nature cell biology

Article

https://doi.org/10.1038/s41556-025-01668-z

# Endoplasmic reticulum–mitochondria contacts are prime hotspots of phospholipid peroxidation driving ferroptosis

Received: 23 April 2024

Accepted: 3 April 2025

Published online: 13 June 2025

Check for updates

Maria Livia Sassano[1,2], Yulia Y. Tyurina[3,11], Antigoni Diokmetzidou[4,5,11], Ellen Vervoort[1,2], Vladimir A. Tyurin[3], Sanket More[1,2], Rita La Rovere[6], Francesca Giordano[7], Geert Bultynck[6], Benjamin Pavie[8], Johan V. Swinnen[9], Hülya Bayir[10], Valerian E. Kagan[3,10], Luca Scorrano[4,5] & Patrizia Agostinis[1,2]

The peroxidation of membrane phospholipids (PLs) is a hallmark of ferroptosis. The endoplasmic reticulum and mitochondria have been implicated in ferroptosis, but whether intracellular PL peroxidation ensues at their contact sites (endoplasmic reticulum–mitochondria contact sites, EMCSs) is unknown. Using super-resolution live imaging, we charted the spatiotemporal events triggered by ferroptosis at the interorganelle level. Here we show that EMCSs expand minutes after localized PL peroxides are formed and secondarily spread to mitochondria, promoting mitochondrial reactive oxygen species and fission. Oxidative lipidomics unravels that EMCSs host distinct proferroptotic polyunsaturated-PLs, including doubly proferroptotic polyunsaturated-acylated PLs, demonstrating their high propensity to undergo PL peroxidation. Endoplasmic reticulum–mitochondria untethering blunts PL peroxidation and ferroptosis, while EMCS stabilization enhances them. Consistently, distancing EMCSs protects the ferroptosis-susceptible triple-negative breast cancer subtype, harbouring high EMCS-related gene expression and basal PL peroxide levels. Conversely, in insensitive triple-negative breast cancer subtypes, bolstering EMCSs sensitizes them to ferroptosis. Our data unveil endoplasmic reticulum–mitochondria appositions as initial hubs of PL peroxide formation and posit that empowering EMCSs endorses ferroptosis in cancer cells.

In eukaryotic cells, the endoplasmic reticulum (ER) establishes a dynamic connection with mitochondria through membrane appositions called ER–mitochondria contact sites (EMCSs). EMCSs are stabilized by protein tethers that operate as bridges between these organelles and provide a molecular platform for signal communication[1,2]. The dynamic regulation and remodelling of EMCSs ensure rapid coordination and integration of physiological and metabolic cues, vital for maintaining organelle and cellular function. A wealth of genetic and biochemical studies validated the functional role of EMCSs in key signalling processes at the cellular and systemic/organ level, including $Ca^{2+}$ fluxes, apoptosis, mitochondrial dynamics, metabolism and lipid homoeostasis[3].

EMCSs play an essential role in transporting phosphatidylcholine (PC), phosphatidylinositol (PI) and phosphatidylserine (PS), from the ER where they are synthesized to the mitochondria[4–6], where PS is rapidly converted to phosphatidylethanolamine (PE) and transferred back to the ER[4–6]. However, while EMCSs are crucialfor the homoeostatic

A full list of affiliations appears at the end of the paper. e-mail: patrizia.agostinis@kuleuven.be

transport of phospholipids (PLs) to mitochondria, our understanding of the spatiotemporal dynamics and remodelling of EMCSs under conditions causing PL peroxidation (PLox) is scant. Oxidized polyunsaturated fatty acids (PUFAs)-containing PEs are the main drivers of ferroptosis, an iron-dependent necrotic cell death caused by the blockade of cellular lipid hydroperoxide detoxification systems and capable of generating myriads of secondary oxidatively-truncated electrophilic species forming adducts with proteins[7–10]. Glutathione peroxidase 4 (GPX4) can reduce hydroperoxyl-PLs to the respective stable alcohols, hence preventing ferroptosis[7–10]. During ferroptosis, PLox produced in membranes rapidly spread[9], ultimately causing plasma membrane damage and cell death. Ferroptosis has been implicated in several pathologies including neurodegeneration, cancer and cardiovascular diseases[11]. However, while substantial progress has been made in understanding the molecular effector mechanisms of ferroptosis, the events that govern the initial PLox damage and its precise subcellular localization remain elusive.

Different organelles have been linked to the regulation of ferroptosis[12] in different cellular settings[12–17]. For example, the radical-trapping agent ferrostatin-1 (Fer-1) targeted to mitochondria protects cells against ferroptosis induced by cysteine starvation or inhibitors of the system $x_c^-$, whereas ER-localized Fer-1 protects from ferroptosis induced by a small molecule inhibitor of GPX4 (refs. 13,14). In the cells exposed to diacyl-PUFA-PLs, mitochondria-targeted antioxidants blunt lipid reactive oxygen species (ROS) formation in the ER and reduce ferroptosis[15]. While these studies implicate primarily the ER and mitochondria in the regulation of ferroptosis, it remains unclear how these organelles precisely control the onset of PLox production and the propagation of these lethal signals during ferroptosis. Portraying the precise spatiotemporal dynamics of EMCSs under conditions eliciting PLox is paramount to gaining molecular insights into the initial stages of ferroptosis and identifying sites of interventions to regulate its lethal progression.

In this study, by combining high-resolution live cell imaging with oxidative phospholipidomics of subcellular fractions and EMCS genetic perturbation, we identify EMCSs as primary sites of early PLox in cells undergoing ferroptosis.

## Results

### ER–mitochondria contacts rapidly expand during ferroptosis

To assess the dynamics of EMCS remodelling induced by lipid-ROS in real time, we first validated the induction of ferroptosis in our cellular model. We used the RAS-selective lethal (1*S*,3*R*)RSL3 (ref. 18) GPX4 inhibitor and the cystine-glutamate antiporter system $x_c^-$ blocker imidazole ketone erastin (IKE), which by impeding the import of cystine causes glutathione (GSH) depletion and inactivation of GPX4 among other GSH-depending enzymes[19], as established class II and I ferroptosis inducers (FINs), respectively. In murine embryonic fibroblasts (MEFs) (1*S*,3*R*)RSL3 (or just RSL3) but not the inactive diastereomer (1*R*,3*R*)RSL3 (ref. 20), induced cell death that was prevented by the iron chelator deferoxamine mesylate salt (DFO) and the radical scavenger and suppressor of arachidonoyl-PE oxidation[21] Fer-1 (Extended Data Fig. 1a,b). Likewise, cell death induced by IKE was prevented by DFO, Fer-1 and by the reducing agent beta-mercaptoethanol (BME), which can promote cystine uptake through mechanisms bypassing system $x_c^-$ (ref. 9) (Extended Data Fig. 1c,d). By contrast, inhibitors of caspases (*Z*-Val-Ala-DL-Asp(OMe)-fluoromethylketone, ZVAD) or RIPK1 (necrostatin-1s, Nec1s) (Extended Data Fig. 1a,c) failed to do so. The cell death was preceded by the Fer-1-inhibitable activation of PLox, as measured by the ratiometric fluorescent indicator of membrane vulnerability to PLox Bodipy 581/591 C11 (Bodipy C11), a commonly used biomarker of ferroptosis (Extended Data Fig. 1e). Together, these observations demonstrate the induction of bona fide ferroptosis by class II and I FINs in our settings.

We then conducted time-lapse live cell imaging using super-resolution confocal Airyscan microscopy and a three-dimensional (3D) rendering of acquired *z*-stacks to visualize the early remodelling of EMCSs during ferroptosis in cells expressing Sec61ß–mCherry (as an ER marker) and incubated with MitoTracker Far Red (to stain the mitochondrial network). As early as 15 min following RSL3 treatment, the ER surface engaged in contact with the mitochondria expanded from a steady-state level of ~15% in untreated cells to ~30%, plateauing at this level (Fig. 1a,b). A proximity ligation assay (PLA) between mitochondrial VDAC1 and ER-associated IP3R3, two known EMCS markers[22,23], confirmed the fast kinetics of EMCS expansion and their perdurance up to 1 h after RSL3 treatment (Fig. 1c,d). This rapid EMCS remodelling was not observed in cells treated with the DNA-damaging agent cisplatin (CDDP) or the pan-kinase inhibitor staurosporine, undergoing Fer-1-insensitive and ZVAD-inhibitable apoptosis (Extended Data Fig. 1f–i).

To characterize the impact of ferroptosis induction on EMCS architecture at the ultrastructural level, we then conducted transmission electron microscopy (TEM) and calculated the ER–mitochondria contact coefficient (ERMICC), which computes various parameters involved in contact sites[24]. The distance separating the ER and mitochondria shortened from an average of 20 nm of the resting cells to 9 nm in response to RSL3 treatment (15 min) (Fig. 1e,f), and the ERMICC coefficient increased by more than fourfold as compared with untreated cells (Fig. 1e, g).

EMCSs play a crucial role in allowing efficient mitochondrial $Ca^{2+}$ uptake upon ER $Ca^{2+}$ depletion[1,25]. Elevations in cytosolic[26] or mitochondrial[27,28] $Ca^{2+}$ have been implicated in the regulation of ferroptosis. Cells expressing the genetically encoded mitochondria-targeted $Ca^{2+}$ indicator mito-R-GECO1 (ref. 29) and loaded with cytosolic $Ca^{2+}$

**Fig. 1 | EMCSs rapidly expand at the onset of lipid peroxidation. a**, Representative volume-rendered 3D reconstructions of confocal *z*-stacks from time-lapse live images of MEFs transiently transfected with ER marker Sec61ß–mCherry (cyan) and stained with MitoTracker Far Red (magenta) at time 0 and 5, 15 and 30 min after RSL3 (0.5 µM) (5′RSL3, 15′RSL3 and 15′RSL3, respectively). The EMCS masked volume, representing colocalization of ER and mitochondria, is indicated in white. The magnified images represent a merge of ER, mitochondrial surfaces and EMCS mask. Scale bar, 10 µm. Zoom, 1 µm. **b**, The per cent of EMCSs normalized on ER volume (Sec61ß–mCherry) at time 0 and 5′RSL3, 15′RSL3 and 15′RSL3 (0.5 µM) ($n = 3$ biological replicates, the same cells ($n = 11$) were acquired and analysed at each timepoint per condition). Similar experiments have been reproduced independently in Fig. 4, Supplementary Fig. 2 and Supplementary Fig. 3. **c**,**d**, Representative images (**c**) of in situ PLA in MEFs and quantification (**d**) of *N* of dots corresponding to IP3R3–VDAC1 interaction per nucleus in untreated cells and in cells treated for 15 and 30 min and 1 h with RSL3 (0.125 µM) ($n = 3$ biological replicates, images $n = 15$ for untreated, $n = 21$ for 15′RSL3, $n = 21$ for 30′RSL3, $n = 20$ for 1 h RSL3). Scale bar, 10 µm. **e**–**g**, Representative TEM images of EMCSs at time 0 and 15 min after RSL3 (0.125 µM) and cotreatment with Fer-1 (1 µM) (**e**), quantification of EMCSs distance (**f**) and ER-mitochondria contact coefficient (ERMICC; interface length/(mitochondrial perimeter × distance ER–mitochondria)) (**g**), with a morphometric analysis of the ER located at less than 30 nm from the mitochondria ($n = 70$ images per condition, five cells per condition from two biological replicates). **h**,**i**, Representative images (**h**) of in situ PLA in MEFs and quantification (**i**) of *N* of dots corresponding to the IP3R3–VDAC1 interaction per nucleus in untreated cells and in cells treated for 15 min with RSL3 (0.125 µM) or cotreated with RSL3 (0.125 µM) and Fer-1 (1 µM) ($n = 3$ biological replicates, images $n = 23$ for untreated, $n = 17$ for 15′RSL3, $n = 32$ for 15′RSL3 + Fer-1). Scale bar, 10 µm. In **d**, and **i**, at least two wells per condition were imaged and quantified per biological replicate. Each image contained multiple cells. All quantitative data are the mean ± s.e.m. In **b**, the statistical significance was determined by a repeated-measures one-way ANOVA, Dunnett post hoc test. In **d**, **f**, **g** and **i**, the statistical significance was determined by a one-way ANOVA, Tukey post hoc test. n.s., not significant ($P > 0.05$), $^*P \leq 0.05$, $^{**}P < 0.01$, $^{***}P < 0.001$.

https://doi.org/10.1038/s41556-025-01668-z

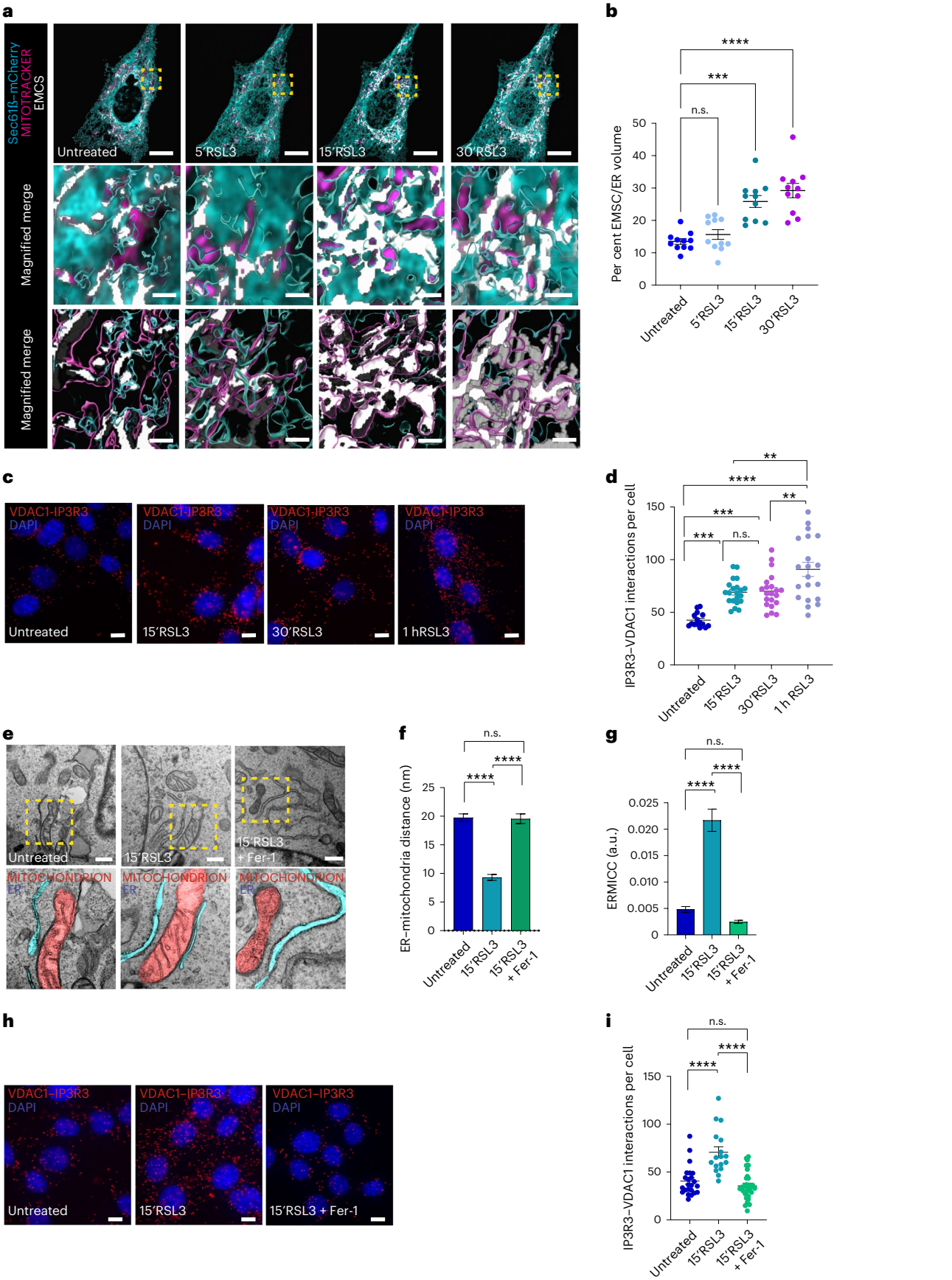

https://doi.org/10.1038/s41556-025-01668-z

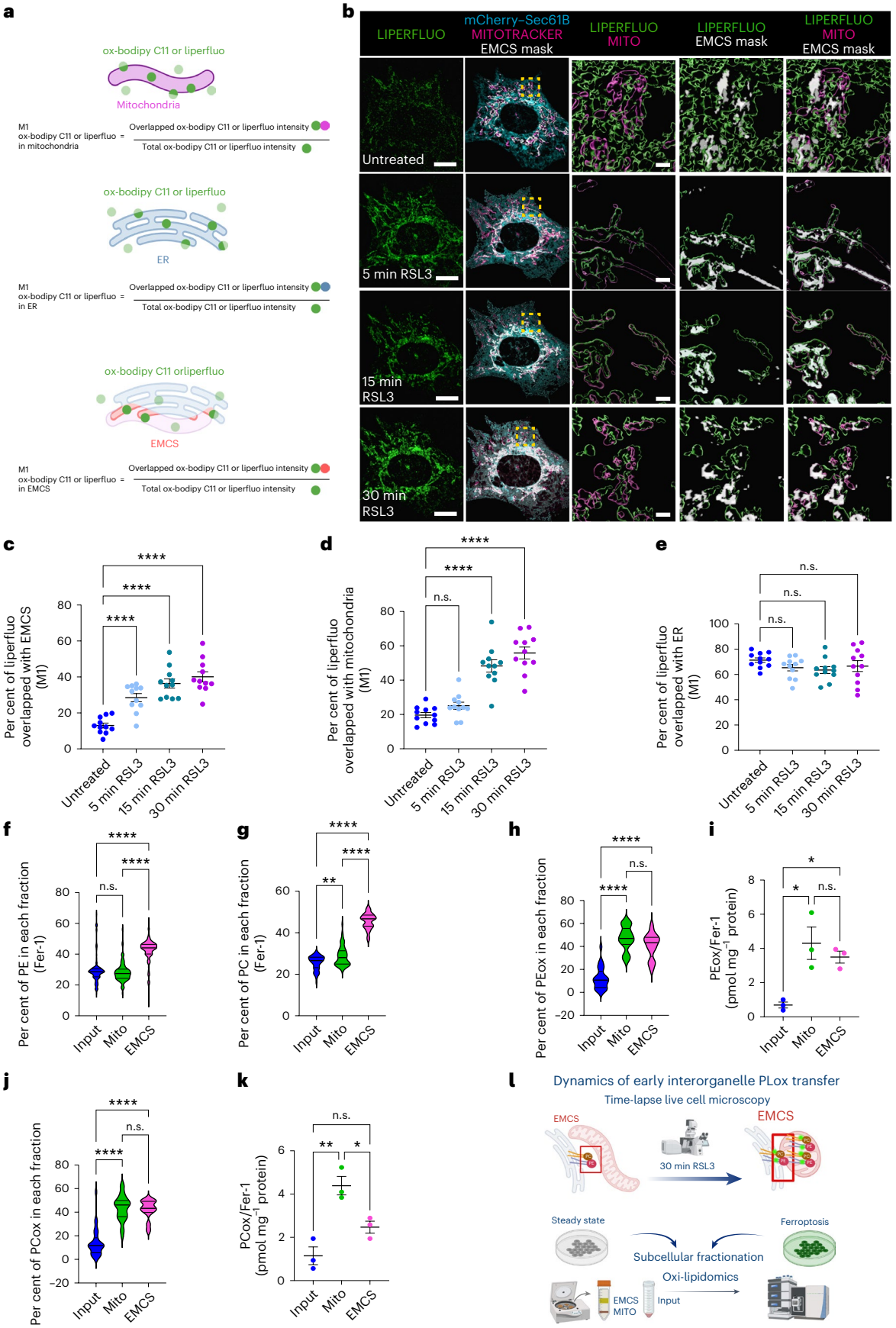

**Fig. 2 | PLox initiates at EMCSs and propagates to the mitochondria.** **a**, A schematic representation of Mander's coefficient (M1). The M1 quantifies the fraction of the signal intensity of the lipid peroxidation probe that colocalizes in each subcellular compartment/organelle relative to the total signal intensity of the probe. **b**, Representative volume-rendered 3D reconstructions of confocal *z*-stacks from time-lapse live images of MEFs transiently transfected with ER marker Sec61ß–mCherry (cyan) and stained with MitoTracker Far Red (magenta) and Liperfluo (green) at time 0 and 5, 15 and 30 min after RSL3 (0.5 µM). The EMCS masked volume, representing colocalization of ER and mitochondria, is indicated in white. The magnified images represent, respectively, (i) Liperfluo and mitochondrial surfaces, (ii) Liperfluo surface and EMCS mask and (iii) Liperfluo and mitochondrial surfaces together the with EMCS mask. Scale bar, 10 µm. Zoom, 1 µm. **c**–**e**, The colocalization (M1%) of Liperfluo in the EMCSs (**c**), mitochondria (**d**) and ER (**e**) masks at time 0 and 5, 15 and 30 min after RSL3 (0.5 µM) ($n = 3$ biological replicate, the same cells ($n = 11$) were acquired and analysed at each timepoint per condition). Similar experiments and settings have been reproduced independently in Fig. 4, Supplementary Fig. 2 and Supplementary Fig. 3. **f**,**g**, The per cent of total PE (**f**) and PC (**g**) in the input, EMCSs and mitochondrial fraction ($n = 3$ biological replicates, 105 PE subspecies, 58 PC subspecies). **h**–**k**, The per cent of PEox (**h**) and PCox (**j**) in the input, EMCSs and mitochondrial fraction and PEox (**i**) and PCox (**k**) fold changes compared with corresponding conditions cotreated with Fer-1 (1 µM) ($n = 3$ biological replicates, 25 PEox subspecies, 29 PCox subspecies). **i**, A schematic representation of the complementary approaches and methodology used to assess the dynamics of early interorganelle PLox transfer. All quantitative data are the mean ± s.e.m. In **c**–**e**, the statistical significance was determined by a repeated-measures one-way ANOVA, Dunnett post hoc test. In **f**–**h** and **j**, the statistical significance was determined by a repeated-measures one-way ANOVA, Tukey post hoc test. In **i** and **k**, the statistical significance was determined by a one-way ANOVA, Tukey post hoc test. n.s., not significant ($P > 0.05$), $^{*}P \leq 0.05$, $^{**}P < 0.01$, $^{***}P < 0.001$. Panel **a** created with BioRender.com.

indicator Cal520 to concomitantly measure mitochondrial and cytosolic $Ca^{2+}$ ($cytCa^{2+}$) levels were treated with RSL3 in a $Ca^{2+}$-free medium for 15 min, followed by the addition of ATP to evoke $Ca^{2+}$ release from ER $Ca^{2+}$ stores (Extended Data Fig. 1j–m). RSL3 did not alter ATP-induced $cytCa^{2+}$ elevation (Extended Data Fig. 1j,k) but potentiated mitochondrial $Ca^{2+}$ uptake (Extended Data Fig. 1l,m). This suggests that early remodelling of EMCS facilitates the transfer of $Ca^{2+}$ to mitochondria, without affecting the overall $cytCa^{2+}$ levels. The cell-permeable high-affinity/fast-kinetic $Ca^{2+}$ chelator BAPTA-AM did not affect the EMCS expansion caused by RSL3 (Extended Data Fig. 1n,o). While these results do not confute the participation of $Ca^{2+}$ signals in ferroptosis at later stages, they suggest that elevation of $Ca^{2+}$ is not the main trigger of EMCS remodelling in the early phases of ferroptosis.

By contrast, in cells treated with RSL3, blockade of PLox by Fer-1 (Extended Data Fig. 1e) inhibited EMCS expansion as shown by TEM analysis (Fig. 1e–g) and PLA (Fig. 1h,i).

We conclude that PLox prompts ER–mitochondria tethering.

## PLox starts at EMCSs and propagates to the mitochondria

To capture early PLox and their interorganelle transfer we monitored by live imaging the subcellular distribution of oxidized Bodipy C11 (ox-Bodipy) signal by creating masks of the mitochondria, the ER, and the overlapping area between the ER and mitochondria, representing the EMCSs (Extended Data Fig. 2a–d), in untreated cells and following 5, 15 and 30 min after RSL3 exposure. We then evaluate at each timepoint the fraction of oxidized Bodipy C11 signal that spatially overlapped with the ER, mitochondria and EMCSs, using Mander's coefficient (M1) as a quantitative measure of the cooccurrence of ox-Bodipy C11 fluorescence with a subcellular organelle[30,31] (Fig. 2a).

The steady-state levels of ox-Bodipy C11 in the ER, which houses important cellular redox reactions, were significantly higher compared with those of the EMCSs and mitochondria (Extended Data Fig. 2b–d). However, the ox-Bodipy C11 signal did not change throughout the time of RSL3 treatment in the ER; if anything, it showed a decreasing trend 30 min after RSL3 addition (Extended Data Fig. 2b). Of note, as soon as 5 min after RSL3 exposure, a significantly larger fraction of ox-Bodipy C11 signal overlapped with EMCSs and persisted up to 30 min (Extended Data Fig. 2c), at the time when a marked ox-Bodipy C11 signal colocalized with mitochondria (Extended Data Fig. 2d). At variance, the residual cellular fraction of ox-Bodipy C11, obtained upon the removal of the ER and mitochondria and EMCS masks, showed a decline (Extended Data Fig. 2e). Since both Bodipy C11 and its oxidation product do not spontaneously leave lipid monolayers for at least over 2 h (ref. 32), diffusion events are unlikely to contribute to the rapid increase in the ox-Bodipy C11 signal in EMCSs observed in our settings.

To chase the spatiotemporal dynamics of PLox within the same cell, we performed 3D rendering of time-lapse super-resolution live imaging of cells expressing Sec61ß–mCherry (as ER marker) and costained with MitoTracker Far Red and the LiperFluo probe. The LiperFluo green-fluorescent signal results from the reduction of lipid hydroperoxides, thus providing a direct assessment of PLox formation[33]. We then analysed (Fig. 2a) the kinetics of PLox organelle redistribution in cells treated with RSL3 (Fig. 2b–e) or IKE (Extended Data Fig. 3a–e).

Consistent with the findings using Bodipy C11 (Extended Data Fig. 2c,d), after 5 min of RSL3 exposure, we observed a rapid increase in the fraction of LiperFluo signal spatially overlapping with the EMCSs, which further redistributed to the mitochondria within 15 min (Fig. 2c,d), along with the steady expansion of the EMCSs (Fig. 1a,b). No significant changes in the ER-associated LIperFluo signal were observed over the time of RSL3 treatment (Fig. 2b,e), mirroring the results with Bodipy C11 (Extended Data Fig. 2a,b). A similar spatial redistribution of Fer-1 inhibitable PLox was observed, albeit with slower kinetics, after

**Fig. 3 | PERK deficiency protects from EMCS expansion during the early phases of ferroptosis.** **a**, Representative FRET live microscopy images of $PERK^{WT}$ and $PERK^{KO}$ MEFs transiently infected with FEMP probe (mAKAP1-YFP-Tav2-CFP-Sac1) and treated with RSL3 (0.5 µM) and $PERK^{WT}$ cotreated with RSL3 (0.5 µM) + Fer-1 (1 µM) at time 0 and 15 min after RSL3 treatment. Scale bar, 10 µm. Zoom, 10 µm. **b**, The FEMP ratio at 0, 15 and 30 min and 1 h after RSL3 (0.5 µM) and rapamycin treatment, in $PERK^{WT}$ MEFs transiently infected with a FEMP probe ($n = 3$ biological replicates, multiple areas in the same well were acquired and analysed per each timepoint per condition per biological replicate). MAX, maximum. **c**, Time-lapse imaging of the FEMP ratio traces, fold changes (on untreated) of $PERK^{WT}$ and $PERK^{KO}$ MEFs treated with RSL3 (0.5 µM) and $PERK^{WT}$ cotreated with RSL3 (0.5 µM) + Fer-1 (1 µM) infected with the FEMP probe. Where indicated, the cells were treated with 100 nM rapamycin. **d**, The FEMP ratio at 0, 15 and 30 min and 1 h after RSL3 (0.5 µM) treatment and rapamycin treatment, in $PERK^{WT}$ and $PERK^{KO}$ MEFs and $PERK^{WT}$ cotreated with RSL3 (0.5 µM) + Fer-1 (1 µM) infected with the FEMP probe ($n = 3$ biological replicates, multiple areas in the same well were acquired and analysed per each timepoint per condition and biological replicate). **e**,**f**, Representative images (**e**) of in situ PLA in $PERK^{WT}$ and $PERK^{KO}$ MEFs and quantification (**f**) of *N* of dots corresponding to IP3R3–VDAC1 interaction per nucleus in untreated cells and in cells treated for 15 and 30 min and 1 h with RSL3 (0.125 µM) ($n = 3$ biological replicates, images $n = 15$ for $PERK^{WT}$ untreated, $n = 20$ for $PERK^{WT}$ 15 min of RSL3 (15′RSL3), $n = 20$ for $PERK^{WT}$30′RSL3, $n = 19$ for $PERK^{WT}$ for 1 h RSL3, $n = 17$ for $PERK^{KO}$ untreated, $n = 18$ for $PERK^{KO}$ 15′RSL3, $n = 20$ for $PERK^{KO}$ 30′RSL3, $n = 20$ for $PERK^{KO}$ for 1 h RSL3 and quantified as described in Fig. 1d). Scale bar, 10 µm. All quantitative data are mean ± s.e.m. In **b**, the statistical significance was determined by a repeated-measures two-way ANOVA, Tukey post hoc test. In **d**, the statistical significance was determined by a one-sample *t*-test. In **f**, the statistical significance was determined by a two-way ANOVA, Tukey post hoc test. n.s., not significant ($P > 0.05$), $^{*}P \leq 0.05$, $^{**}P < 0.01$, $^{***}P < 0.001$.

https://doi.org/10.1038/s41556-025-01668-z

IKE (Extended Data Fig. 3a–e). Overall cellular PLox levels following RSL3 or IKE (that is, mean fluorescence intensity of ox-Bodipy C11 or LiperFluo) showed similar kinetics, with an early buildup of PLox steadily increasing over time (Extended Data Fig. 2f, g; Extended Data Fig. 3f).

Ferroptosis is associated with the generation of oxidation products from PUFA-PLs, particularly containing PC and PE[3–5], and EMCSs are the spatially restricted sites of PC and PS transfer between the ER and mitochondria[8–10]. We posited that following their expansion,

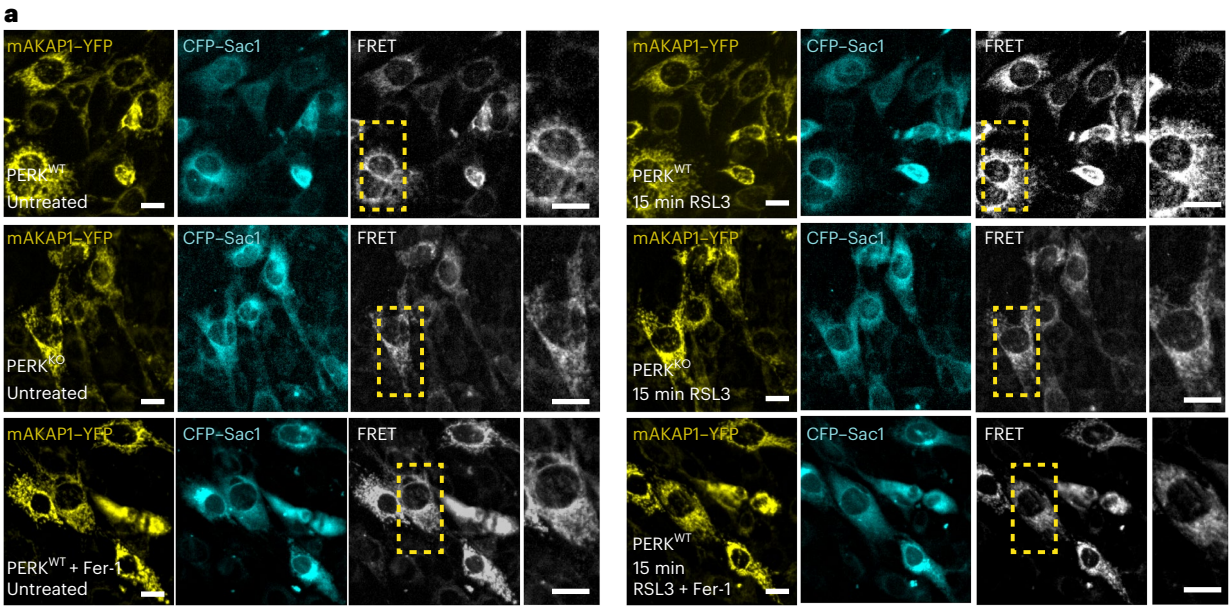


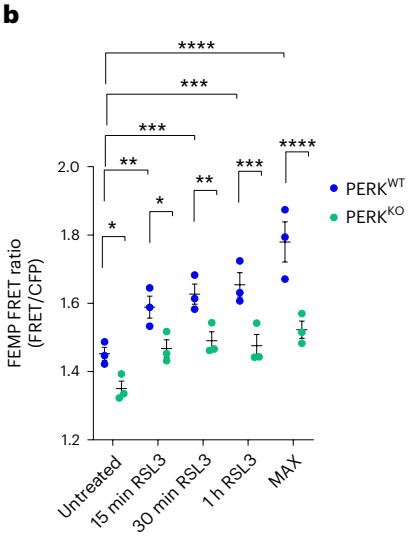


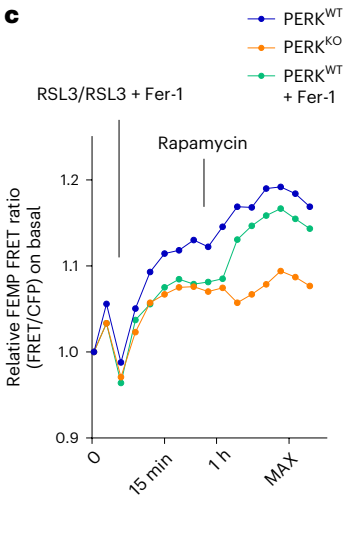


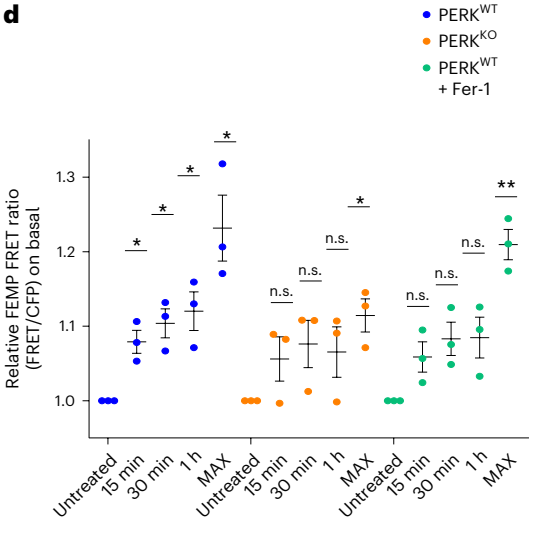


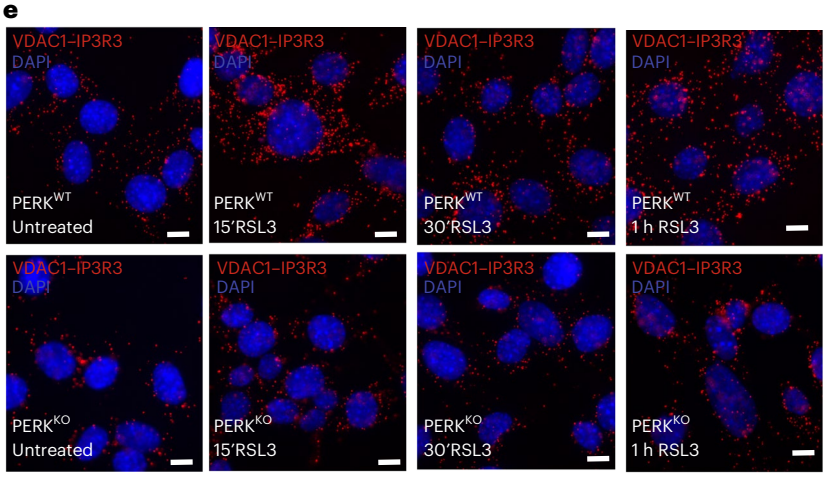


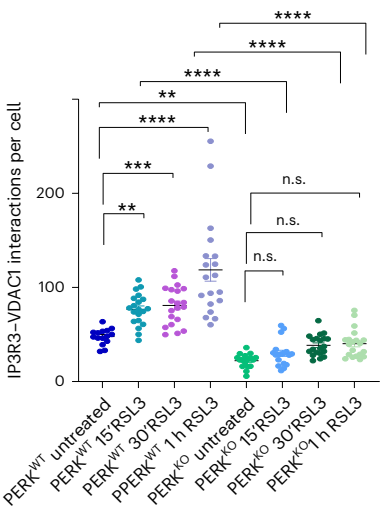

https://doi.org/10.1038/s41556-025-01668-z

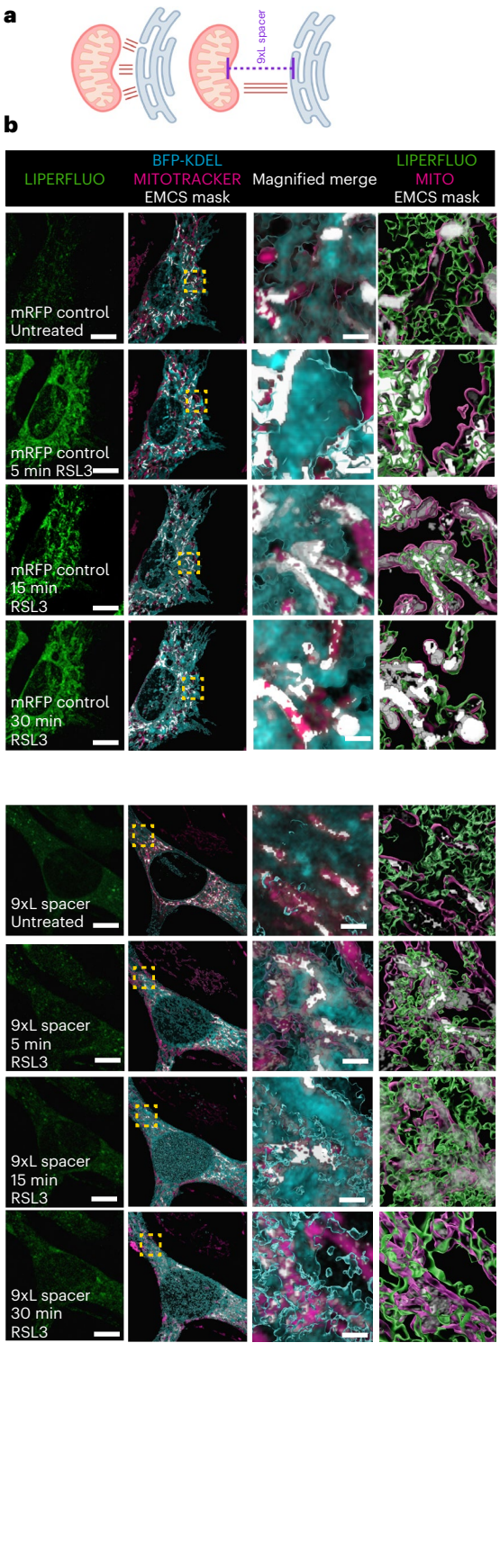

**Fig. 4 | Spacing EMCSs protects cells from EMCS-mediated mitochondrial PLox. a**, A schematic representation of 9xL spacer. **b**, Representative volume-rendered 3D reconstructions of confocal *z*-stacks from time-lapse live images of MEFs transiently transfected with AKAP1–mRFP control or 9xL spacer and the ER marker BFP–KDEL (cyan) and stained with MitoTracker Far Red (magenta) and Liperfluo (green) at time 0, 5, 15 and 30 min after RSL3 (0.5 µM). The EMCS masked volume, representing colocalization of the ER and mitochondria, is indicated in white. The magnified images represent, respectively, (i) the merge of ER, mitochondrial surfaces and EMCS mask and (ii) Liperfluo and mitochondrial surfaces together with EMCS mask. Scale bar, 10 µm. Zoom, 1 µm. **c**, A quantification of the per cent of EMCSs normalized on the ER volume (BFP–KDEL) at time 0, 5, 15 and 30 min after RSL3 (0.5 µM) in MEFs transiently transfected with AKAP1–mRFP control or 9xL spacer ($n = 3$ biological replicates). ctrl, control. **d**–**f**, A colocalization (Mander's coefficient (M1), per cent) of Liperfluo in the EMCS (**d**), mitochondria (**e**) and ER (**f**) masks at time 0, 5, 15 and 30 min after RSL3 (0.5 µM) treatment in MEFs transiently transfected with AKAP1–mRFP control or 9xL spacer ($n = 3$ biological replicates, the same cells ($n = 7$ mRFP control, $n = 7$ 9xL spacer) were acquired and analysed at each timepoint per condition). Similar experiments and settings have been reproduced independently on Fig. 2, Supplementary Fig. 2 and Supplementary Fig. 3. All quantitative data are the mean ± s.e.m. In **c**, **d**, **e** and **f**, the statistical significance was determined by a two-way repeated-measures ANOVA, Tukey post hoc test. n.s., not significant ($P > 0.05$), $^{*}P \leq 0.05$, $^{**}P < 0.01$, $^{***}P < 0.001$. Panel **a** created with BioRender.com.

particularly oxidized PE (PEox) and oxidized PC (PCox) could be channelled to the mitochondria via ER–mitochondria juxtapositions. We exposed cells for 30 min to RSL3, either alone or in combination with Fer-1, to specifically block RSL3-induced PLox and isolated the cell's input, their respective EMCSs and the enriched mitochondria fraction (that is, containing the mitochondria and associated EMCSs) (Extended Data Fig. 4a) by ultracentrifugation. We conducted liquid chromatography tandem mass spectrometry (LC-MS/MC)-based lipidomics and redox lipidomics analysis and calculated the fractional distribution of total PE, PC and mitochondrial cardiolipin (CL), as well as all their oxidized forms in the input, EMCSs and mitochondrial fraction (Fig. 2f–h,j). These data are also presented as fold changes compared with those of the samples cotreated with Fer-1 (Fig. 2i,k). In non-oxidizing conditions (Fer-1), EMCSs were enriched in the overall PE and PC species compared with the input and the mitochondrial fraction (Fig. 2f,g). After 30 min of RSL3, the total content of PEox (Fig. 2h,i) and PCox (Fig. 2j,k) was elevated both in the mitochondrial fraction and EMCSs, suggesting the relocation of these PLox between EMCSs and the mitochondria, in agreement with the spatial data of the ox-Bodipy C11 (Extended Data Fig. 2a,c,d) and Liperfluo signal (Fig. 2b–d). By contrast, CL oxidation did not change and remained restricted to the mitochondrial fraction (Extended Data Fig. 4b,c). Thus the integration of real-time imaging with liquid chromatography with tandem mass spectrometry (LC–MS/MS)-based lipidomics and redox lipidomics of organellar fractions (Fig. 2l) reveals that EMCSs are key interfaces for the initiation and subsequent mitochondrial propagation of PLox during ferroptosis.

Accompanying the accumulation of mitochondrial PLox at 30 min, we observed the fragmentation of the mitochondrial network (Extended Data Fig. 4d–k) the production of mitochondrial superoxide (Extended Data Fig. 4l,m) followed by a steady increase in mitochondrial PLox (Extended Data Fig. 4n). The rapid dynamics of Fer-1 inhibitable PLox redistribution (Extended Data Fig. 3a–f) and subsequent mitochondrial fragmentation (Extended Data Fig. 4d–k) following IKE probably reflect cell context-dependent mechanisms that control the abundance of the glutathione pool and ferroptosis sensitivity, as described in previous studies[34,35].

Hence, during ferroptosis, early PLox ensues at the EMCSs and spreads to the mitochondria, triggering their morphological and redox changes.

## Spacing EMCSs protects mitochondria from lipid-ROS attack

We then tested whether preventing ER–mitochondria tethering in response to lipid-ROS affected key steps of the ferroptosis cascade.

We first investigated the effects of the knockout of PERK, the unfolded protein response (UPR) sensor with moonlighting function at the ER–mitochondria contacts independent of its kinase activity[36–38]. Consistent with our previous studies[37,38], the loss of PERK impaired EMCS formation in steady-state conditions (Extended Data Fig. 5a–c). We then transiently transduced wild-type PERK ($PERK^{WT}$) and PERK-knockout ($PERK^{KO}$) cells with the fluorescence resonance energy transfer (FRET)-based ER–mitochondria proximity probe (FEMP)[24]. FEMP contains a FKBP-FRB dimerization domain that, following rapamycin treatment, allows maximal juxtaposition between the two spectral GFP variants targeted to the mitochondria and ER. A brief rapamycin pulse therefore allows measuring of not only the basal but also the extent of the maximal juxtaposition possible between the two organelles[39]. In $PERK^{WT}$ cells, EMCSs rapidly increased after RSL3 treatment with kinetics such as those observed in our previous analysis (from 15 min to 1 h) (Fig. 3a,b). In line with the expected defect in EMCS formation, the basal and maximal FEMP signal was lower $PERK^{KO}$ cells (Fig. 3a,b). Following RSL3, the FEMP signal rapidly and steadily increased in $PERK^{WT}$ cells, whereas it remained consistently reduced in PERK-deficient cells, indicating their inability to form proficient EMCSs in response to PLox (Fig. 3a–c). Fer-1 reduced RSL3-mediated EMCS expansion in $PERK^{WT}$ cells to a similar extent to what was observed in

**Fig. 5 | EMCSs house ferroptosis-prone PUFA-containing PLs. a**,**b**, Representative images (**a**) and quantification (**b**) of in situ PLA in $PERK^{WT}$ and $PERK^{KO}$ MEFs untreated and after RSL3 (0.125 µM, 6 h) ($n = 3$ biological replicates, images $n = 21$ for $PERK^{WT}$ untreated, $n = 26$ for $PERK^{WT}$ 6h RSL3, $n = 23$ for $PERK^{KO}$ untreated, $n = 26$ for $PERK^{KO}$ 6 h RSL3, quantified as in Fig. 1d). Scale bar, 10 µm. **c**, A volcano plot depicting changes in PL content between input and EMCSs in $PERK^{WT}$ MEFs. **d**, A heat map visualizing the individual 78 PL species, based on the VIP scores and a two-sided unpaired *t*-test ($P < 0.05$) in $PERK^{WT}$ MEFs quantified as pmol $mg^{-1}$ protein and auto-scaled to *z*-scores and coded blue (low values) to red (high values). The VIP scores for respective PL species are shown on the top ($n = 3$ biological replicates). **e**, The total contents of PUFAs in PUFA-PEd, PUFA-PEp and PUFA-PCd in EMCSs versus input in $PERK^{WT}$ MEFs ($n = 3$ biological replicates). **f**, A volcano plot depicting the differences in PL content between input and EMCSs samples in $PERK^{KO}$ MEFs ($n = 3$ biological replicates). **g**, A heat map visualizing the changes in the individual PL species based on the VIP scores and a two-sided unpaired *t*-test ($P < 0.05$) in EMCSs versus input in $PERK^{KO}$ MEFs. The data are quantified as in **d**. **h**, The total contents of PUFAs in PUFA-PEd, PUFA-PUFA-PEp and PUFA-PCd in EMCSs versus input in $PERK^{KO}$ MEFs ($n = 3$ biological replicates). **i**, A heat map showing the content of the individual 18 PLox species based on the VIP scores and a two-sided unpaired *t*-test ($P < 0.05$) in EMCSs from $PERK^{WT}$ MEFs treated with RSL3 (0.125 µM) in the absence or presence of Fer-1. The data are quantified as in **d** ($n = 3$ biological replicates). **j**, A heat map visualizing the changes in the content of three PEox species based on the VIP scores and a two-sided unpaired *t*-test ($P < 0.05$) in input $PERK^{WT}$ MEFs. The data are quantified as in **d** ($n = 3$ biological replicates). **k**, The content of di-PUFA-PE (40:8) in $PERK^{WT}$ and $PERK^{KO}$ EMCS versus input ($N = 3$ biological replicates). **l**, A heat map depicting individual PEox and PGox species in EMCSs from $PERK^{KO}$ MEFs treated with RSL3 (0.125 µM) with or without Fer-1 (1 µM). The data are quantified as in **d**. OPLS-DA modelling for oxidized PLs from $PERK^{KO}$ MEFs and EMCSs from $PERK^{KO}$ MEFs yielded zero components; therefore, the VIP scores were not available ($n = 3$ biological replicates). In **b**, **e**, **h** and **k**, the quantitative data are the mean ± s.e.m. In **b** and **k**, the statistical significance was determined by a two-way ANOVA, Tukey (for **b**) or Sidak (for **k**) post hoc test. In **c**, **e**, **f** and **h**, the statistical significance was determined by a two-sided unpaired *t*-test. n.s., not significant ($P > 0.05$), $^{*}P \leq 0.05$, $^{**}P < 0.01$, $^{***}P < 0.001$.

https://doi.org/10.1038/s41556-025-01668-z

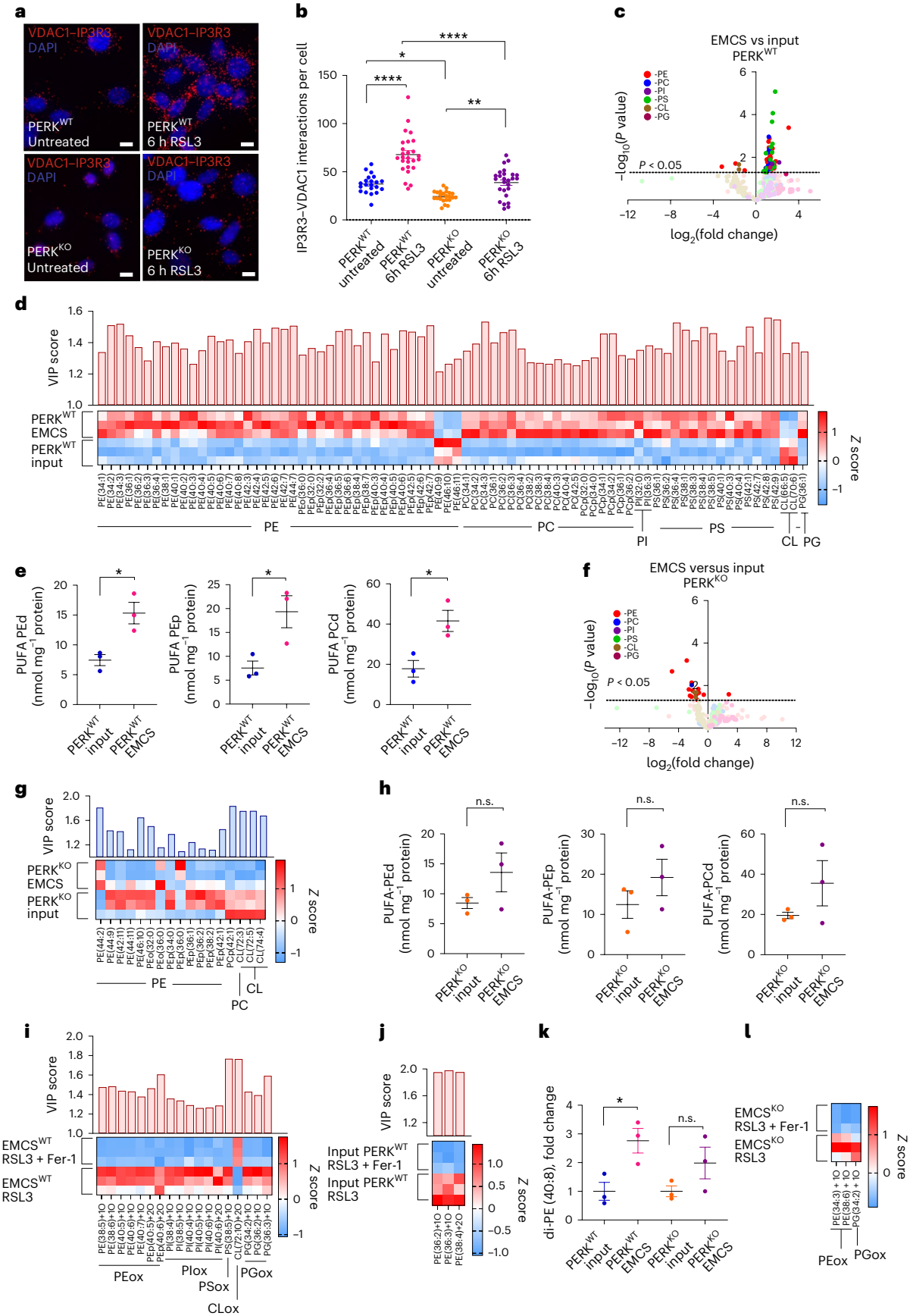

PERK$^{KO}$ cells, supporting the causal link between lipid-ROS and the early expansion of ER–mitochondria juxtapositions (Fig. 3d). These findings were confirmed by PLA analysis of EMCSs in PERK $^{WT}$ and PERK$^{KO}$ cells (Fig. 3e,f).

Since the loss of PERK could have additional or indirect effects on the composition of the ECMSs[36,40,41], we tested whether preventing EMCS expansion and remodelling by an artificial tether could phenocopy the effects observed in PERK$^{KO}$ cells. We introduced in MEFs the engineered tether 9xL containing the mitochondria-targeting sequence AKAP1 (34-63)–RFP linked to the ER marker yUBC6 by a sequence with nine tandem repeats, which we called 'spacer' since it separates contact sites at a membrane gap distance of approximately 20 nm (ref. 42) (Fig. 4a). In agreement, the expression of the 9xL spacer reduced EMCSs as measured by FEMP analysis (Extended Data Fig. 5d,e).

We conducted time-lapse imaging in live cells exposed to RSL3 for 30 min (Fig. 4b–g). Notably, transient expression of the 9xL spacer, blunted the overall cellular LiperFluo signal elicited by RSL3 (Extended Data Fig. 5f), the primary PLox accumulation in the EMCSs, the consequent expansion of EMCSs and the secondary accumulation of PLox in the mitochondria (Fig. 4b–f).

Together, these results suggest that distancing EMCSs and/or limiting their dynamics[43], either genetically or synthetically, thwarts the initial formation of PLox at these subcellular sites and their subsequent spreading to the mitochondria.

Conforming to our previous studies[37], PERK deficiency did not alter the global lipidome (Extended Data Fig. 5g) or the mitochondrial network (Extended Data Fig. 6a–d) in untreated cells. Similar results were obtained in cells transiently expressing the 9xL spacer (Extended Data Fig. 5h and Extended Data Fig. 6e,f). However, consistent with their effects on preventing EMCS expansion, both PERK deficiency and expression of the 9xL spacer blunted mitochondrial fragmentation (Extended Data Fig. 6a–f) in cells undergoing ferroptosis[9,44].

PERK deficiency also abolished the subsequent production of mitochondrial lipid-ROS (3 h) and overall cellular PLox (6 h) (Extended Data Fig. 6g,h).

Hence, the remodelling of the mitochondrial network, mitochondria PL peroxidation and overall lipid-ROS are secondary to the expansion of EMCSs driven by FINs.

## Thwarting EMCSs blunts oxidation of proferroptosis PUFA-PLs

Oxidation products from PUFA-PLs, particularly from PE and PC species with one PUFA located in sn-2 position (mono-PUFA) or two PUFAs localized in sn-1 and sn-2 positions of the PE (di-PUFA-PE) and PC molecule (di-PUFA PC) promote ferroptosis[15,17].

Following the early increase in ER–mitochondria tethering, the EMCSs remained stable through the first 6 h of RSL3 treatment corresponding to the apex of PLox formation (Extended Data Fig. 1c). We examined whether preventing EMCS expansion during ferroptosis affects the abundance and composition of PLox at these subcellular sites. We chose PERK$^{WT}$ and PERK$^{KO}$ cells as models for several reasons: loss of PERK precluded (1) EMCS expansion (Figs. 3a–f and 5a,b), (2) the ensuing mitochondrial dysfunctions and (3) overall PLox (Extended Data Fig. 6a–d,g–h). Furthermore, PERK deficiency, by perturbing EMCS integrity, affects the homoeostatic transfer of PLs from the ER to mitochondria[37], which may modify the proferroptosis lipid landscape of the EMCSs (Fig. 2f–k).

We performed LC–MS/MS-based lipidomics and redox lipidomics in PERK$^{WT}$ and PERK$^{KO}$ cells treated with RSL3 for 6 h, either alone or in combination with Fer-1, and isolated the cell's input and respective EMCSs by ultracentrifugation (Extended Data Fig. 7a).

Following LC-MS/MC phospholipidomics, we conducted orthogonal partial least squares discriminant analyses (OPLS-DA) using all identified non-oxidized PLs. This analysis revealed that input and EMCSs of PERK$^{WT}$ cells clustered into separate groups (Extended Data Fig. 7b). Consistent with the phospholipidomics analysis of early timepoints (Fig. 2f,g) compared with the phospholipidome of the input, the EMCSs of the PERK$^{WT}$ cells were enriched in several PEs and PCs. This fraction also contained several PI, PS, and phosphatidylglycerol (PG) species (Fig. 5c,d). A variable importance in projection (VIP) predictive score plot (with a threshold of 1) generated from OPLS-DA identified 78 PLs species distinguishing input from EMCSs (Fig. 5c). Particularly, 40 PEs, 19 PCs, 2 PIs, 14 PSs, 2 CLs and 1 PG species were identified as significant components that drove the differences between these two groups (Fig. 5d). In the EMCSs of these cells, the contents of 34 PE molecular species out of the total 40 were significantly increased and contained PUFAs with two or more double bonds, thus highly susceptible to oxidization[9,45] (Fig. 5d). The total levels of PUFA-PE diacyls (PUFA-PEd), PUFA-PE plasmalogens (PUFA-PEp) and PUFA-PC diacyls (PUFA-PCd) were significantly upregulated in the EMCSs of the wild-type cells compared with their respective inputs (Fig. 5e). The same trend, although not significant, was observed for PUFA-PC-plasmalogen, PUFA-PS, PUFA-PI and PUFA-PG (Extended Data Fig. 7c). The inner mitochondrial membrane CL was enriched in the input of the PERK$^{WT}$ cells (Fig. 5d and Extended Data Fig. 7d), thus ruling out cross-contamination of the isolated EMCS fractions by mitochondria membranes.

We analysed the effect of loss of EMCS integrity on their PL composition. OPLS-DA analysis separated input from the EMCSs of PERK$^{KO}$ cells into two distinct clusters (Extended Data Fig. 7e) and identified 17 PLs with high VIP scores (Fig. 5f). Notably, PERK deficiency suppressed the rich PL variety and the highly unsaturated PL species of the EMCSs of the wild-type cells (Fig. 5c,d,f,g), restricting it to only three PE species, of which only one with double bonds (Fig. 5f,g). In these EMCS fractions, several oxidation-prone PUFAs, such as PUFA-PEd, PUFA-PEp and PUFA-PCd (Fig. 5h), were not significantly increased.

**Fig. 6 | ER–mitochondria tethering fosters ferroptosis. a**, The per cent of cell death of PERK$^{WT}$ and PERK$^{KO}$ MEFs at time 0 and after RSL3 (0.125 µM, 24 h) in the absence or presence of ZVAD (30 µM), Nec1s (30 µM), DFO (50 µM) or Fer-1 (1 µM) ($n$ = 4 biological replicates, three wells per condition per biological experiment). **b**, Representative images of live cells from PERK$^{WT}$, PERK$^{KO}$ and PERK$^{KO}$ MEFs after transient re-expression of PERK$^{KD}$ at time 0 (T0) and 24 h (T24h) after RSL3 (0.5 µM). The images show SYTOX Green staining and bright field (BF). Scale bar, 100 µm. **c**, The per cent of cell death in PERK$^{WT}$, PERK$^{KO}$ and PERK$^{KO}$ MEFs after transient re-expression of PERK$^{KD}$ after RSL3 (0.5 µM, 24 h) ($n$ = 3 biological replicates). **d**, Representative images of live cells from MFN2$^{KO}$ MEFs transiently transfected with HA-tag-EV, MFN2-HA and ERMIT2-HA at T0 and after RSL3 (0.5 µM, 24 h). The images show SYTOX Green staining and BF. Scale bar, 100 µm. **e**, The per cent of cell death in MFN2$^{KO}$ MEFs transiently transfected with HA-tag-EV, MFN2-HA and ERMIT2-HA after RSL3 (0.5 µM, 24 h). Scale bar, 100 µm ($n$ = 3 biological replicates). **f**, Representative images of live cells from PERK$^{WT}$ MEFs transiently transfected with AKAP1–mRFP control or 9xL spacer at time 0 and 24 h after RSL3 (0.5 µM). The images show SYTOX Green staining, BF and RFP. Scale bar, 100 µm. **g**, The per cent of cell death in PERK$^{WT}$ MEFs transiently transfected with AKAP1–mRFP control or 9xL spacer after RSL3 (0.5 µM, 8 h) ($n$ = 3 biological replicates). **h**, A schema of the OMM–ER linker. **i**, Representative images of live cells from PERK$^{WT}$ and PERK$^{KO}$ MEFs transiently transfected with AKAP1–mRFP control and PERK$^{KO}$ transiently transfected with the OMM–ER linker at time 0 and 24 h after RSL3 (0.5 µM). The images show SYTOX Green staining, BF and RFP. Scale bar, 100 µm. **j**, The per cent of cell death of PERK$^{WT}$ and PERK$^{KO}$ MEFs transiently transfected with AKAP1–mRFP control and PERK$^{KO}$ transiently transfected with the OMM–ER linker after RSL3 (0.5 µM, 24 h). Scale bar, 100 µm ($n$ = 3 biological replicates). All the quantitative data are the mean ± s.e.m. In **a**, the statistical significance was determined by a two-way ANOVA, Sidak post hoc test. In **c**, **e** and **j**, the statistical significance was determined by a one-way ANOVA, Tukey post hoc test. In **g**, the statistical significance was determined by a two-sided unpaired $t$-test. n.s., not significant ($P > 0.05$), *$P \leq 0.05$, **$P < 0.01$, ***$P < 0.001$.

https://doi.org/10.1038/s41556-025-01668-z

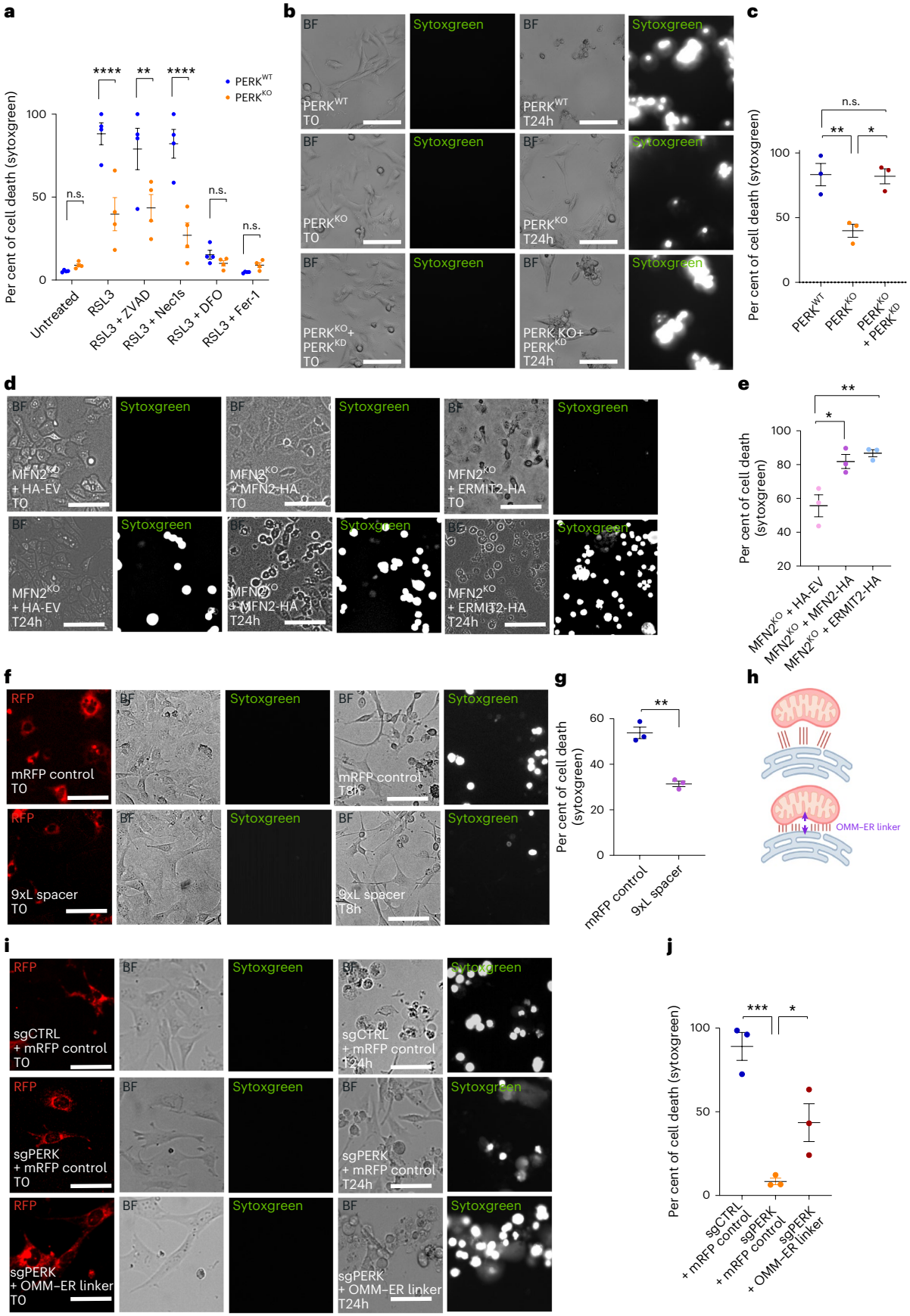

We conducted redox lipidomics of the input and EMCS fractions of PERK$^{WT}$ and PERK$^{KO}$ cells after RSL3 treatment. OPLS-DA analysis based on the PLox species separated RSL3 and RSL3 + Fer-1 samples in different clusters for both input and EMCSs of the PERK$^{WT}$ samples (Extended Data Fig. 7f,g). The presence of Fer-1 protected all major PL species from peroxidation (Fig. 5i,j and Extended Data Fig. 7h,i) except for CL. When compared with their inputs, which showed significant enrichment in three major PEox species (Fig. 5j and Extended Data Fig. 7i), the PLox landscape of the EMCSs of PERK$^{WT}$ cells was highly diversified and contained oxidatively modified species in all major PL classes (Fig. 5i and Extended Data Fig. 7h). Among those, we detected five PEox and one PSox, whose precursors were elevated in the EMCSs of the PERK$^{WT}$ cells but not in those of the PERK$^{KO}$ cells (Extended Data Fig. 8a and Fig. 5k). In wild-type cells, the content of the highly oxidable di-PUFA PE, PE(40:8), was almost 2.8 times higher in the EMCSs than in the input. By contrast, in the EMCSs of the PERK$^{KO}$ cells, this di-PUFA was not enriched (Fig. 5k). Furthermore, in cells with defective EMCSs (that is PERK$^{KO}$ cells) the presence of PLox was restricted to two PEox and one PGox species (Fig. 5l and Extended Data Fig. 8b).

PERK deficiency did not change the expression of the main cellular antioxidant machinery (Extended Data Fig. 8c–f) or the MUFA to PUFA ratio in any PL species within the input and EMCS fraction significantly (Extended Data Fig. 8g). However, we cannot exclude the possibility that the small changes observed contribute to the overall PERK phenotype.

Together, these results disclose the high vulnerability of the EMCS lipidome to ROS attack.

## Enforcing ER–mitochondria tethering endorses ferroptosis

Given the role of ER–mitochondria appositions in controlling the onset and propagation of lipid-ROS signals, we then tested their causal role in ferroptosis. Consistent with their protective effects against EMCS-mediated formation of lipid-ROS, PERK-deficient cells were significantly resistant to ferroptosis induced by different RSL3 and IKE doses when compared with their wild-type counterparts (Fig. 6a and Extended Data Fig. 9a–e), indicating a general protective response against these FINs. ER stress and, in particular, the PERK–ATF4 axis of the UPR has been involved in ferroptosis[46,47]. To discriminate the possible contribution of PERK kinase-mediated signalling function in ferroptosis, we expressed in PERK$^{KO}$ MEFs the UPR-defective PERK kinase-dead mutant (PERK$^{KD}$) (Extended Data Fig. 9f), which restores only the PERK tethering function at the EMCSs[37,38]. Re-expression of PERK$^{KD}$ rescued the vulnerability of the PERK$^{KO}$ cells to ferroptosis to a similar extent found in PERK-proficient cells (Fig. 6b,c), demonstrating that PERK-dependent tethering function is critical for RSL3 cytotoxicity. Consistent with this, chemical inhibition of PERK kinase activity failed to protect cells from ferroptosis (Extended Data Fig. 9g). Likewise, ferroptosis progressed unaltered in cells expressing the S51A phosphorylation mutant of eIF2α, the downstream effector of the PERK arm of the UPR (Extended Data Fig. 9h). Hence, loss of PERK impairs ferroptosis irrespective of its UPR function.

We further validated these findings by deleting mitofusin 2 (MFN2), a well-established ER–mitochondria tether[24,48]. The recently identified MFN2 splice variant ERMIT2 localizes at the EMCS interface and tethers the ER with mitochondria[49]. MFN2$^{KO}$ cells in which MFN2-HA was re-expressed (Extended Data Fig. 9i) succumbed to RSL3-induced ferroptosis while MFN2 deletion (MFN2$^{KO}$) mitigated it (Fig. 6d,e). Consistent with its tethering function, rescuing ERMIT2-HA expression in MFN2$^{KO}$ cells (Extended Data Fig. 9i) significantly corrected their ferroptosis vulnerability (Fig. 6d,e). Cells expressing the EMCS 9xL spacer were also protected from RSL3-mediated cell death (Fig. 6f,g), thus phenocopying the effects of the genetic loss of the PERK and MFN2 tethers.

We then sought orthogonal support for these findings. We first expressed in PERK$^{KO}$ cells a synthetic outer mitochondrial membrane-ER (OMM–ER) linker, AKAP1 (34–63)-mRFP-yUBC6 (Fig. 6h), which shortens the EMCS proximity up to 5 nm while maintaining membrane identity[25]. Expression of the OMM–ER linker increased EMCSs, as judged by FEMP imaging (Extended Data Fig. 9j,k) and restored ferroptosis susceptibility of PERK$^{KO}$ cells (Fig. 6i,j). This suggests that forcing very narrow and/or less dynamic EMCSs[43] overrules the functional effects caused by the loss of a specific tethering molecule. Likewise, overexpression of the ER-associated Sigma1Receptor (S1R) stimulating ER–mitochondria proximity[50] augmented the sensitivity of both PERK$^{WT}$ (Extended Data Fig. 9l,m) and PERK$^{KO}$ cells (Extended Data Fig. 9n,o) to RSL3, consistent with a recent report linking the effect of a small molecule CGI1746 inhibitor of the S1R to ferroptosis sensitivity[51].

Hence, all manoeuvers shortening ER–mitochondria contacts enforce ferroptosis, while distancing EMCSs blunts it.

## EMCSs shape ferroptosis vulnerability of TNBC subtypes

Dysregulation of ER–mitochondria contacts is a hallmark of several diseased conditions, including cancer[52,53]. A recent study exploring the ferroptosis landscape of triple-negative breast cancer (TNBC) identified the luminal androgen receptor (LAR) subtype[45] as the subtype hypersensitive to FINs, compared with the mesenchymal-like (MES), immunomodulatory (IM) or basal-like and immune-suppressed (BLIS) subtypes[54]. Congruently, the MDA-MB-157 cell line, a TNBC LAR subtype, succumbed to ferroptosis, while non-LAR TNBC cell lines were either tolerant (HCC1143, Hs578T) or less sensitive to RSL3 (HCC1937) (Extended Data Fig. 10a,b).

We wondered if the heterogeneity in ferroptosis vulnerability exhibited by the four TNBC subtypes from the extensive cohort of patients (FUSCCTNBC cohort)[54] could reflect a discrepancy in EMCS

**Fig. 7 | EMCSs shape the responses of the triple-negative breast cancer subtypes to ferroptosis. a**,**b**, Box plots of the EMCS-enrichment score, indicating the median line, (1.5× interquartile range (whiskers)) (full list) of each sample calculated by ssGSEA across different TNBC subtypes from **a**: FUSCCTNBC cohort (two-sided Wilcoxon's test), $n = 258$ patient sample ($n = 102$ BLIS, $n = 65$ IM, $n = 62$ LAR, $n = 29$ MES) and from **b**: TCGA cohort (two-sided Wilcoxon's test) $n = 158$ patient samples ($n = 67$ BLIS, $n = 43$ IM, $n = 20$ LAR, $n = 28$ MES). **c**,**d**, Representative immunoblot (**c**) for PERK, S1R and MFN2 in MDA-MB-157 and Hs578T cells and relative quantification (**d**) to MDA-MB-157 cells ($n = 3$ biological replicates). **e**, A heat map visualizing the mean of the ERMCS-enrichment score (manually curated and full list) and normalized abundances of PEox across different TNBC subtypes (FUSCCTNBC cohort). min, minimum; max, maximum. **f**, Representative images of cells from sgCTRL MDA-MB-157 cells transiently transfected with AKAP1–mRFP control or 9xL spacer at time 0 (T0) and after RSL3 (0.5 μM, 6 h (T6h)). The images show SYTOX Green staining, bright field (BF) and RFP. Scale bar, 100 μm. **g**, The per cent of cell death after RSL3 (0.5 μM, 6 h) of sgCTRL MDA-MB-157 cells transiently transfected with AKAP1–mRFP control or 9xL spacer ($n = 3$ biological replicates). **h**, Representative images of sgCTRL and sgPERK MDA-MB-157 cells transiently transfected with AKAP1–mRFP control and sgPERK transfected with OMM–ER linker at time 0 and after 12 h (T12h) of RSL3 (0.5 μM). The images show SYTOX Green staining, BF and RFP. Scale bar, 100 μm. **i**, The per cent of cell death (RSL3 (0.5 μM, 6 h)) in sgCTRL MDA-MB-157 and sgPERK MDA-MB-157 cells transiently transfected with AKAP1–mRFP control and sgPERK with the OMM–ER linker ($n = 3$ biological replicates). **j**, The per cent of cell death after RSL3 (3 μM, 24 h) of HCC1143 cells transiently transfected with AKAP1–mRFP control or OMM–ER linker ($n = 3$ biological replicates). **k**, The per cent of cell death after RSL3 (1 μM, 24 h) of Hs578T cells transiently transfected with AKAP1–mRFP control or OMM–ER linker ($n = 3$ biological replicates). In **d**, **g**, **i**, **j** and **k**, the quantitative data are the mean ± s.e.m. In **d**, the statistical significance was determined by a one-sample *t*-test. In **g**, **j** and **k**, the statistical significance was determined by a two-sided unpaired *t*-test. In **i**, the statistical significance was determined by a one-way ANOVA, Tukey post hoc test. n.s., not significant ($P > 0.05$), $^{*}P \leq 0.05$, $^{**}P < 0.01$, $^{***}P < 0.001$.

https://doi.org/10.1038/s41556-025-01668-z

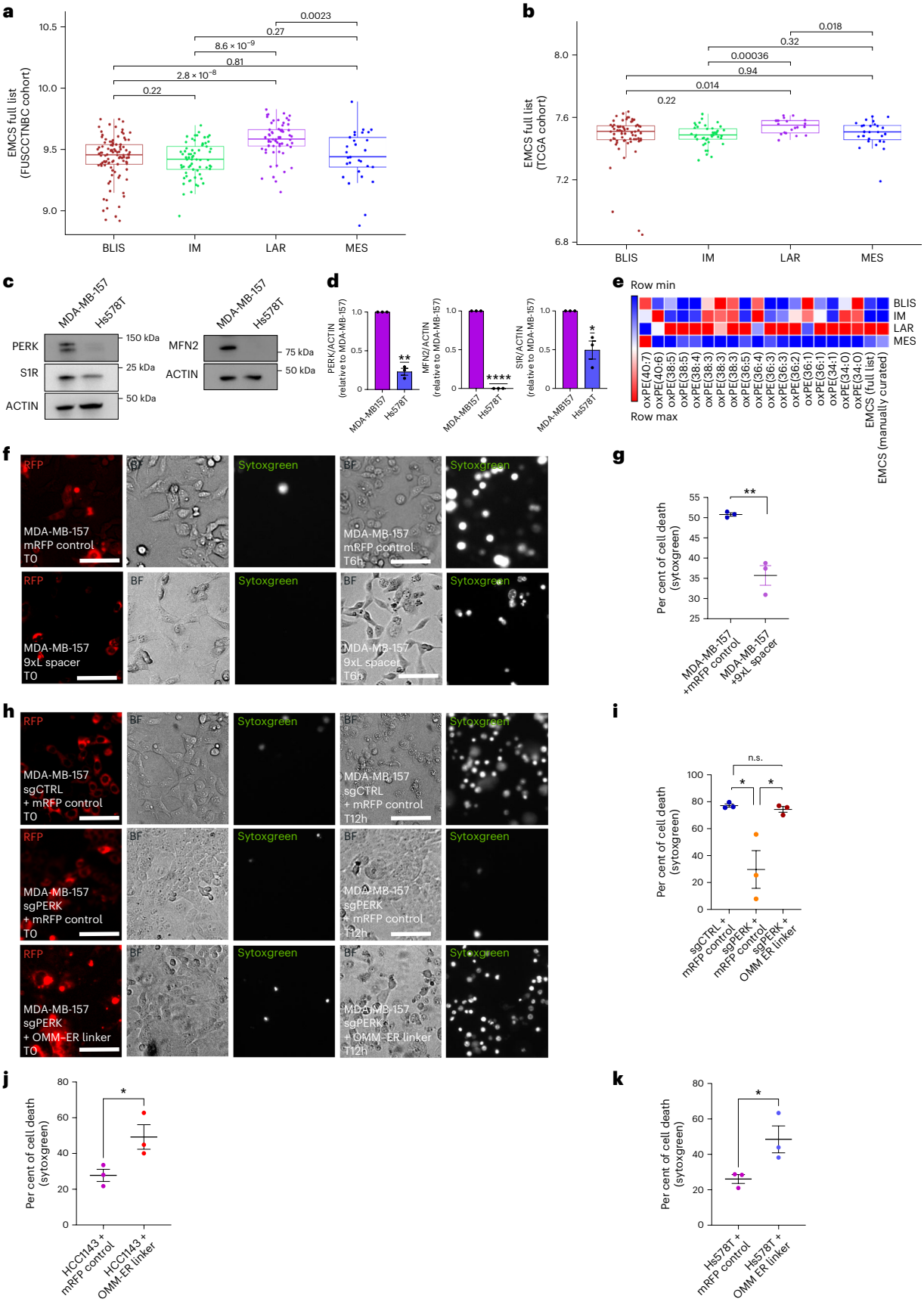

gene expression. We performed a single-sample gene set enrichment analysis (ssGSEA) to calculate the enrichment scores of the EMCS gene signature, based on the recently available database of EMCS-associated proteins[55], on the cohort of TNBC patients[54] (Fig. 7a). Remarkably, TNBC patients with the LAR subtype[54] expressed an enrichment in the set of genes encoding for EMCS components (EMCS$^{high}$ gene signature) when compared with the MES, IM or BLIS subtypes (Fig. 7a). This association was also confirmed by a manually curated gene expression dataset (Supplementary Table 1) of functionally characterized EMCS regulators, including PERK, MFN2 and S1R (Extended Data Fig. 10c) and corroborated through analysis of the transcriptomic data of TNBC from the TCGA cohorts (Fig. 7b and Extended Data Fig. 10d).

In line with the expression data, when compared with the ferroptosis-vulnerable MDA-MB-157 cells of the LAR subtype, the non-LAR TNBC cell lines, Hs578T, HCC1143 and HCC1937, exhibited reduced protein levels of PERK, MFN2 and S1R (Fig. 7c,d and Extended Data Fig. 10e–h), suggesting an impairment in ER–mitochondria tethering and communication. Consistently, these non-LAR TNBC cell lines exhibited reduced ER–mitochondria appositions when compared with the MDA-MB-157 cells (Extended Data Fig. 10i). Previous metabolomic analysis indicated that the LAR phenotype, harbouring heightened expression of multiple ferroptosis-related molecules, had a higher PEox/PUFA-PE ratio when compared with other TNBC subtypes[54]. Using both EMCS gene data sets, we observed that the LAR subtype with the heightened EMCS gene signature (EMCS$^{high}$) was also associated with a robust enrichment in several PEox species (Fig. 7e). Together, these data suggest a link between the functional status of the EMCSs and the heterogeneous response to ferroptosis of the different TNBC subtypes.

To test this assumption, we first perturbed EMCS formation in the MDA-MB-157 cell line by expressing the 9xL spacer (Extended Data Fig. 5d,e) or by CRISPR–Cas9-mediated PERK deletion (Extended Data Fig. 10j) and tested the effects of these genetic manipulations on RSL3-induced ferroptosis. Transient expression of the 9xL spacer (Fig. 7f,g) or loss of PERK (Fig.7h,i) caused a similar resistance to RSL3 (Fig.7f–i). Rescuing EMCS integrity in PERK-deficient MDA-MB-157 cells by the expression of the OMM–ER linker, restored their ferroptosis responses (Fig. 7h,i).

We then postulated that expression of the OMM–ER linker could sensitize the non-LAR TNBC cells to ferroptosis. Consistent with this, expression of the synthetic linker in Hs578T and HCC1143 cells improved their ferroptosis response to RSL3 (Fig. 7j,k), albeit to a reduced extent when compared with the ferroptosis-primed MDA-MB-157 cells (Fig. 7f,i).

Altogether, these findings indicate that EMCS integrity is a critical determinant of the ferroptosis heterogeneity of TNBC and suggest that an EMCS$^{high}$-gene signature could be a predictor of TNBC vulnerability to PLox-induced cell death.

## Discussion

Despite accumulating knowledge of the mechanisms governing ferroptosis, the primary intracellular sites of lipid-ROS generation and subsequent damage remain elusive[56,57].

In this study, by combining super-resolution microscopy in live cells with subcellular oxidative phospholipidomics, we provide several lines of evidence showing PLox occurs at the ER–mitochondria interface within minutes of exposure to FINs. Following its onset at the EMCSs, which consequently expand, PLox propagates to the mitochondria, leading to mitochondrial ROS production and dysfunction. The subsequent buildup of cellular lipid peroxides precipitates ferroptosis.

By probing the lipidome of the EMCSs in unstressed conditions, we demonstrated that EMCSs are particularly enriched in several PUFA-containing PL species, with an abundance of PUFA-containing PEs, with a recognized role in ferroptosis[10,45]. Tempering with EMCS integrity and functions modifies their PL landscape and halts peroxidation of ferroptosis-prone PLs, including several PUFA-containing PEox. A recent study reported that di-PUFA-PC is incorporated in the mitochondria membranes and interacts with complex I of the electron transfer chain, driving the generation of mtROS, while PLox would occur secondarily at the ER[15]. Other studies unravelled that beyond the most abundant redox-sensitive, single PUFA-sn-2-arachidonoyl(AA)-PE and sn-2-adrenoyl(AdA)-PE subspecies, the minor populations di-PUFA-PLs can be oxidized during the early phases of ferroptosis. Among them, the di-PUFA-PE species oxidized by 15LOX at high rates in a Fer-1-inhibitable manner are considered potent proferroptotic mediators[17]. We found that EMCSs also house the minor populations of di-PUFA-PE involved in early peroxidation[17], and their amount is reduced by genetically impairing EMCS integrity. Hence, our data strongly advocate the role of EMCSs as a primary shuttling platform for the bidirectional transfer of lipid peroxides between the ER and the mitochondria, which ultimately amplify the initial ferroptosis signals. The distinguished PL composition of the EMCSs explains why these subdomains of the ER membranes are particularly prone to generating proferroptosis peroxidized PUFA-PLs early in cell death.

The ER can connect with other organelles with an essential role in ferroptosis, such as the iron-rich lysosomes or lipid droplets, via the formation of three-way contact sites[58,59]. This suggests that following the initial formation at the EMCSs, PLox can propagate to membranes of other organelles in close contact, a possibility that warrants further studies.

Furthermore, we demonstrated that preventing EMCS expansion, by depleting key EMCS tethering regulators both at the side of the ER (PERK, S1R and ERMIT2) or mitochondria (MFN2)[60] or by synthetically spacing EMCSs, curbed ferroptosis. We recently found that PERK serves as a scaffold for the recruitment of the ER-associated lipid transfer protein extended-synaptotagmin 1 (E-Syt1) at the EMCSs, forming a complex that favours the transfer of key PLs to the mitochondria[37]. Disrupting endogenous tethers may destabilize molecular complexes and impair lipid transfer function, even when other EMCS components are present. However, whether disturbance in EMCS-associated lipid transfer proteins[37,61,62] or PL biosynthesis enzymes[63] modulates ferroptosis requires future studies.

Notwithstanding, all genetic approaches we used to re-establish or impair EMCS interactions, consistently promoted or inhibited ferroptosis in both murine fibroblasts and human TNBC cell lines.

Notably, the ferroptosis-vulnerable TNBC subtype LAR[54], hosts an enrichment in the expression of EMCS-associated genes along with a higher amount of oxidized-PE species. By contrast, the ferroptosis-insensitive non-LAR TNBC subtypes harbour reduced gene and protein expression of critical EMCS tethers and dysfunctional ER–mitochondria juxtapositions. Expressing the synthetic linker in the non-LAR TNBC cells or distancing EMCSs in the LAR TNBC subtype, respectively sensitized or inhibited ferroptosis of these cancer cells, demonstrating the functional link between EMCS integrity and the heterogeneous responses of TNBC to this type of cell death. This suggests that EMCS gene expression may serve as a potential biomarker to predict sensitivity to ferroptosis in TNBC.

Hence, while EMCSs serve as critical hubs for cancer cells metabolism and plasticity[52], their unique biochemical environment also creates vulnerability to ferroptosis. These tantalizing perspectives have potential clinical and therapeutic implications and warrant future studies.

Our study unravels EMCSs as prime hotspots for PLox driving ferroptosis and suggests that manipulation of ER–mitochondria contacts could be harnessed to regulate cell vulnerability to ferroptosis in diseased conditions.

## Online content

Any methods, additional references, Nature Portfolio reporting summaries, source data, extended data, supplementary information, acknowledgements, peer review information; details of author contributions and competing interests; and statements of data and code availability are available at https://doi.org/10.1038/s41556-025-01668-z.

## References


1. Rizzuto, R. et al. Close contacts with the endoplasmic reticulum as determinants of mitochondrial $Ca^{2+}$ responses. *Science* **280**, 1763–1766 (1998).
2. Vance, J. E. Phospholipid synthesis in a membrane fraction associated with mitochondria. *J. Biol. Chem.* **265**, 7248–7256 (1990).
3. Petrungaro, C. & Kornmann, B. Lipid exchange at ER–mitochondria contact sites: a puzzle falling into place with quite a few pieces missing. *Curr. Opin. Cell Biol.* **57**, 71–76 (2019).
4. Sassano, M. L., Felipe-Abrio, B. & Agostinis, P. ER–mitochondria contact sites; a multifaceted factory for $Ca^{2+}$ signaling and lipid transport. *Front. Cell Dev. Biol.* **10**, 988014 (2022).
5. Vance, J. E. Inter-organelle membrane contact sites: implications for lipid metabolism. *Biol. Direct* **15**, 24–35 (2020).
6. Potting, C. et al. TRIAP1/PRELI complexes prevent apoptosis by mediating intramitochondrial transport of phosphatidic acid. *Cell Metab.* **18**, 287–295 (2013).
7. Tyurina, Y. Y. et al. Redox phospholipidomics discovers pro-ferroptotic death signals in A375 melanoma cells in vitro and in vivo. *Redox Biol.* **61**, 102650 (2023).
8. Wiernicki, B. et al. Excessive phospholipid peroxidation distinguishes ferroptosis from other cell death modes including pyroptosis. *Cell Death Dis.* **11**, 922 (2020).
9. Dixon, S. J. et al. Ferroptosis: an iron-dependent form of nonapoptotic cell death. *Cell* **149**, 1060–1072 (2012).
10. Kagan, V. E., Mao, G., Qu, F. & Angeli, J. P. F. Oxidized arachidonic and adrenic PEs navigate cells to ferroptosis. *Nat. Chem. Biol.* **13**, 81–90 (2016).
11. Stockwell, B. R. Ferroptosis turns 10: emerging mechanisms, physiological functions, and therapeutic applications. *Cell* **185**, 2401–2421 (2022).
12. Dixon, S. J. & Olzmann, J. A. The cell biology of ferroptosis. *Nat. Rev. Mol. Cell Biol.* **25**, 424–442 (2024).
13. Gao, M. et al. Role of mitochondria in ferroptosis. *Mol. Cell* **73**, 354–363.e3 (2019).
14. Gaschler, M. M. et al. Determination of the subcellular localization and mechanism of action of ferrostatins in suppressing ferroptosis. *ACS Chem. Biol.* **13**, 1013–1020 (2018).
15. Qiu, B. et al. Phospholipids with two polyunsaturated fatty acyl tails promote ferroptosis. *Cell* **187**, 1177–1190.e18 (2024).
16. von Krusenstiern, A. N. et al. Identification of essential sites of lipid peroxidation in ferroptosis. *Nat. Chem. Biol.* **19**, 719–730 (2023).
17. Samovich, S. N. et al. Strikingly high activity of 15-lipoxygenase towards di-polyunsaturated arachidonoyl/adrenoyl-phosphatidylethanolamines generates peroxidation signals of ferroptotic cell death. *Angew. Chem. Int. Ed.* **63**, e202314710 (2024).
18. Zhang, Y. et al. Imidazole ketone erastin induces ferroptosis and slows tumor growth in a mouse lymphoma model. *Cell Chem. Biol.* **26**, 623–633.e9 (2019).
19. Yang, W. S. et al. Regulation of ferroptotic cancer cell death by GPX4. *Cell* **156**, 317–331 (2014).
20. Yang, W. S. et al. Peroxidation of polyunsaturated fatty acids by lipoxygenases drives ferroptosis. *Proc. Natl Acad. Sci. USA* **113**, E4966–E4975 (2016).
21. Anthonymuthu, T. S. et al. Resolving the paradox of ferroptotic cell death: ferrostatin-1 binds to 15LOX/PEBP1 complex, suppresses generation of peroxidized ETE-PE, and protects against ferroptosis. *Redox Biol.* **38**, 101744 (2021).
22. Szabadkai, G. et al. Chaperone-mediated coupling of endoplasmic reticulum and mitochondrial $Ca^{2+}$ channels. *J. Cell Biol.* **175**, 901–911 (2006).
23. Tubbs, E. & Rieusset, J. Study of endoplasmic reticulum and mitochondria interactions by in situ proximity ligation assay in fixed cells. *J. Vis. Exp.* **123**, 54899 (2016).
24. Naon, D. et al. Critical reappraisal confirms that Mitofusin 2 is an endoplasmic reticulum-mitochondria tether. *Proc. Natl Acad. Sci. USA* **113**, 11249–11254 (2016).
25. Csordás, G. et al. Structural and functional features and significance of the physical linkage between ER and mitochondria. *J. Cell Biol.* **174**, 915–921 (2006).
26. Pedrera, L. et al. Ferroptotic pores induce $Ca^{2+}$ fluxes and ESCRT-III activation to modulate cell death kinetics. *Cell Death Differ.* **28**, 1644–1657 (2021).
27. Nakamura, T. et al. The mitochondrial $Ca^{2+}$ uptake regulator, MICU1, is involved in cold stress-induced ferroptosis. *EMBO Rep.* **22**, e51532 (2021).
28. Marmolejo-Garza, A. et al. Negative modulation of mitochondrial calcium uniporter complex protects neurons against ferroptosis. *Cell Death Dis.* **14**, 772 (2023).
29. Wu, J. et al. Improved orange and red $Ca^{2+}$ indicators and photophysical considerations for optogenetic applications. *ACS Chem. Neurosci.* **4**, 963–972 (2013).
30. Dunn, K. W., Kamocka, M. M. & McDonald, J. H. A practical guide to evaluating colocalization in biological microscopy. *Am. J. Physiol. Cell Physiol.* **300**, C723–C742 (2011).
31. Nakamura, K. et al. Mitochondrial complexity is regulated at ER-mitochondria contact sites via PDZD8-FKBP8 tethering. *Nat. Commun.* **16**, 3401 (2025).
32. Drummen, G. P. C., van Liebergen, L. C. M., Op den Kamp, J. A. F. & Post, J. A. C11-BODIPY(581/591), an oxidation-sensitive fluorescent lipid peroxidation probe: (micro)spectroscopic characterization and validation of methodology. *Free Radic. Biol. Med.* **33**, 473–490 (2002).
33. Bayır, H. et al. Achieving life through death: redox biology of lipid peroxidation in ferroptosis. *Cell Chem. Biol.* **27**, 387–408 (2020).
34. Magtanong, L. et al. Context-dependent regulation of ferroptosis sensitivity. *Cell Chem. Biol.* **29**, 1409–1418.e6 (2022).
35. Cao, J. Y. et al. A genome-wide haploid genetic screen identifies regulators of glutathione abundance and ferroptosis sensitivity. *Cell Rep.* **26**, 1544–1556.e8 (2019).
36. Sassano, M. L., Derua, R., Waelkens, E., Agostinis, P. & van Vliet, A. R. Interactome analysis of the ER stress sensor perk uncovers key components of er–mitochondria contact sites and $Ca^{2+}$ signalling. *Contact* **4**, 25152564211052392 (2021).
37. Sassano, M. L. et al. PERK recruits E-Syt1 at ER–mitochondria contacts for mitochondrial lipid transport and respiration. *J. Cell Biol.* **222**, e202206008 (2023).
38. Verfaillie, T. et al. PERK is required at the ER–mitochondrial contact sites to convey apoptosis after ROS-based ER stress. *Cell Death Differ.* **19**, 1880–1891 (2012).
39. Csordás, G. et al. Imaging interorganelle contacts and local calcium dynamics at the ER–mitochondrial interface. *Mol. Cell* **39**, 121–132 (2010).
40. van Vliet, A. R. et al. The ER stress sensor PERK coordinates ER–plasma membrane contact site formation through interaction with filamin-A and F-actin remodeling. *Mol. Cell* **65**, 885–899.e6 (2017).
41. Almanza, A. et al. Endoplasmic reticulum stress signalling—from basic mechanisms to clinical applications. *FEBS J.* **286**, 241–278 (2019).
42. Carreras-Sureda, A. et al. Non-canonical function of IRE1α determines mitochondria-associated endoplasmic reticulum composition to control calcium transfer and bioenergetics. *Nat. Cell Biol.* **21**, 755–767 (2019).
43. Obara, C. J. et al. Motion of VAPB molecules reveals ER–mitochondria contact site subdomains. *Nature* **626**, 169–176 (2024).

44. Yagoda, N. et al. RAS–RAF–MEK-dependent oxidative cell death involving voltage-dependent anion channels. *Nature* **447**, 864–868 (2007).
45. Doll, S. et al. ACSL4 dictates ferroptosis sensitivity by shaping cellular lipid composition. *Nat. Chem. Biol.* **13**, 91–98 (2017).
46. Sarcinelli, C. et al. ATF4-dependent NRF2 transcriptional regulation promotes antioxidant protection during endoplasmic reticulum stress. *Cancers* **12**, 569 (2020).
47. Anandhan, A., Dodson, M., Schmidlin, C. J., Liu, P. & Zhang, D. D. Breakdown of an ironclad defense system: the critical role of NRF2 in mediating ferroptosis. *Cell Chem. Biol.* **27**, 436–447 (2020).
48. de Brito, O. M. & Scorrano, L. Mitofusin 2 tethers endoplasmic reticulum to mitochondria. *Nature* **456**, 605–610 (2008).
49. Naón, D. et al. Splice variants of mitofusin 2 shape the endoplasmic reticulum and tether it to mitochondria. *Science* **380**, eadh9351 (2023).
50. Hayashi, T. & Su, T.-P. Sigma-1 receptor chaperones at the ER–mitochondrion interface regulate $Ca^{2+}$ signaling and cell survival. *Cell* **131**, 596–610 (2007).
51. Zhang, Z. et al. CGI1746 targets σ1R to modulate ferroptosis through mitochondria-associated membranes. *Nat. Chem. Biol.* **20**, 699–709 (2024).
52. Sassano, M. L., van Vliet, A. R. & Agostinis, P. Mitochondria-associated membranes as networking platforms and regulators of cancer cell fate. *Front. Oncol.* **7**, 174 (2017).
53. Lei, G., Zhuang, L. & Gan, B. The roles of ferroptosis in cancer: tumor suppression, tumor microenvironment, and therapeutic interventions. *Cancer Cell* **42**, 513–534 (2024).
54. Yang, F. et al. Ferroptosis heterogeneity in triple-negative breast cancer reveals an innovative immunotherapy combination strategy. *Cell Metab.* **35**, 84–100.e8 (2023).
55. Pan, X. et al. MCSdb, a database of proteins residing in membrane contact sites. *Sci. Data* **11**, 281 (2024).
56. Lei, G., Zhuang, L. & Gan, B. Targeting ferroptosis as a vulnerability in cancer. *Nat. Rev. Cancer* **22**, 381–396 (2022).
57. Jakaria, M., Belaidi, A. A., Bush, A. I. & Ayton, S. Ferroptosis as a mechanism of neurodegeneration in Alzheimer's disease. *J. Neurochem.* **159**, 804–825 (2021).
58. Freyre, C. A. C., Rauher, P. C., Ejsing, C. S. & Klemm, R. W. MIGA2 links mitochondria, the ER, and lipid droplets and promotes de novo lipogenesis in adipocytes. *Mol. Cell* **76**, 811–825.e14 (2019).
59. Boutry, M. & Kim, P. K. ORP1L mediated PI(4)P signaling at ER–lysosome–mitochondrion three-way contact contributes to mitochondrial division. *Nat. Commun.* **12**, 5354 (2021).
60. Scorrano, L. et al. Coming together to define membrane contact sites. *Nat. Commun.* **10**, 1287 (2019).
61. Yeo, H. K. et al. Phospholipid transfer function of PTPIP51 at mitochondria-associated ER membranes. *EMBO Rep.* **22**, e51323 (2021).
62. Galmes, R. et al. ORP5/ORP8 localize to endoplasmic reticulum-mitochondria contacts and are involved in mitochondrial function. *EMBO Rep.* **17**, 800–810 (2016).
63. Zhu, Y. et al. Loss of WIPI4 in neurodegeneration causes autophagy-independent ferroptosis. *Nat. Cell Biol.* **26**, 542–551 (2024).




[1]Cell Death Research and Therapy Laboratory, Center for Cancer Biology, Leuven, Belgium. [2]Department of Cellular and Molecular Medicine and Leuven Kanker Instituut, KU Leuven, Leuven, Belgium. [3]Department of Environmental and Occupational Health and Center for Free Radical and Antioxidant Health University of Pittsburgh, Pittsburgh, PA, USA. [4]Department of Biology, University of Padua, Padova, Italy. [5]Veneto Institute of Molecular Medicine, Padova, Italy. [6]Laboratory of Molecular and Cellular Signaling, Department of Cellular and Molecular Medicine and Leuven Kanker Instituut, KU Leuven, Leuven, Belgium. [7]Inserm, Gif-sur-Yvette, France. [8]VIB-bioimaging Center UGent, Zwijnaarde, Belgium. [9]Laboratory of Lipid Metabolism and Cancer, Department of Oncology, KU Leuven, Leuven, Belgium. [10]Department of Pediatrics, Division of Critical Care and Hospital Medicine, Redox Health Center, Vagelos College of Physicians and Surgeons, Columbia University Irving Medical Center, New York, NY, USA. [11]These authors contributed equally: Yulia Y. Tyurina, Antigoni Diometzidou. ✉e-mail: patrizia.agostinis@kuleuven.be

## Methods

### Cell lines

Simian virus 40 (SV40)-immortalized MEFs proficient or deficient for PERK (PERK$^{WT}$ and PERK$^{KO}$ cells respectively) were a kind gift from Dr David Ron (Cambridge Institute for Medical Research). All MEFs were maintained in Dulbecco's modified Eagle's medium (DMEM) containing 4.5 g $l^{-1}$ glucose and 0.11 g $l^{-1}$ sodium pyruvate and supplemented with 2 mM glutamine, 100 units $ml^{-1}$ penicillin, 100 µg $ml^{-1}$ streptomycin and 10% foetal bovine serum (FBS). The triple-negative breast cancer cell lines, MDA-MB-157 and HCC1937 purchased from ATCC, were a gift from Professor Marcus Conrad (Helmholtz Zentrum Munich) and Professor Colinda Scheele (VIB–KU Leuven Center for Cancer Biology), respectively. The breast cancer cell lines HCC1143 and Hs578t were purchased from ATCC and authenticated by BMR genomics[64].

MDA-MB-157 efficiently integrated the negative control non-targeting single-guide RNA (sgRNA) (MDA-MB-157 sgCTRL) and the EIF2AK3 (MDA-MB-157 shPERK) human sgRNA and Cas9 using 4D-Nucleofector SE solution (Lonza Bioscience). The HCC1937 cells were maintained in Roswell Park Memorial Institute supplemented with 2 mM glutamine, 100 units $ml^{-1}$ penicillin, 100 µg $ml^{-1}$ streptomycin and 10% FBS; MDA-MB-157 (wild type and PERK$^{KO}$), HCC1143 and Hs578T were maintained in DMEM containing 4.5 g $l^{-1}$ glucose and 0.11 g $l^{-1}$ sodium pyruvate and supplemented with 2 mM glutamine, 100 units $ml^{-1}$ penicillin, 100 µg $ml^{-1}$ streptomycin and 10% FBS. MEFs eIF2α wild type (S/S) and eIF2α (S/A) were a kind gift from Professor Frans Schuit (KU Leuven).

### Plasmids

PERK.K618A.9E10 pcDNA-myc-tagged plasmid (Addgene plasmid #21815), BFP–KDEL (Addgene plasmid #49150) and Sec61ß–mCherry (Addgene plasmid #121160) were obtained from Addgene. AKAP1–mRFP, AKAP1 (34-63)-9x-mRFP-yUBC6 (9xL spacer) and AKAP1 (34–63)-mRFP-yUBC6 (OMM–ER linker) were a kind gift from Professor György Hajnóczky (Thomas Jefferson University). KDEL-HRP-myc was previously reported[40]. S1R–GFP was a kind gift from Professor Paolo Pinton (University of Ferrara). CMV-mito-R-GECO1 was a gift from Dr Robert Campbell (University of Alberta) (Addgene plasmid #46021). FEMP, HA-tag-empty vector (HA-tag-EV), MFN2-HA and ERMIT2-HA were previously reported[24,49].

### Western blotting

The samples were separated by SDS–polyacrylamide gel electrophoresis on the Criterion system (Bio-Rad Laboratories) on a 4%–12% Bis–Tris gel and electrophoretically transferred to Protran 2-µm-pored nitrocellulose paper (PerkinElmer). The blots were blocked for 1 h at room temperature (RT) in TBS-T buffer (50 mM Tris, pH 7.4, 150 mM NaCl, 0.1% Tween-20) containing 5% non-fat dry milk and then incubated with selected antibody solutions processed and analysed as described in ref. 37.

### Antibodies chemicals and reagents

Anti Mouse Alexa Fluor 488, Thermo Fisher Scientific, A11001, 1:200; anti-rabbit 488 Alexa Fluor (Thermo Fisher Scientific, A-27034, 1:200); anti-mouse Alexa Fluor 647 (Thermo Fisher Scientific, A-21235, 1:200); anti-rabbit Alexa Fluor 647 (Thermo Fisher Scientific, A-21244, 1:200); mouse monoclonal anti ACTIN (Sigma-Aldrich, A5441, clone AC-15, lot no. 0000126949, 1:1,000); rabbit monoclonal anti-ACSL4 (Santa Cruz Biotechnology, sc-271800, clone A-5, lot no. H0923, 1:1,000); mouse monoclonal anti c-myc, (Sigma-Aldrich, M4439, clone 9E10, lot no. 0000184338, 1:1,000); rabbit polyclonal anti calnexin, (Enzo, ADI-SPA-865-F, 1:1,000); mouse monoclonal anti CYTC (BD Bioscience, 556433, clone 7H8.2C12 (RUO), lot no. 9157540, 1:1,000); Duolink In Situ Detection Reagents Red (Sigma-Aldrich, DUO92008, 1:40); Duolink In Situ PLA Probe anti-mouse MINUS (Sigma-Aldrich, DUO92004, 1:5); Duolink In Situ PLA Probe Anti-Rabbit PLUS (Sigma-Aldrich, DUO92004, 1:5); Duolink In Situ Mounting Medium with 4′,6-diamidino-2-phenylindole (DAPI) (Sigma-Aldrich, DUO82040); rabbit monoclonal anti GAPDH (Cell Signaling, 2118S, clone 14C10, lot no. 16, 1:1,000); rabbit polyclonal anti GPX4 (Cell Signaling, 52455 1:1000); rabbit polyclonal anti HA-Tag (C29F4) (Cell Signaling, 3724S, 1:1,000); mouse monoclonal anti-IP3R3 (BD Bioscience, 610312, clone 2:IP3R3 (RUO), lot no. 2329334, 1:100); rabbit polyclonal anti-MFN2 (Abcam, ab50838, 1:1,000); rabbit polyclonal anti PERK, Cell Signaling, 3192S, 1:1,000); mouse monoclonal anti TOMM20 (Abcam, ab186735, Abcam, EPR15581-54, lot no. 1011221-48, 1:100); rabbit polyclonal VDAC1 (Abcam, ab15895, 1:100); rabbit polyclonal VDAC1 (Cell Signaling, 4866S; 1:1,000); rabbit polyclonal anti SLC7A11 (Thermo Fisher Scientific, PA1-16893, 1:1,000).

The reagents used were: Bodipy 581/591 C11 (Thermo Fisher Scientific); Liperfluo (Dojindo), D-glucose (Sigma-Aldrich, G7021-1KG); DAPI (Thermo Fisher Scientific, 62248); DAPI (Thermo Fisher Scientific, D1306); DMEM—high glucose (Sigma-Aldrich, D0422); Gibco DMEM/F-12 (Thermo Fisher Scientific, 11320074); Duolink In Situ Mounting Medium with DAPI (Sigma-Aldrich, DUO82040); GSK2606414 PERK Inhibitor (Toronto Research Company, G797800); MitoPerox (Abcam, ab146820); MitoTracker Far Red (Thermo Fisher Scientific, M22426); MitoTracker Green (Thermo Fisher Scientific, M7514); SE Cell Line 4D-NucleofectorTM X Kit L (Lonza Bioscience, V4XC-1024); P3 Cell Line 4D-NucleofectorTM X Kit L (Lonza Bioscience, V4XP-3024); penicillin and streptomycin (Sigma-Aldrich, P0781); Pierce ECL Western Blotting Substrate (Thermo Fisher Scientific, 32106×4); Pierce Protease Inhibitor Tablets, EDTA-free (Thermo Fisher Scientific, 88266); potassium chloride (Janssen Chimica, 7447407); protease inhibitor (Thermo Fisher Scientific, A32953); saponin (Sigma-Aldrich, 8047152); Gibco, Roswell Park Memorial Institute Sodium Chloride, (Sigma-Aldrich, A0431796); SYTOX Green (Sigma-Aldrich, S7020); TransIT-X2 Dynamic Delivery System (Mirus Bio, MIR 6000); Tris base (Sigma-Aldrich, 77861); Triton (Sigma-Aldrich, T9234); Tween (Sigma-Aldrich, P4780).

The plates used for microscopy were: glass-bottom dishes, 35 mm uncoated, glass no. 1.5 (Case Mattek corporation, P35G-1.5-14-C); 6-well glass-bottom plates (Cellvis, P06-1.5H-N); 24-well glass-bottom plate with high performance no. 1.5 cover glass P24-1.5H-N; CultureWell Chambered Coverglass for Cell Culture, 16 wells per coverglass, C37000.

The chemical used were: BME (21985023); BAPTA-AM (B1205); Cas9 (2NLS Biolegio); CDDP (Sigma, CAS 15663-27-1); DFO (Sigma-Aldrich, D9533-1G); Fer-1 SML0583-5MG (Sigma-Aldrich, SML0583-5MG); IKE (Selleckchem, S8877); Nec1s (Sigma-Aldrich, 2263-1MG); staurosporine (Sanbio, 81590-1); rapamycin (Adipogen, AG-CN2-0025); RSL3 (Selleckchem, S8155-5MG); 1*R*,3*R*-RSL3 (Biotechne, 6687/10); sg EIF2AK3 human (Biolegio); ZVAD (Bachem, 4027403.0005).

### Cell transfection

The MEFs were transiently transfected with PERK.K618A.9E10 pcDNA-myc tagged, BFP–KDEL, mt-GECO1-RFP, AKAP1–mRFP, AKAP1 (34-63)-9x-mRFP-yUBC6 (9xL spacer), AKAP1 (34–63)-mRFP-yUBC6 (OMM–ER linker), KDEL-HRP, HA-tag-EV, MFN2-HA, ERMIT2-HA and S1R–GFP using TransIT-X2 transfection reagent accordingly to the manufacturer's instructions or electroporated with 4D-Nucleofector (Lonza Bioscience) using P3 Cell Line kit (V4XP-3024, Lonza Bioscience) for MEFs (CA-137 Program) or SE Cell line Kit (V4XC-1024, Lonza Bioscience) for MDA-MB-137 cells (Program DN-100). A total of 24 h after transfection, the cells were replated to microscopy culture dishes or collected for lysate after 48 h.

### CRISPR–Cas9 gene knockout

The genes were deleted by nucleofecting (SE Cell line 4D-Nucleofector kit Lonza V4XC-1024). Ribonucleoprotein complexes (RNPs) consisting of pooled sgRNAs conjugated with Cas9. The RNPs were prepared by

coincubating 500 pmol of sgRNA pools (for EIF2AK3) with 100 pmol of Cas9 2NLS (Synthego) and introducing the RNPs into MDA-MB-157 using the DN-100 program in Lonza 4D-Nucleofector. A total of 48 h after transfection, the cells were collected for western blot analysis and expanded.

### Electron microscopy

MEF $PERK^{WT}$ and $PERK^{KO}$ expressing HRP-KDEL-myc were fixed on coverslips with 1.3% glutaraldehyde in 0.1 M cacodylate buffer and washed in 0.1 M ammonium phosphate (pH 7.4) buffer for 1 h, and HRP was visualized with 0.5 mg $ml^{-1}$ DAB and 0.005% $H_2O_2$ in 0.1 M ammonium phosphate (pH 7.4) buffer, following the same procedures as described in ref. 37. The untreated MEFs, the MEFs pretreated with RSL3 for 15 min or RSL3 cotreated with Fer-1 for 15 min were fixed with 1.25% (vol/vol) glutaraldehyde in 0.1 M sodium cacodylate at pH 7.4 for 1 h at RT. Thin sections were imaged on a Tecnai-20 electron microscope (Philips-FEI), at the Bioimaging facility of the Department of Biology, University of Padova.

### PLA

A PLA was performed using Duolink In Situ Red Started Kit Mouse/Rabbit (Duolink In Situ Detection Reagents Red (Sigma-Aldrich, DUO92008); Duolink In Situ PLA Probe Anti-Mouse MINUS (Sigma-Aldrich, DUO92004); Duolink In Situ PLA Probe Anti-Rabbit PLUS (Sigma-Aldrich, DUO92004); Duolink In Situ Mounting Medium with DAPI (Sigma-Aldrich, DUO82040)) according to the manufacturer's instructions. Briefly, after treatment with RSL3 at the different timepoints, MEFS were fixed with 4% PFA and permeabilized with 0.1% Triton and further processed as described in ref. 37. The PLA images were acquired with an Olympus IX73 (Olympus), cellSens Dimension acquisition software and 63× magnification.

### Subcellular fractionation

The MEFs were treated with RSL3 or cotreated with Fer-1 to block lipid peroxidation, and after the specified period (30 min or 6 h), the cells were collected and the resulting pellet after centrifugation (600–800*g* for 5 min at RT) was resuspended in 5 ml of starting buffer 1 containing 225 mM mannitol, 75 mM sucrose and 30 mM Tris–HCl and 0.1 mM ethylene glycol-bis(β-aminoethyl ether)-*N*,*N*,*N*′,*N*′-tetraacetic acid (EGTA), pH 7.4 and homogenized. The unbroken cells and nuclei were removed by centrifugation of the cell homogenate at 600*g* for 5 min (at 4 °C). The crude mitochondrial fraction (mito crude) was pelleted by centrifuging the supernatant at 7,000*g* for 10 min at 4 °C. The crude mitochondria were resuspended in starting buffer (SB) (225 mM mannitol, 75 mM sucrose and 30 mM Tris–HCl, pH 7.4) and after other two sequential centrifugations (7,000*g* and 10,000*g* for 10 min at 4 °C), the obtained pellet was resuspended in 1 ml of mitochondria resuspending buffer MRB (250 mM mannitol, 5 mM HEPES buffer and 0.5 mM EGTA), layered on top of a percoll gradient (30% and 15%) and spun down at 95,000*g* for 40 min (using a Beckman ultracentrifuge, rotor SW41), to separate EMCSs from the pure mitochondria (mito pure). Further ultracentrifugation (70Ti rotor, 100,000*g* for 1 h at 4 °C) was required to obtain the pellet of the EMCS fraction.

### Lipidomics and redox lipidomics

After isolation of the subcellular fractions from 6 h RSL3 (0.125 μM) treatment or RSL3 (0.125 μM) cotreated with Fer-1 (1 μM) MEFs, we analysed through liquid chromatography–mass spectrometry lipidomics the presence of oxidative PL forms. This procedure was conducted according to the published protocol cited in ref. 65.

After transient transfection of MEFs with AKAP1–mRFP control or 9xL spacer, the cell pellets were analysed through mass spectrometry-based lipidomic using the Lipometrix platform (KU Leuven). This procedure was conducted according to the published protocol in ref. 37.

### MitoPerox and Bodipy C11 FACS analysis

After ferroptosis treatments at different timepoints, the cells were washed, trypsinized, collected and then stained for MitoPerox (400 nM) or Bodipy 581/591 C11 (2.5 μM) for 30 min. The samples were then washed two times with cold PBS and processed using BD FACS Canto IIBD Canto II or Attune flow cytometer. An analysis was performed using FlowJo software.

### Cell death detection

The cells were incubated with RSL3 or IKE at the concentrations and for the time indicated in the legends. When transiently or virally transfected, MEF and MDA-MB-157 cells were treated with 0.5 μM RSL3 while HCC1143 and Hs578T cells were treated with 3 μM and 1 μM RSL3, respectively. To assess the specificity of the cell death, the cells were preincubated with the pan-caspase inhibitor ZVAD (30 μM) or the necroptosis inhibitor or Nec1s (30 μM) 2 h before the treatments, while the iron chelator DFO (50 μM), the radical-trapping antioxidant Fer-1 (1 μM) or the reducing agent BME (50 μM) were added in the medium together with RSL3/IKE. The cell death was measured after 24 h of staurosporine (1 μM) treatment and 48 h after CDDP (100 μM) treatment of MEFs. The cell death was evaluated by the fluorescent viability dye Sytogreen and quantified either by using the Flexstation plate reader at 488/523 nm (FlexStation; Molecular Devices) or by counting the number of SYTOX-Green-positive cells normalized on the total amount of cells before the treatment using an Olympus IX73 (Olympus) or by the Operetta High Content imaging system (PerkinElmer, University of Padova) with incubator and $CO_2$ chamber. When the cells were manually counted, multiple areas in the same well were acquired and analysed at each timepoint per condition and biological replicate.

### Live cell imaging

Time-lapse 3D live cell imaging was acquired with the high-resolution confocal Zeiss LSM 880–Airyscan (Cell and Tissue Imaging Cluster), ZEN 2.3 SP1 acquisition software, objective 63×, numerical aperture 1.4 oil, equipped with temperature (37 °C), $CO_2$ and a humidity-controlled incubator. The cells were imaged in Krebs solution (150 mM NaCl, 5.9 mM KCl, 1.2 mM MgCl2, 11.6 mM HEPES (pH 7.3), 11.5 mM glucose and 1.5 mM $CaCl_2$). For mitochondrial and EMCS live imaging, the cells were incubated with MitoTracker green or Far Red 20 nM (M7514, Thermo Fisher Scientific) for 30 min and washed in the physiological Krebs solution (39.47 g NaCl, 2.3 g KCl,11.88 g glucose monohydrate,14.3 g HEPES,1.26 g $MgCl_2$·6aq, 3.97 g EGTA, 1.15 g $CaCl_2$·2aq and 5,220 ml MQ, pH 7.4) and then imaged with a Zeiss LSM 880–Airyscan (Cell and Tissue Imaging Cluster). RSL3 or IKE were added directly to the dish after images of the untreated condition were taken. The same imaging procedure was conducted for MEFs transfected with AKAP1–mRFP control or 9xL spacer or BFP–KDEL and acquired as well with the Zeiss LSM 880–Airyscan (Cell and Tissue Imaging Cluster, 63× magnification, equipped with temperature, $CO_2$ and humidity-controlled incubator. MitoSOX staining 5 μM, Bodipy 581/591 C11 2.5 μM or Liperfluo (10 μM) were preincubated for 30 min and then costained with MitoTracker Far Red 20 nM following the same staining and imaging procedure as described above.

### Immunostaining

After inducing ferroptosis, the cells were fixed in PFA 4% for 10 min. After washing, the cells were permeabilized in 0.1% saponin in 5% normal goat serum for 1 hr at RT. The primary antibodies were incubated 1:100 diluted in 0.1% saponin and incubated ON at 4 °C. The secondary antibodies were incubated in anti-rabbit/mouse−488 nm−and anti-mouse/rabbit−647 nm−for 1 h at RT. The cells were incubated with DAPI (1:1,000) in PBS for 10 min and successively added prolong gold in PBS and stored at 4 °C. The images were taken with the Zeiss LSM 880–Airyscan (Cell and Tissue Imaging Cluster, 63× magnification).

### $Ca^{2+}$ imaging

MEFs transiently transfected with mito-R-GECO1 were loaded with 3 µM Cal520 at RT in modified Krebs solution (150 mM NaCl, 5.9 mM KCl, 1.2 mM MgCl2, 11.6 mM HEPES (pH 7.3), 11.5 mM glucose and 1.5 mM CaCl2) for 30 min. This was followed by a de-esterification step in the absence of extracellular Cal520 for 30 min at RT. The cells were washed and were added to Krebs solution without $CaCl_2$ and EGTA 3 mM to chelate the extracellular $Ca^{2+}$. The cytosolic $Ca^{2+}$ release (Cal520, excitation 493, emission 515) and mitochondrial $Ca^{2+}$ uptake (mito-R-GECO1, excitation 560, emission 584) were monitored in live cell imaging using a Zeiss Axio Observer Z1 inverted microscope. The baseline was recorded for 60 s before the addition of RSL3 for 15 min followed by $Ca^{2+}$ triggers (ATP, 100 µM).

### FEMP imaging and high-throughput EMCS measurements

$PERK^{WT}$ and $PERK^{KO}$ MEFs were infected with an adenovirus carrying the FEMP probe complementary DNA at a multiplicity of infection of 10. After 24 h, the cells were imaged using an Operetta CLS High Content imaging system (Revvity) with the following filter settings: CFP (excitation 410–430, emission 460–500), YFP (excitation 490–510, emission 520–560) and YFP FRET (excitation 410–430, emission 520–560). RSL3/RSL3 + Fer-1/RSL3 + DFO were added to the wells after measuring the baseline FRET intensity of the untreated samples. To image the maximum FRET intensity (FRETmax), the cells were treated with 100 nM rapamycin for 15 min. The images were analysed using Harmony 3.5 image analysis software (Revvity). The YFP channel was chosen to mark the region of interest, and around each region of interest, a second boundary was drawn to measure the background intensity. The cells pretransfected with AKAP1–mRFP, AKAP1 (34-63)-linker, 9x-mRFP (9xL spacer) or AKAP1 (34–63)-mRFP-yUBC6 (OMM–ER linker) were selected on the basis of RFP-positive cells. FRETbasal, FRETmax and FRET ratio were calculated as previously described[24]. The MDA-MB-157 cells of the LAR subtype and the non-LAR TNBC cells, Hs578T, HCC1143 and HCC1937 were seeded in a 384-well microplate (PhenoPlate, PerkinElmer) and the next day were transfected with the Sec16ß–EGFP plasmid using the jetOPTIMUS transfection reagent (Polyplus). A total of 24 h after transfection, the cells were incubated with 100 nM MitoTracker Far Red for 30 min at 37 °C in serum-free media, washed once and imaged at 37 °C and 5% $CO_2$ using the Operetta CLS High Content Analysis System (Revvity) with a 63× water flow objective. The images were analysed in high-throughput mode using Harmony (Revvity).

### Gene set expression analysis for EMCS from a publicly available dataset

The bulk RNAseq expression matrix for 360 samples from FUSCC TNBC cohort[66] was downloaded from The National Omics Data Encyclopedia (NODE: OEP000155; GEO: GSE118527). A total of 258 samples matched with lipidomics analysis were used for further analysis. The lipidomic data ($log_2$ transformed abundance of MS2 annotated lipids in TNBC samples) were downloaded from the supplemental information of the article[54]. The bulk RNAseq expression counts were downloaded for 158 The Cancer Genome Atlas Breast Invasive Carcinoma (TCGA -BRCA), samples of patients with TNBC using TCGA biolinks package in R (TCGA breast cancer data: (https://portal.gdc.cancer.gov); TCGA-BRCA, dbGaP accession phs000178). The patient samples were labelled as BLIS, IM, LAR and MES, representing distinct subtypes of TNBC, as outlined in the previously published article[54]. To calculate the EMCS score, we downloaded a set of gene from this work[55] and used only genes annotated as EMCS. We calculated two sets of score, one using a full gene list and the other using a manually curated gene list based on previously available literature. We calculated the enrichment score for the signature gene set using an ssGSEA for each patient sample using the R Bioconductor package GSVA (version 1.49.0). The enrichment score for EMCS was analysed across different subtypes of TNBC as defined by Yang et al.[54], and the statistical significance was calculated using Wilcoxon's test.

### Image processing, analysis and statistics

For two-dimensional (2D) and 3D live imaging, an EMCS area or volume analysis was performed using ImageJ/Fiji software (http://imagej.nih.gov/ij/). The masked area and volume for the ER and mitochondria were created using IJ IsoData threshold method, and their area and volume were analysed. The EMCS mask was created by the overlapping region between ER and mitochondria (EMCS) (ImageCalculator).

The area outside ER and mitochondria was created by Bodipy C11 Red mask minus ER plus mitochondria masks. The per cent of EMCS was measured as a ratio of EMCS area or volume and ER area or volume. We measured the intensity of oxidized Bodipy 581/591 C11 (green) on total Bodipy 581/591 C11 signal (red) or for Liperfluo the integrated density (IntDen) and normalized on total cellular volume. A colocalization analysis was performed using Mander's overlap coefficient above the threshold value defined using Otsu on the oxidized Bodipy 581/591 C11 (green) and Liperfluo in the EMCSs, mitochondrial and ER masks (Mander's coefficient, JacoB plugin, Fiji). For a 3D rendering representation, Imaris 10.1 software was used to visualize the surfaces of the different channels (Liperfluo, ER and mitochondria) together with the EMCS mask. For live imaging of MEFs costained with MitoSOX green and MitoTracker Far Red, the intensity of MitoSOX on MitoTracker Far Red was measured. The mitochondrial morphology was measured with Imaris 10.1. The mitochondrial fragmentation was calculated using the volume statistic features and measured as a fragmentation index (from 0 to 1), equal to the sum of small volumes normalized on the total volume. The PLA images were analysed manually with 'Threshold' and 'Analyze particles' commands from ImageJ/Fiji Software. The number of EMCSs per mitochondria in HRP-stained Epon sections of $PERK^{WT}$ and $PERK^{KO}$ cells were quantified using ImageJ/Fiji Software. TEM morphometric measurements in MEFs untreated and after treatment or cotreatment with RSL3 or RSL3 + Fer-1 were carried out using ImageJ/Fiji Software. For calculations of mitochondria-ER distance, 70 images per condition were considered, and the minimal distance of the ER located in a 30 nm radius from the considered mitochondria was computed. The ERMICC was calculated as previously described[24].

All data are represented as the mean ± standard error of the mean (s.e.m.). The statistical significance between two groups was determined by a standard unpaired two-sided *t*-test with *F*-testing or a one-sample *t*-test. The data distribution was assumed to be normal, but this was not formally tested. The statistical significance between multiple groups was determined by a one-way analysis of variance (ANOVA) to ensure comparable variance, then individual comparisons were performed by Tukey's or Sidak's post hoc test. The analysis was done in Prism v9.0f, GraphPad. The asterisk represents a $P$ value <0.05, $^{**}P < 0.01$, $^{***}P < 0.001$ and $^{****}P < 0.0001$, where a $P$ value <0.05 is considered significant. No statistical methods were used to predetermine the sample sizes, but our sample sizes are similar to those reported in previous publication[37]. The investigators were not blinded to allocation during experiments and outcome assessment.

### Reporting summary

Further information on research design is available in the Nature Portfolio Reporting Summary linked to this article.

## Data availability

Data supporting the findings of this work are available in this study and its Extended data figures and the Supplementary Information. All the data generated and analysed in this study are available from the corresponding author upon request. Source data are provided with this paper.

## References

64. Menegollo, M. et al. Multistate gene cluster switches determine the adaptive mitochondrial and metabolic landscape of breast cancer. *Cancer Res.* **84**, 2911–2925 (2024).
65. Kagan, V. E. et al. Oxidized arachidonic and adrenic PEs navigate cells to ferroptosis. *Nat. Chem. Biol.* **13**, 81–90 (2017).
66. Jiang, Y.-Z. et al. Genomic and transcriptomic landscape of triple-negative breast cancers: subtypes and treatment strategies. *Cancer Cell* **35**, 428–440.e5 (2019).

## Acknowledgements

The authors thank G. Hajnóczky for providing AKAP1–mRFP, AKAP1 (34-63)-9x-mRFP-yUBC6 (9xL spacer) and mAKAP1 [34–63]-mRFP-yUBC6 (OMM–ER linker), P. Pinton for providing S1R–GFP, J. Van Asselberghs (Research Group for Neurobiology and Gene Therapy, KU Leuven) for producing the PERK K622A-myc plasmid and D. Ron for providing $PERK^{WT}$ and $PERK^{KO}$ MEF cells. The Zeiss LSM 880–Airyscan from the Cell and Tissue Imaging Cluster—was supported by Hercules AKUL/15/37_GOH1816N and FWO G.0929.15 to P. Vanden Berghe, KU Leuven and the Bioimaging core VIB–KU Leuven, S. Munck. We thank the Bioimaging facility of the Department of Biology (HiTS and Electron Microscopy Facility University of Padova) and the Institute of Integrative Cell Biology, Paris for the EM analysis. We thank J. Dehairs, F. Vanderhoydonc and N. Ravoet from the lipidomics analysis (KU Leuven, Lipometrix platform). M.L.S. is funded by the European Union's Horizon 2020 Research and Innovation programme under the Marie Sklodowska-Curie grant (grant no. 675448) and by the Flemish Research Foundation (FWO-Vlaanderen; grant no. V431023N). A.D. is supported by the postdoctoral fellowship 2023 and 2024 awards from Fondazione Umberto Veronesi. F.G. is supported by the Agence Nationale de la Recherche (ANR-22-CE11-0024-01/MADE), the AFM Telethon (Project AFM 23778) and as part of France 2030 programme ANR-11-IDEX-0003. G.B. is supported by the KU Leuven Research Council (grant nos. C14/19/099 and AKUL/19/34), grants by the FWO-Vlaanderen (grant nos. G081821N and G094522N) and the Central European Leuven Strategic Alliance (grant no. CELSA/23/032). P.A. and G.B. are partners of the FWO Scientific Research Network CaSign (W0.014.22N). L.S. is supported by Italian Science Fund Advanced Grant FIS00001005, Ministry of University and Research, AIRC IG27307, PRIN 20222Y9X43, Ministry of University and Research. V.K is supported by NIH grants AI156924, AI156923, CA266342, CA243142, NS061817 and HL174611. P.A. is supported by the C1 KU Leuven Consortium InterAction C14/21/095, grants by the Flemish Research Foundation (FWO-Vlaanderen; grant nos. G0A3320N and G094922N), the EOS MetaNiche consortium no. 40007532 and the iBOF/21/053 ATLANTIS consortium. Open Access funding is provided by KU Leuven Libraries.

## Author contributions

M.L.S. and P.A. designed the experiments. M.L.S. performed the majority of all the experiments presented in the manuscript. LC–MS/MS lipidomic analysis and data interpretation were carried out by Y.T., V.T., H.B. and V.K. J.S. helped with lipidomic analysis on the Lipometrix platform (KU Leuven). A.D. created the FEMP adenovirus. FRET imaging was performed and interpreted by M.L.S. with the assistance from A.D. and L.S. E.V. helped with the execution of part of the experiments. S.M. performed the gene set expression analysis for EMCS from publicly available dataset. The $Ca^{2+}$ measurements were performed and interpreted by M.L.S. with the assistance of R.L.R. and G.B. F.G. acquired the HRP-KDEL-stained EM images. The imaging analysis was performed by M.L.S. with the assistance of B.P. B.P. wrote the scripts for the 2D image analysis. The EM images were acquired at the Bioimaging facility of the Department of Biology, University of Padova and the Institute of Integrative Cell Biology, Paris. P.A. supervised the research and interpreted the results with M.L.S. Both P.A. and M.L.S. wrote the manuscript. P.A. oversaw the project and acquired funding. All authors discussed the results and commented on the manuscript.

## Competing interests

The authors declare no competing interests.

## Additional information

**Extended data** are available for this paper at https://doi.org/10.1038/s41556-025-01668-z.

**Supplementary information** The online version contains supplementary material available at https://doi.org/10.1038/s41556-025-01668-z.

**Correspondence and requests for materials** should be addressed to Patrizia Agostinis.

**Peer review information** *Nature Cell Biology* thanks the anonymous reviewers for their contribution to the peer review of this work. Peer reviewer reports are available.

https://doi.org/10.1038/s41556-025-01668-z

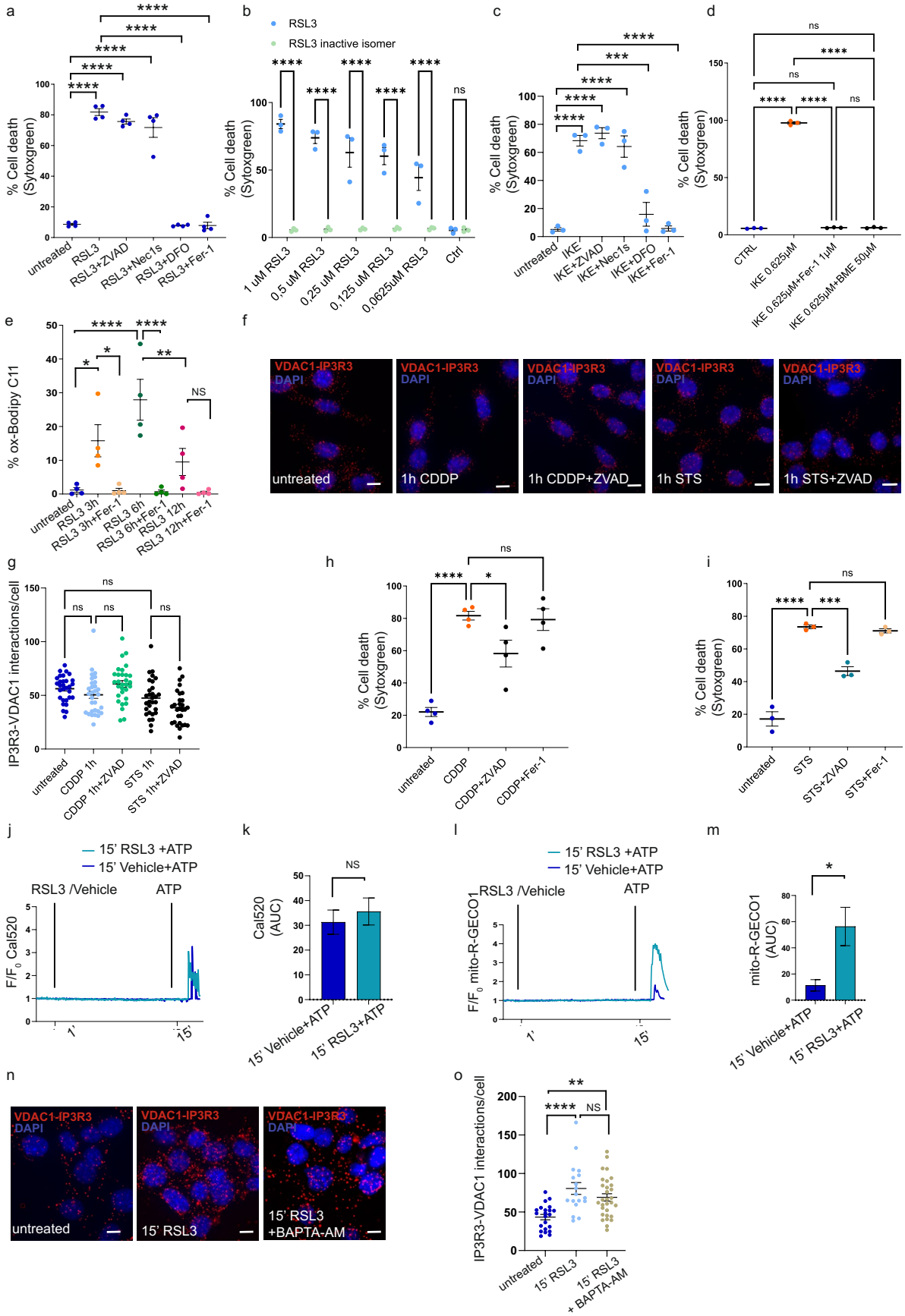


**Extended Data Fig. 1 | See next page for caption.**

https://doi.org/10.1038/s41556-025-01668-z

**Extended Data Fig. 1 | EMCS early expansion is not triggered by Ca2+ remodeling, and it is exclusive to ferroptosis cell death. a**, % cell death (Sytoxgreen positive cells) of MEFs treated for 24 h with RSL3 (0.125 μM), in the absence or presence of Z-Val-Ala-DL-Asp(OMe)-fluoromethylketone (ZVAD, 30 μM), Necrostatin-1s (Nec1s, 30 μM), deferoxamine mesylate salt (DFO, 50 μM) or ferrostatin 1 (Fer-1, 1 μM). (n = 4 biological replicates, 3 wells per condition per biological experiment were analyzed). **b**, % cell death (Sytoxgreen positive cells) of MEFs treated for 24 h with RSL3 or the inactive diastereomer (1 R,3 R) RSL3 (1 μM, 0.5 μM, 0.25 μM, 0.125 μM and 0.0625 μM). (n = 3 biological replicates, 3 wells per condition per biological experiment were analyzed). **c**, % cell death (Sytoxgreen positive cells) of MEFs treated for 24 h with IKE (0.625 μM), in the absence or presence of Z-Val-Ala-DL-Asp(OMe)-fluoromethylketone (ZVAD, 30 μM), Necrostatin-1s (Nec1s, 30 μM), deferoxamine mesylate salt (DFO, 50 μM) or ferrostatin 1 (Fer-1, 1 μM). (n = 3 biological replicates, 3 wells per condition per biological experiment were analyzed). **d**, % cell death (Sytoxgreen positive cells) of MEFs treated for 24 h with IKE (0.625 μM) in the absence or presence of Fer-1 (1 μM) or beta-mercaptoethanol (BME) (50 μM). (n = 3 biological replicates, 3 wells per condition per biological experiment were analyzed). **e**, % oxidized Bodipy C11 (ox-Bodipy C11) of untreated MEFs and, at 3 h, 6 h, and 12 h after RSL3 (0.125 μM) and Fer-1 (1 μM), measured as a shift in Bodipy C11 red/green fluorescence. (n = 4 biological replicates). **f, g**, Representative images (**f**) of in situ PLA in MEFs and quantification (**g**) of N of dots corresponding to IP3R3-VDAC1 interaction per nucleus of untreated cells, and cells treated for 1 h with staurosporine (STS, 1 μM), cisplatin (CDDP, 100 μM) or cotreated with -Val-Ala-DL-Asp(OMe)-fluoromethylketone (ZVAD, 30 μM). (n = 3 biological replicates, n = 30 images for untreated, n = 30 images for CDDP 1 h, n = 30 images for CDDP 1 h+ZVAD, n = 30 images for STS 1 h, n = 29 images for STS 1 h+ZVAD and quantified as described in Fig. 1d). **h,i**, % cell death (Sytoxgreen positive cells) of MEFs treated for 48 h with cisplatin (CDDP, 100 μM) (**h**) or 24 h with staurosporine (STS, 1 μM) (**i**) treatment, in the absence or presence of Val-Ala-DL-Asp(OMe)-fluoromethylketone (ZVAD, 30 μM) or ferrostatin 1 (Fer-1, 1 μM). (n = 3 biological replicates, 3 wells per condition per biological experiment were analyzed). **j, k**, Representative fluorescent traces (**j**) and AUC (**k**) of the cytosolic Ca2+ release after ATP (100 μM) treatment in cells stained with Cal520 and pretreated for 15′ with RSL3 (0.5 μM) or vehicle. (n = 3 biological replicates, n = 26 for 15′ vehicle, n = 41 for 15′ ATP). **l, m**, Representative fluorescent traces (**l**) and AUC (**m**) of the mitochondrial $Ca^{2+}$ uptake after ATP (100 μM) treatment in cells transiently transfected with mito-R-GECO1 and pretreated for 15′ with RSL3 (0.5 μM) or vehicle. (n = 3 biological replicates, n = 65 for 15′ vehicle, n = 110 for 15′ ATP). **n, o**, Representative images (**n**) of in situ PLA of MEFs and quantification (**o**) of N of dots corresponding to IP3R3-VDAC1 interaction per nucleus in untreated cells, and in cells treated for 15′ with RSL3 (0.125 μM) or cotreated with RSL3 (0.125 μM) and BAPTA-AM (10 μM). (n = 3 biological replicates, n = 22 images for untreated, n = 18 images for 15′ RSL3, n = 30 images for 15′ RSL3 + BAPTA and quantified as described in Fig. 1d). All quantitative data are mean ± SEM. In **a, c, d, e, g, h, i, o**, statistical significance was determined by one-way ANOVA, Tukey (**a**, **c**, **d**, **o**) or Sidak (**e**, **g**, **h**, **i**) post-hoc test. In **b**, statistical significance was determined by two-way ANOVA, Sidak post-hoc test. In **k, m**, statistical significance was determined by two-sided unpaired t-test. NS, not significant ($P > 0.05$), *$P \leq 0.05$, **$P < 0.01$, ***$P < 0.001$. Source numerical and statistical data are provided.

https://doi.org/10.1038/s41556-025-01668-z

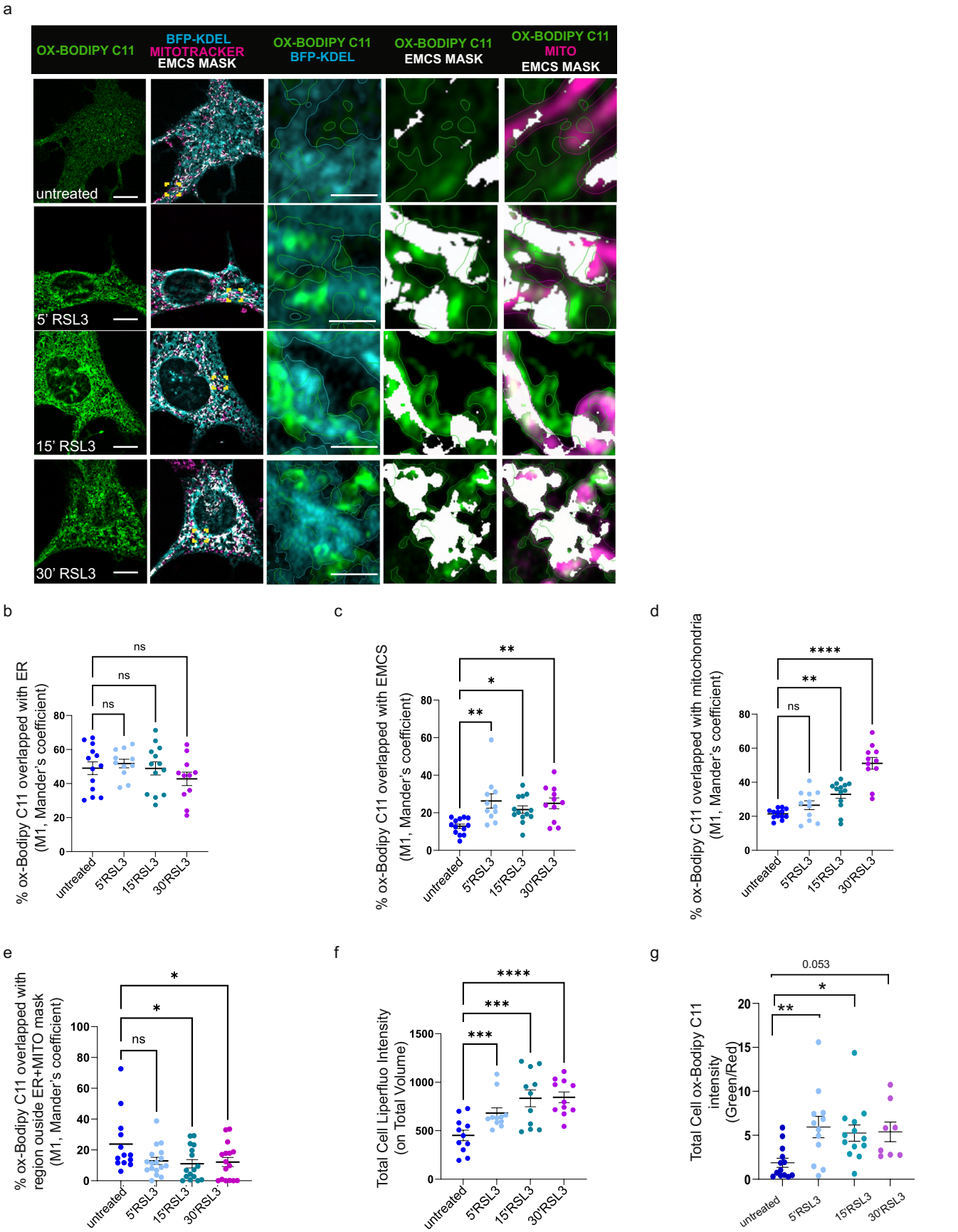


**Extended Data Fig. 2 | See next page for caption.**

https://doi.org/10.1038/s41556-025-01668-z

**Extended Data Fig. 2 | The phospholipid peroxidation sensor Bodipy C11 colocalizes primarily with EMCSs and subsequently with the mitochondria.** **a**, Representative 2D images of MEFs transiently transfected with the ER marker BFP-KDEL (cyan) and stained with MitoTracker Far Red (magenta) and Bodipy C11 (green) at time 0 and at 5', 15', 30' after RSL3 (0.5 µM). EMCS masked area, representing colocalization of the ER and mitochondria, is indicated as white. Magnified images represent respectively ox-Bodipy together with i) ER surface, ii) EMCS mask and iii) mitochondrial surfaces together with EMCS mask. Scale bar, 10 µm. Zoom, 1 µm. **b-e**, Colocalization (% M1, Mander's coefficient) of oxidized Bodipy C11 (ox-Bodipy C11) (green) signal in the ER, EMCS mask, mitochondria and the residual cellular region outside the ER + mitochondrial masks, at time 0 and 5, 15, 30' after RSL3 (0.5 µM). (n = 3 biological replicates). **f**, Total Cell Liperfluo intensity normalized on total cellular volume (MFI) at time 0 and 5, 15, 30' after RSL3 (0.5 µM). (n = 3 biological replicates). **g**, Total Cell ox-Bodipy C11 intensity (green) normalized on non-oxidized Bodipy C11 (red) at time 0 and 5, 15, 30' after RSL3 (0.5 µM). (n = 3 biological replicates). All quantitative data are mean ± SEM. In **b-e, g**, statistical significance was determined by one-way ANOVA, Dunnett post-hoc test. In **f**, statistical significance was determined by RM one-way ANOVA, Dunnett post-hoc test. NS, not significant ($P > 0.05$), *$P \leq 0.05$, **$P < 0.01$, ***$P < 0.001$. Source numerical and statistical data are provided.

https://doi.org/10.1038/s41556-025-01668-z

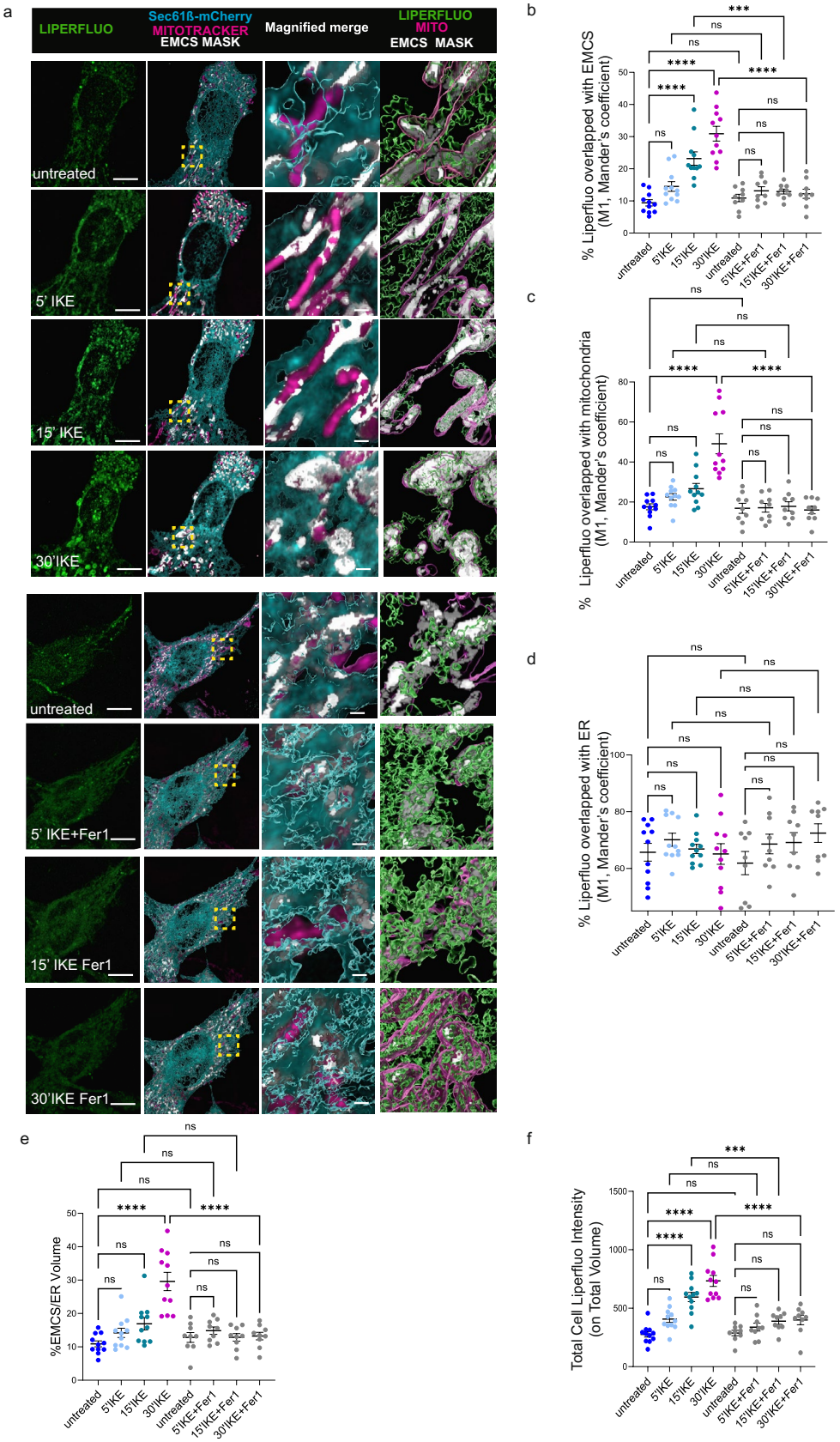


**Extended Data Fig. 3 | See next page for caption.**

https://doi.org/10.1038/s41556-025-01668-z

**Extended Data Fig. 3 | Time-lapse live imaging of phospholipid peroxides onset and propagation in IKE treated cells. a**, Representative volume-rendered 3D reconstructions of confocal *z*-stacks from time-lapse live images of MEFs transiently transfected with the ER marker Sec61ß-mCherry (cyan) and stained with MitoTracker Far Red (magenta) and Liperfluo (green) at time 0 and 5', 15', 30' after IKE (0.625 µM). EMCS masked volume, representing colocalization of the ER and mitochondria, is indicated as white. Magnified images represent respectively, i) merge of ER, mitochondrial surfaces and EMCS mask and ii) Liperfluo and mitochondrial surfaces together with EMCS mask. Scale bar, 10 µm. Zoom, 1 µm. **b-d**, Colocalization (% M1, Mander's coefficient) of Liperfluo in the EMCS (**b**), mitochondria (**c**), ER (**d**) masks at time 0 and 5', 15', and 30' after IKE (0.625 µM) without or with Fer-1 (1 µM) in MEFs. (n = 3 biological replicates). **e**, Quantification of the % EMCS normalized on the ER volume (Sec61ß-mCherry) at time 0 and 5', 15', 30' after IKE (0.625 µM) and cotreatment with Fer-1 (1 µM) in MEFs. **f**, Total Cell Liperfluo intensity normalized on total cellular volume (MFI) at time 0 and 5, 15, 30 'after IKE (0.625 µM) and cotreatment with Fer-1 (1 µM) in MEFs. (n = 3 biological replicates). (n = 3 biological replicates, the same cells (n = 11 IKE, n = 9 IKE+Fer-1) were acquired and analyzed at each timepoint per condition). Similar experiments and settings have been reproduced independently in Fig. 2, Fig. 4 and Supplementary Fig. 2. All quantitative data are mean ± SEM. In **b-f**, statistical significance was determined by one-way ANOVA, Sidak post-hoc test. NS, not significant ($P > 0.05$), *$P \leq 0.05$, **$P < 0.01$, ***$P < 0.001$. Source numerical and statistical data are provided.

https://doi.org/10.1038/s41556-025-01668-z

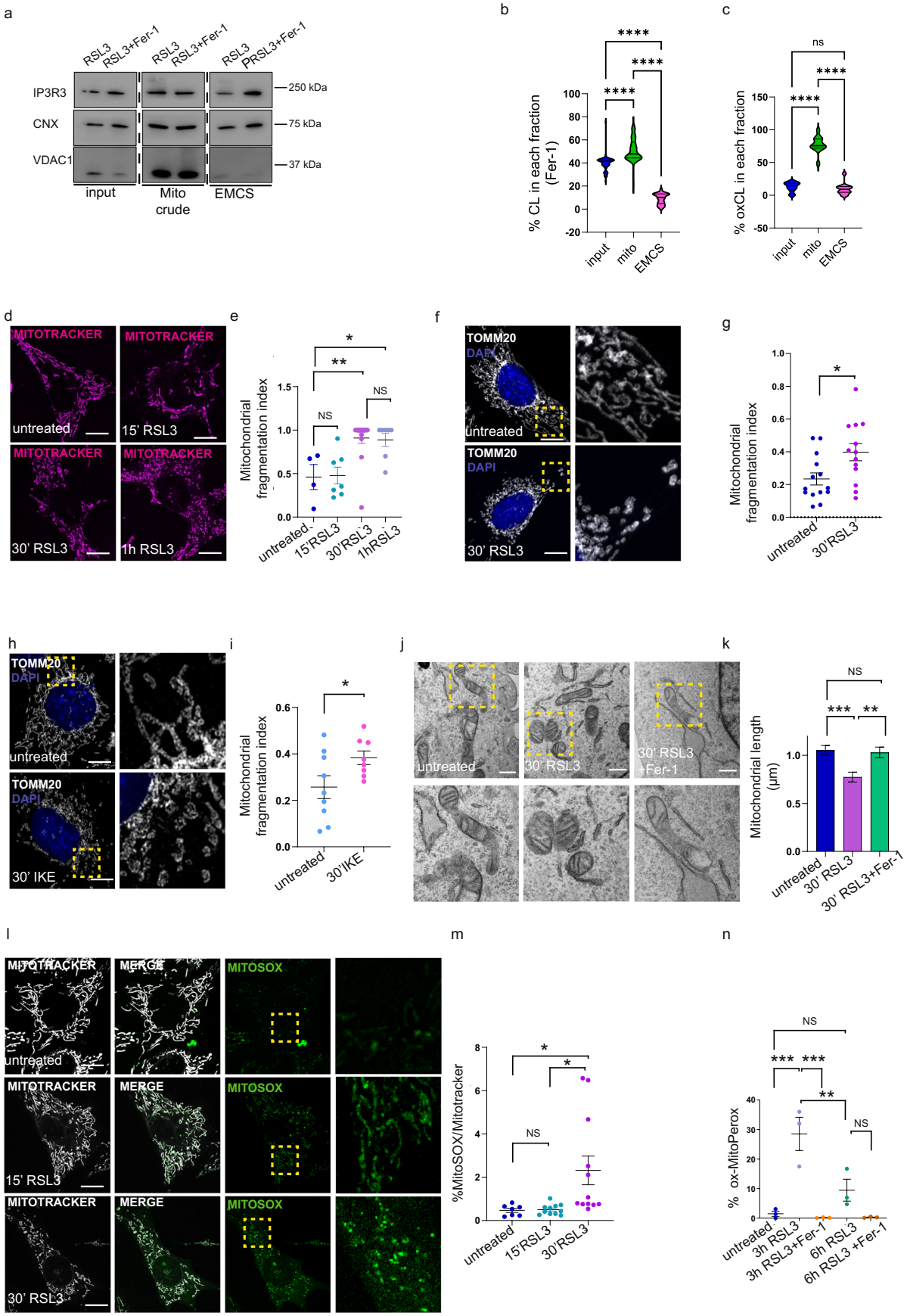


**Extended Data Fig. 4 | See next page for caption.**

https://doi.org/10.1038/s41556-025-01668-z

**Extended Data Fig. 4 | IKE and RSL3-mediated phospholipid peroxidation provokes mitochondrial fission. a**, Representative immunoblot of IP3R3, CNX, VDAC1 from inputs, crude mitochondrial fraction (mito crude) and EMCSs fractions of MEFs after 30′ RSL3 (0.125 μM). **b**, % cardiolipin (CL) in the input, EMCS, and mitochondrial fraction. (n = 3 biological replicates, 54 CL subspecies). **c**, % oxidized cardiolipin (oxCL) in the input, EMCS, and mitochondrial fraction and their fold changes compared to the corresponding condition co-treated with Fer-1 (1 μM). (n = 3 biological replicates, 12 CL subspecies). **d**, Representative images of live cells co-stained with MitoTracker Far Red in MEFs at time 0 and 15′, 30′ and 1 h after RSL3 (0.125 μM). Scale bar 10 μm. **e**, Mitochondrial fragmentation index in untreated cells and 15′, 30′ and 1 h after RSL3 (0.125 μM). (n = 3 biological replicates). (n = 4 untreated, n = 7 15′, n = 15 30′, n = 7 1 h) were acquired and analyzed from 3 independent biological replicates). Similar experiments and settings have been reproduced independently in Supplementary Fig. 6. **f**, Representative images of MEFs co-stained with TOMM20 and DAPI. Images were taken in fixed untreated cells and 30′ after RSL3 (0.125 μM). Scale bar, 10 μm. **g**, Mitochondrial fragmentation index in untreated cells and 30′ after RSL3 (0.125 μM). (n = 3 biological replicates). (n = 14 untreated, n = 13 30′) were acquired and analyzed from 3 independent biological replicates, similar experiments and settings have been reproduced independently in Supplementary Fig. 6). **h**, Representative images of MEFs co-stained with TOMM20 and DAPI. Images were taken in fixed untreated cells and 30′ after IKE (0.625 μM). Scale bar, 10 μm. **i**, Mitochondrial fragmentation index in untreated cells and 30′ after IKE (0.625 μM). (n = 2 biological replicates). (n = 8 untreated, n = 9 30′) were acquired and analyzed from 3 independent biological replicates. Similar experiments and settings have been reproduced independently in Supplementary Fig. 6). **j, k**, Representative TEM images of mitochondria at time 0 and 30′ after RSL3 (0.125 μM) and cotreatment with Fer-1 (1 μM) (**j**) and quantification of mitochondrial length (n = 70 images per condition, 5 cells per condition from 2 biological replicates). **l**, Representative images of live cells co-stained with MitoTracker Far Red and MitoSOX green in MEFs at time 0 and 15′ and 30′ after RSL3 (0.125 μM). Scale bar 10 μm. **m**, Quantification of the intensity of MitoSOX on MitoTracker. (n = 7 untreated, n = 11 15′, n = 12 30′) were acquired and analyzed from 3 independent biological replicates. Similar experiments and settings have been reproduced independently in Supplementary Fig. 6). **n**, % oxidized MitoPerox (ox-MitoPerox) in untreated, at 3 h and 6 h after RSL3 (0.125 μM) or RSL3 and Fer-1 (1 μM) treatment measured as a shift in MitoPerox. (n = 3 biological replicates). All quantitative data are mean ± SEM. In **b, c**, statistical significance was determined by RM one-way ANOVA, Tukey post-hoc test. In **e, k, m, n**, statistical significance was determined by one-way ANOVA, Sidak (**e**) or Tukey (**k**, **m**, **n**) post-hoc test. In **g, i**, statistical significance was determined by two sided unpaired t-test. NS, not significant ($P > 0.05$), *$P \leq 0.05$, **$P < 0.01$, ***$P < 0.001$. Source numerical and statistical data are provided.

https://doi.org/10.1038/s41556-025-01668-z

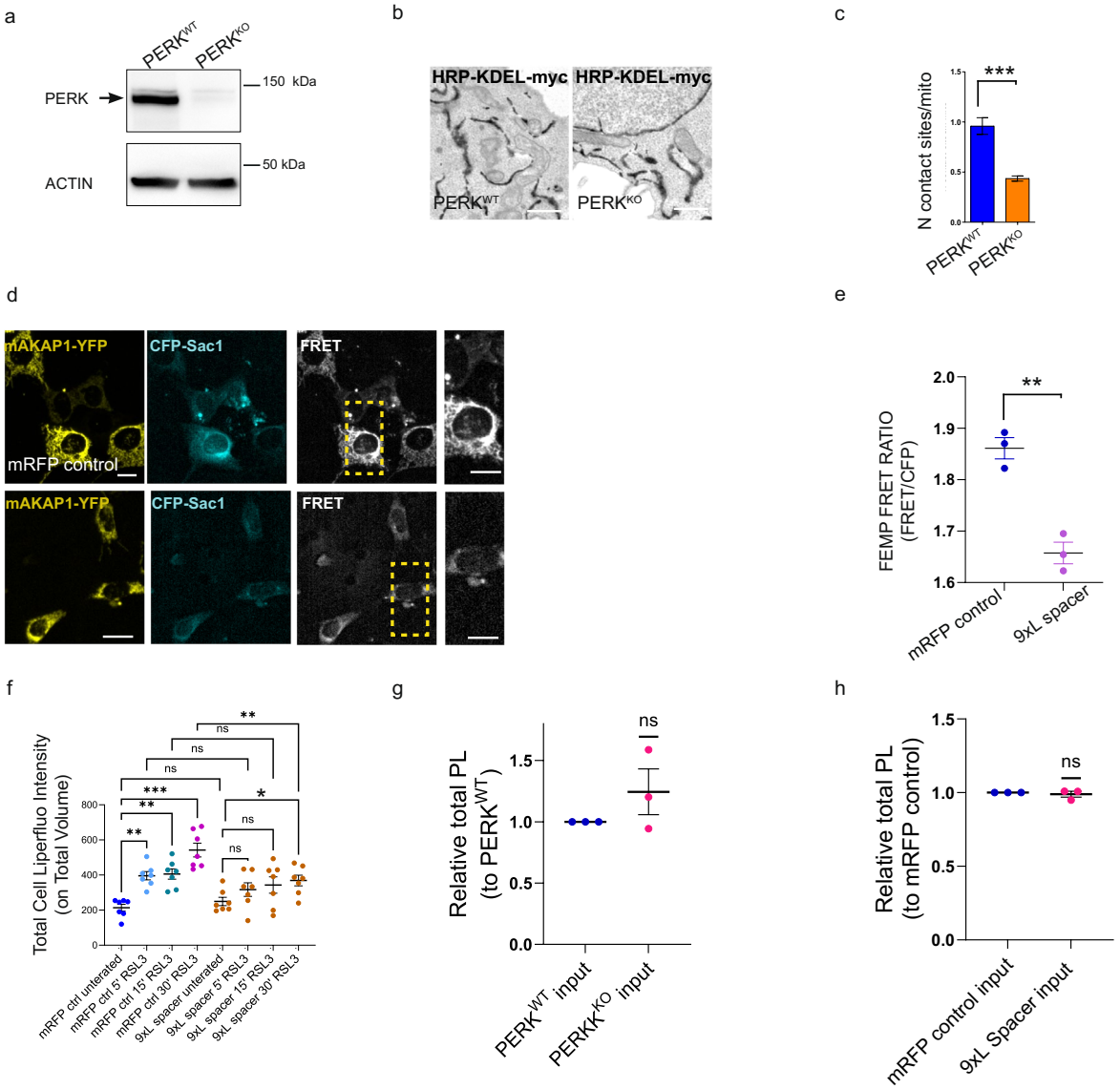


**Extended Data Fig. 5 | Spacing the EMCS does not alter the total cellular phospholipid abundance. a**, Representative immunoblot for PERK in PERK$^{WT}$ and PERK$^{KO}$ MEFs. ACTIN serves as loading control. Arrow indicates PERK. **b**, Representative TEM images of PERK$^{WT}$ and PERK$^{KO}$ MEFs transiently transfected with HRP-KDEL. **c**, quantification of the EMCSs N normalized on the mitochondrial surface in PERK$^{WT}$ and PERK$^{KO}$ MEFs. **d**, Representative FRET (Fluorescence Resonance Energy Transfer) live microscopy images of PERK$^{WT}$ MEFs transiently transfected with AKAP1-mRFP control or 9xL spacer and infected with FEMP probe (mAKAP1-YFP-Tav2-CFP-Sac1) in basal condition. Scale bar, 10 µm. Zoom, 10 µm. **e**, FRET-based ER-Mitochondria Proximity (FEMP) ratio in MEFs transiently transfected with AKAP1-mRFP control or 9xL spacer and transiently infected with FEMP probe and treated with RSL3 (0.5 µM). (n = 3 biological replicates, multiple areas in the same well were acquired and analyzed per each timepoint per condition per biological replicate). **f**, Total Cell Liperfluo intensity normalized on total cellular volume (MFI) at time 0 and 5, 15, 30 'after RSL3 (0.5 µM) treatment in MEFs transiently transfected with AKAP1-mRFP control or 9xL spacer. (n = 3 biological replicates). **g**, Relative levels of total PLs in PERK$^{KO}$ MEFs (to PERK$^{WT}$). (n = 3 biological replicates). **h**, Relative levels of total PLs in MEFs transiently transfected with 9xL spacer (to AKAP1-mRFP control). (n = 3 biological replicates). All quantitative data are mean ± SEM. In **c, e**, statistical significance was determined by two sided unpaired t-test. In **f**, statistical significance was determined by two-way RM ANOVA, Tukey post-hoc test. In **g, h**, statistical significance was determined by one sample t-test. NS, not significant ($P > 0.05$), *$P \leq 0.05$, **$P < 0.01$, ***$P < 0.001$. Source numerical and statistical data are provided.

https://doi.org/10.1038/s41556-025-01668-z

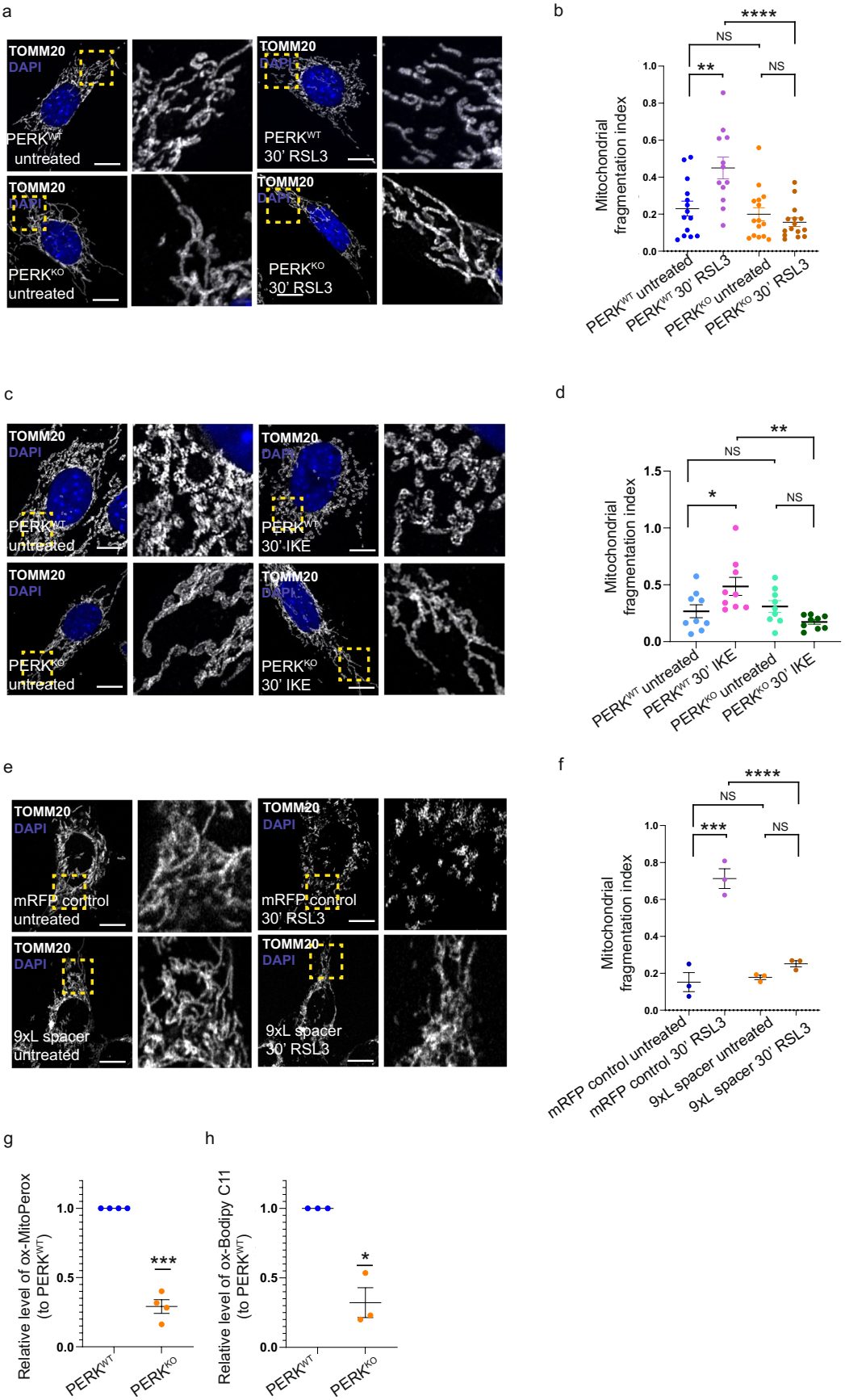


**Extended Data Fig. 6 | See next page for caption.**

https://doi.org/10.1038/s41556-025-01668-z

**Extended Data Fig. 6 | Altering EMCS integrity protects from ferroptosis-mediated mitochondrial fragmentation. a**, Representative images of co-stained MEFs with TOMM20 and DAPI in $PERK^{WT}$ and $PERK^{KO}$ MEFs. Images were taken in fixed untreated cells and 30′ after RSL3 (0.125 µM). Scale bar, 10 µm. **b**, Mitochondrial fragmentation index in untreated cells and 30′ after RSL3 (0.125 µM) in $PERK^{WT}$ and $PERK^{KO}$ MEFs. (n = 3 biological replicates). (n = 14 WT untreated, n = 12 WT 30′, n = 15 KO untreated, n = 15WT 30′) were acquired and analyzed from 3 independent biological replicates. Similar experiments and settings have been reproduced independently in Supplementary Fig. 4. **c**, Representative images of co-stained MEFs with TOMM20 and DAPI in $PERK^{WT}$ and $PERK^{KO}$ MEFs. Images were taken in fixed untreated cells and 30′ after IKE (0.625 µM). Scale bar, 10 µm. **d**, Mitochondrial fragmentation index in untreated cells and 30′ after IKE (0.625 µM) in $PERK^{WT}$ and $PERK^{KO}$ MEFs. (n = 2 biological replicates; n = 9 WT untreated, n = 9 WT 30′, n = 9 KO untreated, n = 9 WT 30′) were acquired and analyzed from 2 independent biological replicates. Similar experiments and settings have been reproduced independently in Supplementary Fig. 4. **e**, Representative images of live cells of $PERK^{WT}$ MEFs transiently transfected with AKAP1-mRFP control or 9xL spacer at T0 and 30′ after RSL3 (0.5 µM). Scale bar, 10 µm. **f**, Mitochondrial fragmentation index in MEFs transiently transfected with AKAP1-mRFP control or 9xL spacer in untreated cells and 30′ after RSL3 (0.5 µM). (n = 3 biological replicates). **g**, % oxidized MitoPerox (ox-MitoPerox) in $PERK^{WT}$ and $PERK^{KO}$ MEFs 3 h after RSL3 (0.125 µM) measured by FACS as a shift in MitoPerox fluorescence and relative to $PERK^{WT}$. (n = 4 biological replicates). **h**, % oxidized Bodipy C11 (ox-Bodipy C11) in $PERK^{WT}$ and $PERK^{KO}$ MEFs 6 h after RSL3 treatment measured by FACS as a shift in Bodipy C11 red/green fluorescence and relative to $PERK^{WT}$. (n = 3 biological replicates). All quantitative data are mean ± SEM. In **b, d**, statistical significance was determined by two-way ANOVA, Tukey post-hoc test. In **f**, statistical significance was determined by two-way RM ANOVA, Sidak post-hoc test. In **g, h**, statistical significance was determined by one sample t-test. NS, not significant ($P > 0.05$), *$P \leq 0.05$, **$P < 0.01$, ***$P < 0.001$. Source numerical and statistical data are provided.

https://doi.org/10.1038/s41556-025-01668-z

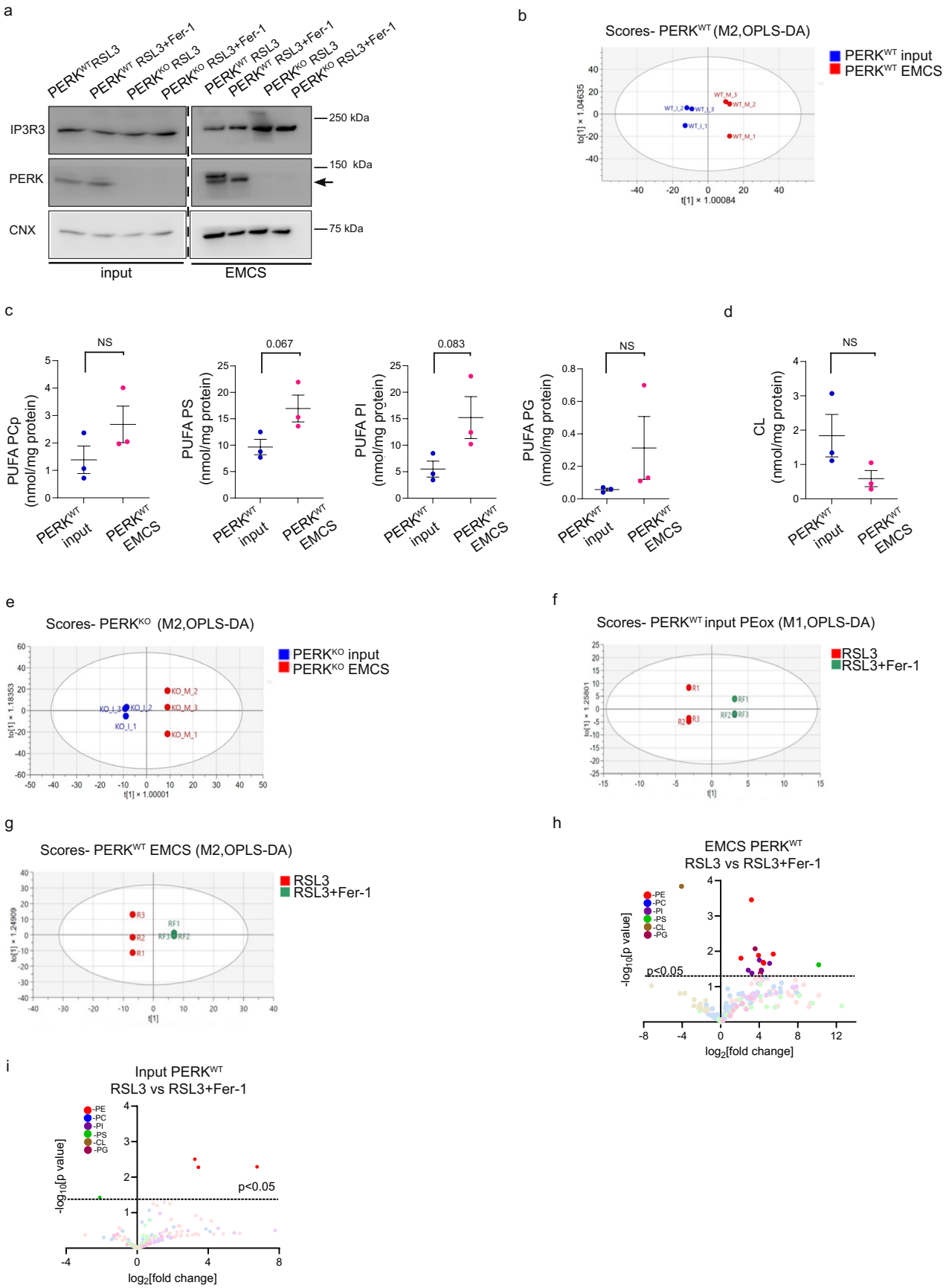


**Extended Data Fig. 7 | See next page for caption.**

https://doi.org/10.1038/s41556-025-01668-z

**Extended Data Fig. 7 | EMCS harbor phospholipids containing PUFAs that are prone to ferroptosis. a**, Representative immunoblot for IP3R3, PERK and CNX from inputs and EMCSs fractions of $PERK^{WT}$ and $PERK^{KO}$ MEFs after 6 h RSL3 (0.125 μM). Arrow indicates PERK. **b**, Orthogonal partial least squares discriminant analyses (OPLS-DA) score plots showing the separation of $PERK^{WT}$ input (RSL3+Fer-1) and $PERK^{WT}$ EMCS (RSL3+Fer-1) in two distinct groups. (n = 3 biological replicates). **c**, Total contents of polyunsaturated fatty acids (PUFAs) in four subclasses of PLs - PUFA-phosphatidylcholine plasmalogen (PCp), PUFA-phosphatidylserine (PS), PUFA-phosphatidylinositol (PI) and PUFA-phosphatidylglycerol (PG) in EMCSs vs input in $PERK^{WT}$ cells. (n = 3 biological replicates). **d**, Total contents of cardiolipin (CL) in EMCSs vs input in $PERK^{WT}$ cells. (n = 3 biological replicates). **e**, Orthogonal partial least squares discriminant analyses (OPLS-DA) score plots showing the separation of $PERK^{KO}$ input (RSL3+Fer-1) and $PERK^{KO}$ EMCS (RSL3+Fer-1) samples in two distinct groups. (n = 3 biological replicates). **f**, Orthogonal partial least squares discriminant analyses (OPLS-DA) score plots showing the separation of $PERK^{WT}$ input (RSL3) and $PERK^{WT}$ input (RSL3+Fer-1) samples in two groups. (n = 3 biological replicates). **g**, Orthogonal partial least squares discriminant analyses (OPLS-DA) score plot showing the separation of $PERK^{WT}$ EMCS (RSL3) and $PERK^{WT}$ EMCSs (RSL3+Fer-1) samples in two groups. (n = 3 biological replicates). **h**, Volcano plot showing the RSL3-induced changes in the content of oxidized PLs in EMCSs of $PERK^{WT}$ cells (RSL3 vs RSL3+Fer-1). (n = 3 biological replicates). **i**, Volcano plot showing the RSL3-induced changes in the content of oxidized PLs in input of $PERK^{WT}$ cells (RSL3 vs RSL3+Fer-1). (n = 3 biological replicates). In **c, d**, quantitative data are mean ± SEM. In **c, d**, statistical significance was determined by two sided unpaired t-test. NS, not significant ($P > 0.05$), *$P \leq 0.05$, **$P < 0.01$, ***$P < 0.001$. Source numerical and statistical data are provided.

https://doi.org/10.1038/s41556-025-01668-z

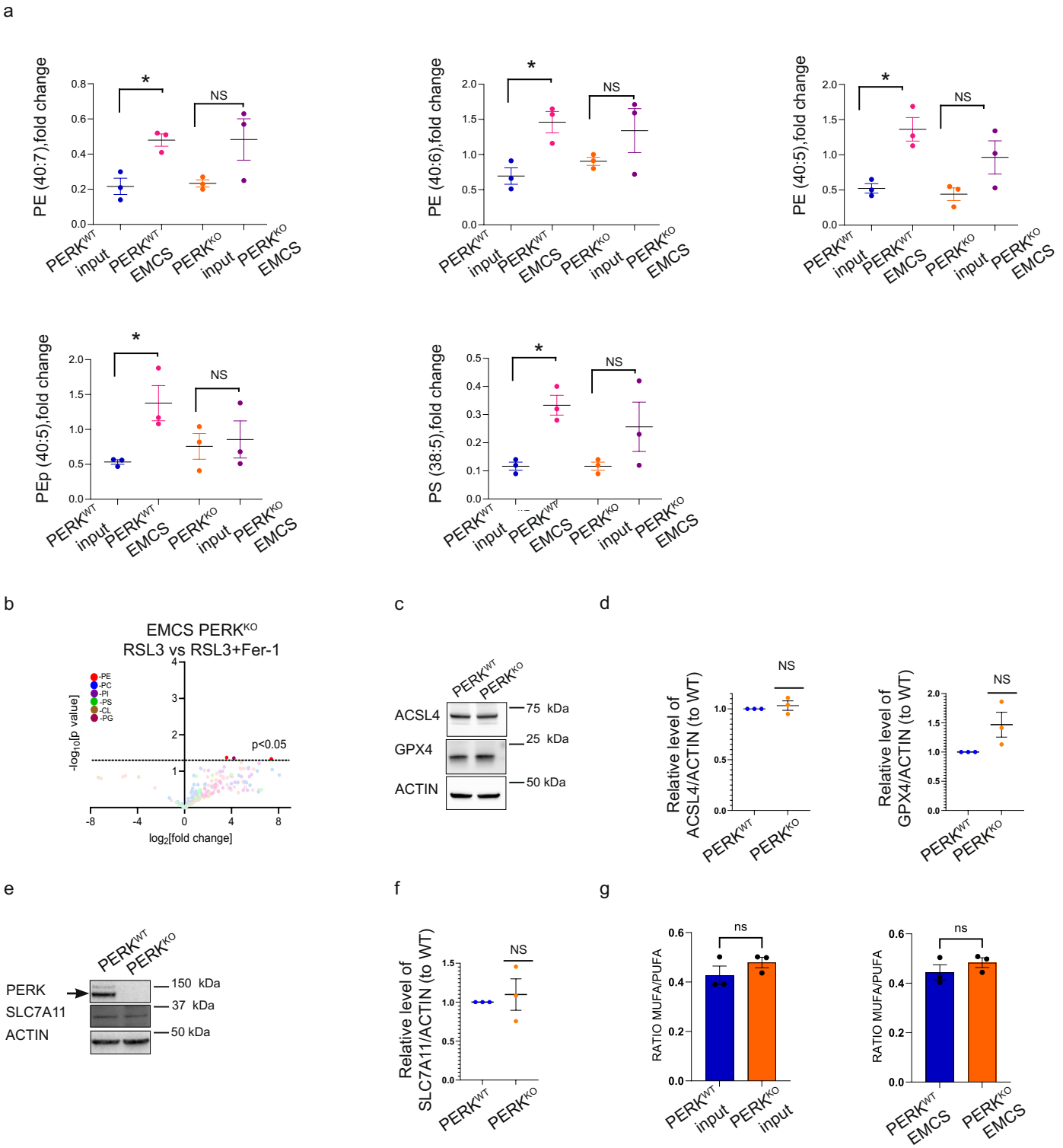


**Extended Data Fig. 8 | Distancing EMCS reduces the abundance of ferroptosis-prone PUFA-containing phospholipids. a**, The contents of PE(40:7), PE(40:6), PE(40:5), PEp(40:5), PS(38:5) precursors in PERK$^{WT}$ and PERK$^{KO}$ EMCSs vs input. (n = 3 biological replicates). **b**, Volcano plot showing the RSL3-induced changes in the content of oxidized PLs in EMCSs of PERK$^{KO}$ cells (RSL3 vs RSL3+Fer-1). (n = 3 biological replicates). **c**, Representative immunoblot for ACSL4 and GPX4 in PERK$^{WT}$ and PERK$^{KO}$ MEFs. ACTIN serves as a loading control. (n = 3 biological replicates). **d**, Quantification of ACSL4 and GPX4 normalized on ACTIN and relative to control condition (WT) (n = 3 biological replicates). **e**, Representative immunoblot for SLC7A11 and PERK in PERK$^{WT}$ and PERK$^{KO}$ MEFs. ACTIN serves as a loading control. N = 3 biological replicates. The arrow indicates PERK. **f**, Quantification of SLC7A11 normalized on ACTIN and relative to control condition (WT). (n = 3 biological replicates). **g**, MUFA/PUFA ratio of total phospholipid (PL) species isolated from input or EMCS fractions PERK$^{WT}$ and PERK$^{KO}$ MEFs (n = 3 biological replicates). All quantitative data are mean ± SEM. In **a**, statistical significance was determined by two-way ANOVA, Sidak post-hoc test. In **d, f**, statistical significance was determined by one sample t-test. In **g**, statistical significance was determined by two sided unpaired t-test. NS, not significant (P > 0.05), *P ≤ 0.05, **P < 0.01, ***P < 0.001. Source numerical and statistical data are provided.

https://doi.org/10.1038/s41556-025-01668-z

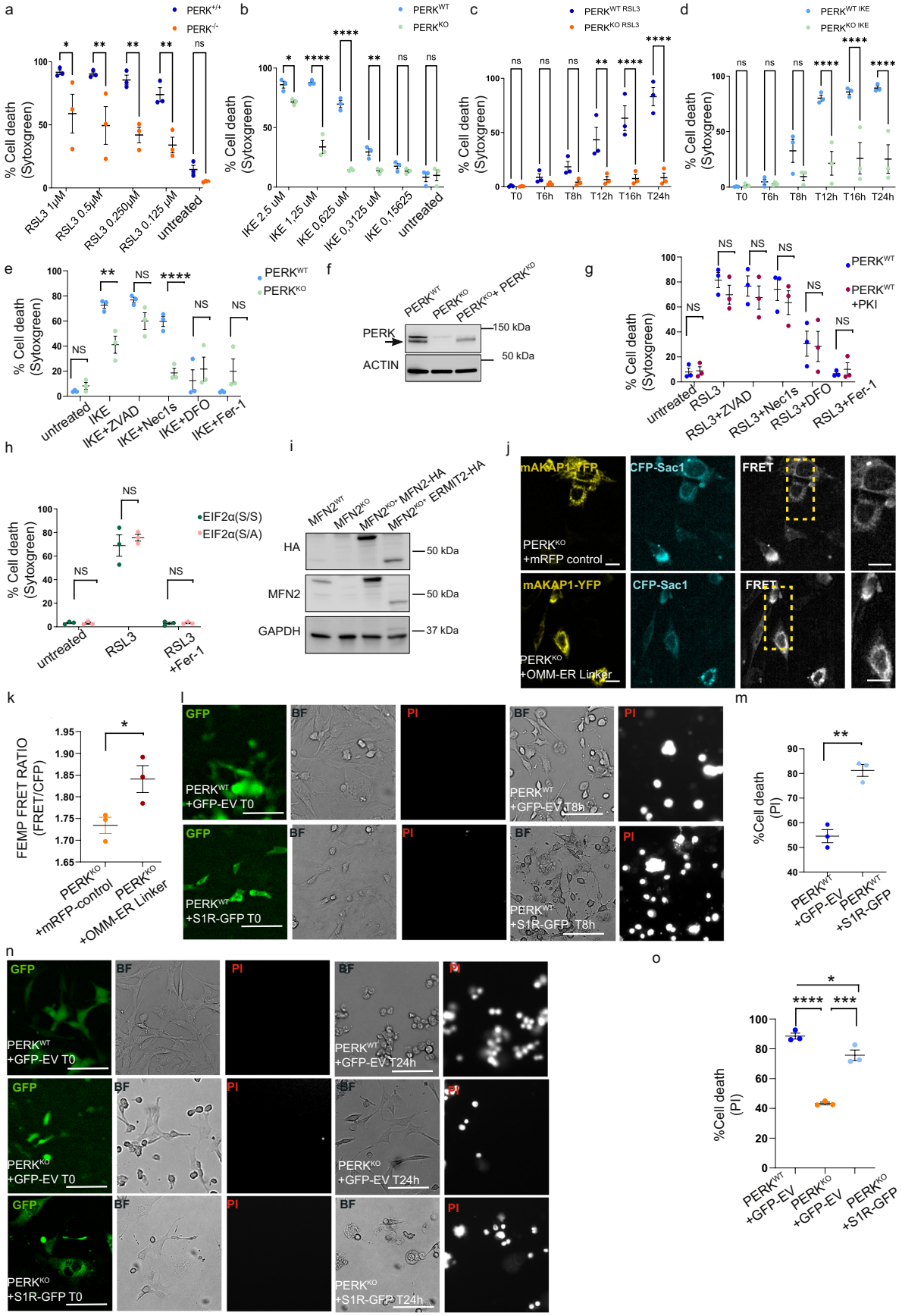


**Extended Data Fig. 9 | See next page for caption.**

https://doi.org/10.1038/s41556-025-01668-z

**Extended Data Fig. 9 | PERK kinase activity is dispensable for promoting ferroptosis. a**, Dose response of RSL3 induced cell death (% Sytoxgreen positive cells) of $PERK^{WT}$ and $PERK^{KO}$ MEFs 24 h after treatment. (n = 3 biological replicates). **b**, Dose response of IKE induced cell death (% Sytoxgreen positive cells) of $PERK^{WT}$ and $PERK^{KO}$ MEFs 24 h after treatment. (n = 3 biological replicates). **c**, Time course of RSL3 (0.125 μM) induced cell death (% Sytoxgreen positive cells) of $PERK^{WT}$ and $PERK^{KO}$ MEFs. (n = 3 biological replicates). **d**, Time course of IKE (0.625 μM) induced cell death (% Sytoxgreen positive cells) of $PERK^{WT}$ and $PERK^{KO}$ MEFs. (n = 3 biological replicates). **e**, % cell death (Sytoxgreen positive cells) of $PERK^{WT}$ and $PERK^{KO}$ MEFs treated for 24 h with IKE (0.625 μM) treatment, in the absence or presence of Z-Val-Ala-DL-Asp(OMe)-fluoromethylketone (ZVAD, 30 μM), Necrostatin-1s (Nec1s, 30 μM), deferoxamine mesylate salt (DFO, 50 μM) or ferrostatin 1 (Fer-1, 1 μM).(n = 3 biological replicates) **f**, Representative immunoblot for PERK in $PERK^{WT}$ and $PERK^{KO}$ MEFs and $PERK^{KO}$ transiently re-expressing $PERK^{KD}$ cells. ACTIN serves as a loading control. **g**, % cell death (Sytoxgreen positive cells) of $PERK^{WT}$ and $PERK^{WT}$ MEFs in the absence or presence of the GSK2606414 PERK inhibitor (PKI), treated for 24 h with RSL3 (0.125 μM) in the absence or presence of Z-Val-Ala-DL-Asp(OMe)-fluoromethylketone (ZVAD, 30 μM), Necrostatin-1s (Nec1s, 30 μM), deferoxamine mesylate salt (DFO, 50 μM) or ferrostatin 1 (Fer-1, 1 μM). (n = 3 biological replicates). **h**, % cell death (Sytoxgreen positive cells) of eIF2α (S/S) and eIF2α (S/A) MEFs treated for 24 h with RSL3 (0.125 μM), in the absence or in the presence of Fer-1 (1 μM). (n = 3 biological replicates). **i**, Representative immunoblot for HA and MFN2 in $MFN2^{WT}$ and $MFN2^{KO}$ MEFs transiently re-expressing HA, MFN2-HA and ERMIT2-HA cells. ACTIN serves as a loading control. **j**, Representative FRET live microscopy images of $PERK^{KO}$ MEFs transiently transfected with AKAP1-mRFP control or OMM-ER linker and transiently infected with FEMP probe (mAKAP1-YFP-Tav2-CFP-Sac1). Scale bar 10 μm. Zoom, 10 μm. **k**, FEMP ratio in $PERK^{KO}$ MEFs transiently transfected with AKAP1-mRFP control or OMM-ER linker and transiently infected with FEMP probe. (n = 3 biological replicates). **l**, Representative images of live $PERK^{WT}$ cells transiently transfected with empty vector (EV) GFP or S1R-GFP at T0 and 8 h after RSL3 (0.5 μM). Images were taken for GFP, PI and bright-field (BF). Scale bar, 100 μm. **m**, % cell death (PI positive cells/total cell number) of $PERK^{WT}$ MEFs transiently transfected with empty vector (EV) GFP or S1R-GFP 8 h after RSL3 (0.5 μM). (n = 3 biological replicates). **n**, Representative images of live $PERK^{WT}$ and $PERK^{KO}$ cells transiently transfected with empty vector (EV) GFP and $PERK^{KO}$ cells transiently transfected with S1R-GFP at T0 and 24 h after RSL3 (0.5 μM) treatment. Images were taken for GFP, PI, and bright-field (BF). Scale bar, 100 μm. **o**, % cell death (PI positive cells/total cell number) $PERK^{WT}$ and $PERK^{KO}$ cells transiently transfected with empty vector (EV) GFP and $PERK^{KO}$ MEFs transiently transfected with S1R-GFP after 24 h RSL3 (0.5 μM). (n = 3 biological replicates). In **a, b, c, d, e, g, h** 3 wells per condition per biological experiment were analyzed. In **k, m, o** multiple areas in the same well were acquired and analyzed at each timepoint per condition and per biological replicate. All quantitative data are mean ± SEM. In **a-e, g, h** statistical significance was determined by two-way ANOVA, Sidak post-hoc test. In **k, m**, statistical significance was determined by two sided unpaired t-test. In **o**, statistical significance was determined by one way ANOVA, Sidak post-hoc test. NS, not significant ($P > 0.05$), *$P \leq 0.05$, **$P < 0.01$, ***$P < 0.001$. Source numerical and statistical data are provided.

https://doi.org/10.1038/s41556-025-01668-z

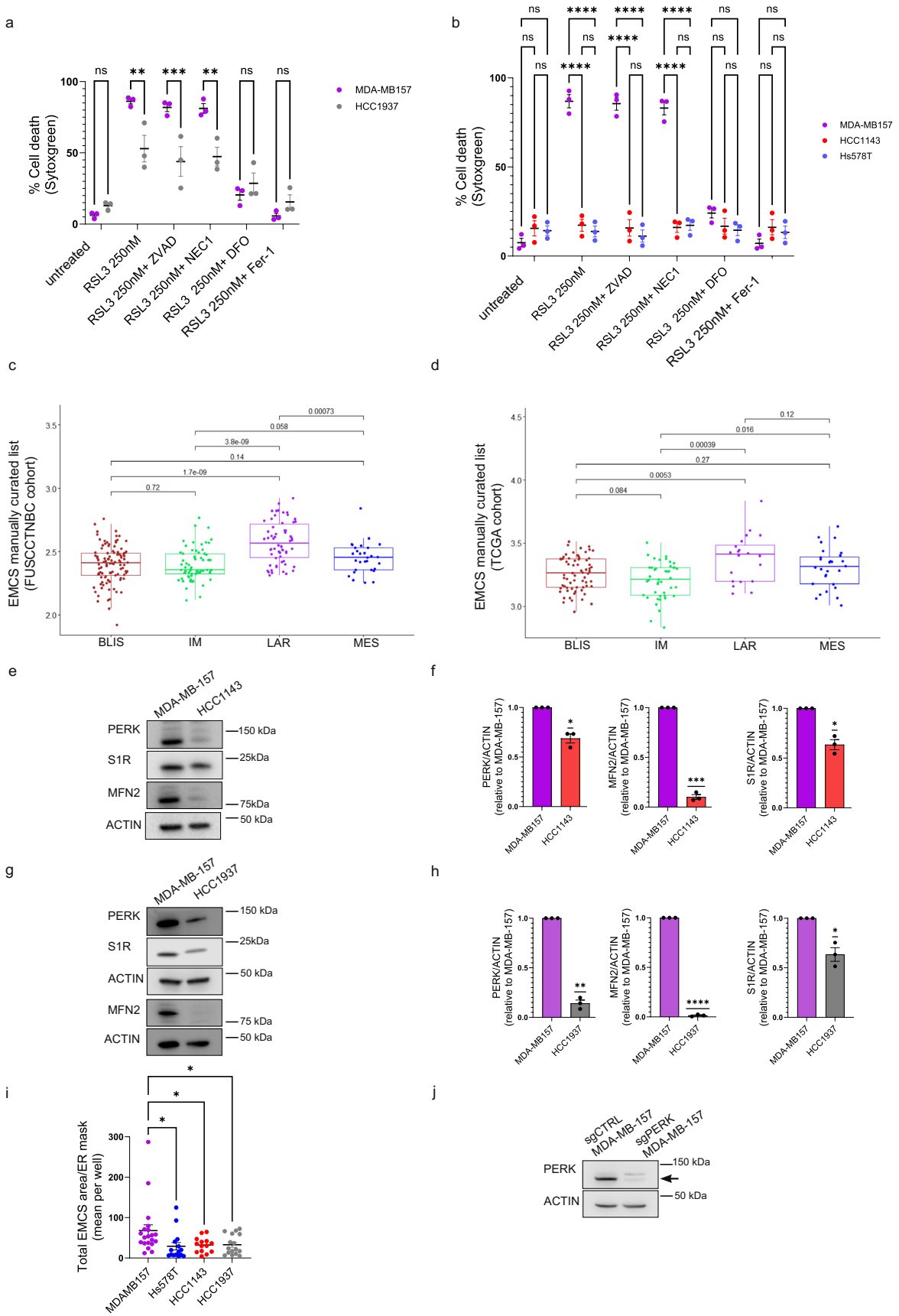


**Extended Data Fig. 10 | See next page for caption.**

https://doi.org/10.1038/s41556-025-01668-z

**Extended Data Fig. 10 | Non-LAR ferroptosis resistant triple-negative breast cancer display reduced EMCS integrity. a**, % cell death (Sytoxgreen positive cells) of MDA-MB-157 and HCC11937 cells treated for 24 h with RSL3 (0.25 µM), in the absence or presence of Z-Val-Ala-DL-Asp(OMe)-fluoromethylketone (ZVAD, 30 µM), Necrostatin-1s (Nec1s, 30 µM), deferoxamine mesylate salt (DFO, 50 µM) or ferrostatin 1 (Fer-1, 1 µM). (n = 3 biological replicates). **b**, % cell death (Sytoxgreen positive cells) of MDA-MB-157, HCC1143 and Hs578T cells treated for 24 h after RSL3 (0.25 µM), in the absence or presence of Z-Val-Ala-DL-Asp(OMe)-fluoromethylketone (ZVAD, 30 µM), Necrostatin-1s (Nec1s, 30 µM), deferoxamine mesylate salt (DFO, 50 µM) or ferrostatin 1 (Fer-1, 1 µM). (n = 3 biological replicates). **c**, Box plot (showing the median line, 1.5× the interquartile range (whiskers)) showing EMCS enrichment score (full list) of each sample calculated by ssGSEA across different TNBC subtypes from FUSCCTNBC cohort (two-sided Wilcoxon's test). n = 258 patient sample (n = 102 Bliss, n = 65 IM, n = 62 LAR, and n = 29 MES). **d**, Box plot (showing the median line, 1.5× the interquartile range (whiskers)) showing EMCS enrichment score (full list) of each sample calculated by ssGSEA across different TNBC subtypes from TCGA cohort (two-sided Wilcoxon's test). n = 158 patient samples (n = 67 Bliss, n = 43 IM, n = 67 20 LAR and n = 28 MES). **e, f**, Representative immunoblot (**e**) for PERK, S1R, MFN2 in MDA-MB-157 and HCC1143 cells and relative quantification (**f**) (to MDA-MB-157). **g, h**, Representative immunoblot (**g**) for PERK, S1R, MFN2 in MDA-MB-157 and HCC1937 cells and relative quantification (**h**) (to MDA-MB-157). **i**, Quantification of EMCS area on ER mask in MDA-MB-157, Hs578T, HCC1143, HCC1937 cells transiently transfected with Sec61ß-GFP and stained with MitoTracker Far Red. (n = 2 biological replicates, multiple areas in the same well were acquired and analyzed at each timepoint per condition and per biological replicate). **j**, Representative immunoblot for sgCTRL and sgPERK MDA-MB-157 cells. ACTIN serves as a loading control. The arrow indicates PERK. In **a, b** 3 wells per condition and per biological experiment were analyzed. In **a, b, f, h, i**, quantitative data are mean ± SEM. In **a, b**, statistical significance was determined by two-way ANOVA, Sidak post-hoc test. In **f, h**, statistical significance was determined by one sample t-test. In **i**, statistical significance was determined by one way ANOVA, Dunnett post-hoc test. NS, not significant ($P > 0.05$), *$P \leq 0.05$, **$P < 0.01$, ***$P < 0.001$. Source numerical and statistical data are provided.

nature portfolio

Corresponding author(s): Prof. Patrizia Agostinis

Last updated by author(s): 25/03/2025

# Reporting Summary

Nature Portfolio wishes to improve the reproducibility of the work that we publish. This form provides structure for consistency and transparency in reporting. For further information on Nature Portfolio policies, see our Editorial Policies and the Editorial Policy Checklist.

## Statistics

For all statistical analyses, confirm that the following items are present in the figure legend, table legend, main text, or Methods section.

| n/a | Confirmed |
|---|---|
| ☐ | ☒ The exact sample size (*n*) for each experimental group/condition, given as a discrete number and unit of measurement |
| ☐ | ☒ A statement on whether measurements were taken from distinct samples or whether the same sample was measured repeatedly |
| ☐ | ☒ The statistical test(s) used AND whether they are one- or two-sided<br>*Only common tests should be described solely by name; describe more complex techniques in the Methods section.* |
| ☒ | ☐ A description of all covariates tested |
| ☐ | ☒ A description of any assumptions or corrections, such as tests of normality and adjustment for multiple comparisons |
| ☐ | ☒ A full description of the statistical parameters including central tendency (e.g. means) or other basic estimates (e.g. regression coefficient) AND variation (e.g. standard deviation) or associated estimates of uncertainty (e.g. confidence intervals) |
| ☐ | ☒ For null hypothesis testing, the test statistic (e.g. *F*, *t*, *r*) with confidence intervals, effect sizes, degrees of freedom and *P* value noted<br>*Give P values as exact values whenever suitable.* |
| ☒ | ☐ For Bayesian analysis, information on the choice of priors and Markov chain Monte Carlo settings |
| ☒ | ☐ For hierarchical and complex designs, identification of the appropriate level for tests and full reporting of outcomes |
| ☒ | ☐ Estimates of effect sizes (e.g. Cohen's *d*, Pearson's *r*), indicating how they were calculated |

*Our web collection on statistics for biologists contains articles on many of the points above.*

## Software and code

Policy information about availability of computer code

| | |
|---|---|
| Data collection | Chemidoc TM MP system (Bio-Rad Laboratories) or AI600 Chemiluminescent Imager (GE Healthcare) for WB analysis. Zeiss LSM 880 – Airyscan for live and fixed confocal super-resolution images). 4D-Nucleofector (Lonza Bioscience) for transient transfection and CRISPR-Cas9 gene knockout. FEI Tecnai 12 microscope equipped with a CCD (SiS 1kx1k keenView) camera or Tecnai-20 electron microscope (Philips-FEI) for TEM Analysis. Olympus IX73 (Olympus) for widefield images. Optima XPN90 (Beckman ultracentrifuge) for subcellular fractionation. Liquid chromatography/mass spectrometry (LC-MC) for lipidomics. BD FACS Canto™ IIBD Canto II or Attune flow cytometer for FACS analysis.FlexStation (Molecular Devices, Sunnyvale, CA, USA) for fluorescent intensity measurements.Zeiss Axio Observer Z1 Inverted Microscope for Ca2+ imaging. Operetta CLS High Content imaging system (Perkin-Elmer) for FRET imaging. |
| Data analysis | FlowJo_v10.8.1 for FACS analysis. Perkin-Elmer Harmony 3.5 image analysis software for FRET analysis. ImageJ/FIJI 1.50i and Imaris 10.1 for super-resolution and TEM images analysis. Image Studio 5.2.5 (Li-Cor Biosciences, Lincoln, NE, USA) or Image Lab 5.2.1 (Bio-Rad Laboratories) for quantifications by densitometry of WB bands. GraphPad Prism 9 for plots and statistic. R Bioconductor package GSVA (version 1.49.0) for the signature gene-set using Single-sample Gene Set Enrichment Analysis (ssGSEA). |

For manuscripts utilizing custom algorithms or software that are central to the research but not yet described in published literature, software must be made available to editors and reviewers. We strongly encourage code deposition in a community repository (e.g. GitHub). See the Nature Portfolio guidelines for submitting code & software for further information.

## Data

Policy information about availability of data

All manuscripts must include a data availability statement. This statement should provide the following information, where applicable:

- Accession codes, unique identifiers, or web links for publicly available datasets
- A description of any restrictions on data availability
- For clinical datasets or third party data, please ensure that the statement adheres to our policy

All data obtained during this study are included in this article and in its supplementary information files. The raw data supporting findings in this article are available from the corresponding author upon request. The bulk RNAseq expression counts were downloaded for 158 The Cancer Genome Atlas Breast Invasive Carcinoma (TCGA -BRCA), Triple Negative Breast Cancer (TNBC) patient samples using TCGA biolinks package in R (TCGA breast cancer data: (https://portal.gdc.cancer.gov); TCGA-BRCA, dbGaP accession phs000178).

## Research involving human participants, their data, or biological material

Policy information about studies with human participants or human data. See also policy information about sex, gender (identity/presentation), and sexual orientation and race, ethnicity and racism.

| | |
|---|---|
| Reporting on sex and gender | N/A |
| Reporting on race, ethnicity, or other socially relevant groupings | N/A |
| Population characteristics | N/A |
| Recruitment | N/A |
| Ethics oversight | N/A |

Note that full information on the approval of the study protocol must also be provided in the manuscript.

# Field-specific reporting

Please select the one below that is the best fit for your research. If you are not sure, read the appropriate sections before making your selection.

☒ Life sciences ☐ Behavioural & social sciences ☐ Ecological, evolutionary & environmental sciences

For a reference copy of the document with all sections, see nature.com/documents/nr-reporting-summary-flat.pdf

# Life sciences study design

All studies must disclose on these points even when the disclosure is negative.

| | |
|---|---|
| Sample size | For all analysis a minimum of 3 independent biological replicates unless specified. No statistical methods were applied to predefine sample size. We based on our labs previous experience in determining the power for disclosing specific effects (sassano et al., JCB, 2023; doi: 10.1083/jcb.202206008). |
| Data exclusions | No data was excluded in any experiments. |
| Replication | All attempt at replication and reproducibility of the experimental findings were successful. This information has been added to the corresponding legends (sample size and values). |
| Randomization | Sample were allocated randomly into experimental groups. |
| Blinding | The investigators analyzing the data were blinded to experimental groups/treatments assignment. |

# Reporting for specific materials, systems and methods

We require information from authors about some types of materials, experimental systems and methods used in many studies. Here, indicate whether each material, system or method listed is relevant to your study. If you are not sure if a list item applies to your research, read the appropriate section before selecting a response.

## Materials & experimental systems

| n/a | Involved in the study |
|---|---|
| ☐ | ☒ Antibodies |
| ☐ | ☒ Eukaryotic cell lines |
| ☒ | ☐ Palaeontology and archaeology |
| ☒ | ☐ Animals and other organisms |
| ☒ | ☐ Clinical data |
| ☒ | ☐ Dual use research of concern |
| ☒ | ☐ Plants |

## Methods

| n/a | Involved in the study |
|---|---|
| ☒ | ☐ ChIP-seq |
| ☐ | ☒ Flow cytometry |
| ☒ | ☐ MRI-based neuroimaging |

# Antibodies

Antibodies used

Anti Mouse Alexa Fluor 488, Thermo Fisher Scientific, A11001, 1:200; Anti Rabbit 488 Alexa Fluor, Thermo Fisher Scientific, A-27034, 1:200; Anti Mouse Alexa Fluor 647 Thermo Fisher Scientific, A-21235, 1:200; Anti Rabbit Alexa Fluor 647, Thermo Fisher Scientific, A-21244, 1:200; Mouse monoclonal anti ACTIN, Sigma Aldrich, A5441, Clone AC-15, Lot number 0000126949, 1:1000; Rabbit monoclonal anti ACSL4, Santa Cruz Biotechnology, sc-271800, Clone A-5, Lot number H0923, 1:1000; Mouse monoclonal anti c-myc, Sigma Aldrich, M4439, Clone 9E10, Lot number 0000184338, 1:1000; Rabbit polyclonal anti Calnexin, Enzo, ADI-SPA-865-F, 1:1000; Mouse monoclonal anti CYTC, BD Bioscience, 556433, Clone 7H8.2C12 (RUO), Lot number 9157540, 1:1000; Duolink™ In Situ Detection Reagents Red, Sigma Aldrich, DUO92008, 1:40; Duolink® In Situ PLA® Probe Anti-Mouse MINUS, Sigma Aldrich, DUO92004, 1:5; Duolink® In Situ PLA® Probe Anti-Rabbit PLUS, Sigma Aldrich, DUO92004, 1:5; Duolink® In Situ Mounting Medium with DAPI, Sigma Aldrich, DUO82040; Rabbit monoclonal anti GAPDH, Cell signaling, 2118S, Clone 14C10, Lot number 16, 1:1000; Rabbit polyclonal anti GPX4, Cell signaling, 52455, 1:1000; Rabbit polyclonal anti HA-Tag (C29F4), Cell signaling, 3724S, 1:1000; Mouse monoclonal anti IP3R3, BD Bioscience, 610312, Clone 2:IP3R-3 (RUO), Lot number 2329334, 1:100; Rabbit polyclonal anti-MFN2, Abcam, ab50838, 1:1000; Rabbit polyclonal anti PERK, Cell signaling, 3192S, 1:1000; Mouse monoclonal anti TOMM20, Abcam, ab186735, Abcam, EPR15581-54, Lot number 1011221-48, 1:100; Rabbit polyclonal VDAC1, Abcam, ab15895, 1:100; Rabbit polyclonal VDAC1, Cell Signaling, 4866S; 1:1000; Rabbit polyclonal anti SLC7A11, Thermo Fisher Scientific, PA1-16893, 1:1000.

Validation

Validation: All antibodies used in this manuscript were commercially bought and validated by the manufacturers, as mentioned on their website. All antibodies were used to detect the respective protein at the expected molecular weight or subcellular localization.

# Eukaryotic cell lines

Policy information about cell lines and Sex and Gender in Research

Cell line source(s)

The triple-negative breast cancer cell lines, MDA-MB-157 and HCC1937 purchased from ATCC, were a gift from Prof. Marcus Conrad (Helmholtz Zentrum München, Germany) and Prof. Colinda Scheele (VIB - KU Leuven Center for Cancer Biology, Leuven, Belgium), respectively. The breast cancer cell lines HCC1143 and Hs578t were purchased from ATCC and authenticated by BMR genomics (Menegollo et al., Cancer Res, 2024; doi: 10.1158/0008-5472.CAN-23-3172.)

Authentication

MDA-MB-157 and HCC1937 cell line were not authenticated. HCC1143 and Hs578t were purchased from ATCC and authenticated by BMR genomics.

Mycoplasma contamination

Cells were regularly checked for mycoplasma contamination and used only when testing mycoplasma negative.

Commonly misidentified lines
(See ICLAC register)

No misidentified cell lines were used in this study.

# Plants

Seed stocks

*Report on the source of all seed stocks or other plant material used. If applicable, state the seed stock centre and catalogue number. If plant specimens were collected from the field, describe the collection location, date and sampling procedures.*

Novel plant genotypes

*Describe the methods by which all novel plant genotypes were produced. This includes those generated by transgenic approaches, gene editing, chemical/radiation-based mutagenesis and hybridization. For transgenic lines, describe the transformation method, the number of independent lines analyzed and the generation upon which experiments were performed. For gene-edited lines, describe the editor used, the endogenous sequence targeted for editing, the targeting guide RNA sequence (if applicable) and how the editor was applied.*

Authentication

*Describe any authentication procedures for each seed stock used or novel genotype generated. Describe any experiments used to assess the effect of a mutation and, where applicable, how potential secondary effects (e.g. second site T-DNA insertions, mosiacism, off-target gene editing) were examined.*

# Flow Cytometry

## Plots

Confirm that:

☒ The axis labels state the marker and fluorochrome used (e.g. CD4-FITC).

☒ The axis scales are clearly visible. Include numbers along axes only for bottom left plot of group (a 'group' is an analysis of identical markers).

☒ All plots are contour plots with outliers or pseudocolor plots.

☒ A numerical value for number of cells or percentage (with statistics) is provided.

## Methodology

| | |
|---|---|
| Sample preparation | After ferroptosis treatments at different timepoints, cells were washed, trypsinized, collected and then stained for MitoPerox (400 nM) or Bodipy 581/591 C11 (2.5 µM) for 30 min. Samples were then washed 2 times with cold PBS and processed using BD FACS Canto™ IIBD Canto II or Attune flow cytometer. |
| Instrument | BD FACS Canto™ IIBD Canto II or Attune flow cytometer |
| Software | Analysis was performed using FlowJo_v10.8.1 software. |
| Cell population abundance | % ox-Bodipy or ox-MitoPerox was calculated on the total population of stained cells with Bodipy C11 or MitoPerox (often higher than 95% of the cells). |
| Gating strategy | initial cell population gating FCS/SSC, FSC-A/FSC-H, was made to exclude debris and select single cell population. BL2-A( PE, Bodipy C11 or MitoPerox) / BL1A (FITC, ox-Bodipy C11 or ox-MitoPerox) to select the double positive cell population. A figure exemplifying the gating sytrategy is provided in the Supplementary information. |

☒ Tick this box to confirm that a figure exemplifying the gating strategy is provided in the Supplementary Information.